Master Thesis

DEVELOPMENT AND VALIDATION OF A MONITOR FOR DETECTING METAL IMPLANTS WITH HEATING RISK WITHIN THE APPLICATION FIELD OF A MAGNETIC STIMULATOR

carried out for the purpose of obtaining the degree of Master of Science, submitted at TU Wien, Faculty of Mechanical and Industrial Engineering,

by

Rita Rabak, BSc

Mat.Nr.: 0725323

under the supervision of

Ao. Univ.-Prof. Dipl.-Ing. DDr. Winfried Mayr

Co-Advisor: Dr. Jose Luis Vargas Luna

Vienna, 22th March, 2018

Rita Rabak	Winfried Mayr

Erklärung zur Verfassung der Arbeit

Ich erkläre an Eides statt, dass die vorliegende Arbeit nach den anerkannten Grundsätzen für wissenschaftliche Abhandlungen von mir selbstständig erstellt wurde. Alle verwendeten Hilfsmittel, insbesondere die zugrunde gelegte Literatur, sind in dieser Arbeit genannt und aufgelistet. Die aus den Quellen wörtlich entnommenen Stellen, sind als solche kenntlich gemacht.

Das Thema dieser Arbeit wurde von mir bisher weder im In- noch Ausland eier Beurteilerin/einem Beurteiler zur Begutachtung in irgendeiner Form als Prüfungsarbeit vorgelegt. Diese Arbeit stimmt mit der von den Begutachterinnen/Begutachtern beurteilten Arbeit überein.

Vienna, 22th March, 2018

Rita Rabak

ABSTRACT

Pelvic floor therapy with Functional Magnetic Stimulation (FES) is becoming more and more popular in different groups of patients. More generally the field of FMS applications extends over a multitude of different possibilities, starting with the transcranial magnetic stimulation for migraine treatment to strengthening various muscles via neuromuscular activation. Magnetic stimulation has key advantages over conventional electrical therapies. These advantages are mostly because of the ease of application, where the treatment can be done through everyday clothing and the avoidance of possible skin irritations or even burns due to high current densities in the electrode contact surface and a highly effective treatment with less sensible discomfort. An important limitation of magnetic stimulation strong impulse fields is the potential heating of metal parts by induced eddy currents. This heating can be dangerous if the surrounding tissues cannot compensate this heating with natural mechanisms. Due to the increasing number of hip implants, a safe detection of the implants is becoming more important.

This thesis describes the development of the prototype for a metal monitor/detector developed by the Medical University of Vienna, in cooperation with gbo Medizintechnik AG, for PonteMed GmbH. The PelviPower Magnetic Field Trainer is a device for the muscular strengthening of the pelvic and the surrounding muscles. The system consists of a magnetic coil embedded in a seat surface. The electrical induction leads to a depolarization of nerves and thus to action potentials that result in muscle contractions. To ensure the safety of patients, it is particularly important to identify any implants in the field range before starting a treatment in order to avoid possible damage of tissue around these objects. The evaluated metal samples were a flat cylinder of iron, a cobalt-chrome sphere shaped hip head, a titanium and a titanium-aluminum alloy acetabulum prosthesis. For the identification of dangerous regions in which a metal can harm surrounding tissue, metal samples were exposed to the magnetic field, the temperature rise was monitored and the power density calculated from these results. Wolfs claims (Wolf, 2008) that a power density above 40mW/cm^2 could become dangerous for the surrounding tissue. Accordingly, the regions of interest were determined where the power density is above this critical power density mark. Because of varying magnetic remanence effects in the core of the therapy coil, recalibration is necessary at the beginning of new application sessions. After that, the system tests for magnetic impedance changes, potentially cause by metal objects within the regions of interest. If a metal is detected, the process stops and a warning signal is displayed on the control screen.

In summary, all distances and positions where a critical power density occurred in a specific sample could reliably be detected in the test series. Furthermore, all samples, exception iron at one specific position, were detected with an additional 20mm safety margin between the maximum detectable distance and the distance where the power density is below the critical mark.

CONTENTS

CHAPTER

1 INTRODUCTION

This chapter presents the abstract, the typical materials and the theoretical background of the key terms. The first section reviews the summary of the thesis. The second section explains the typical materials for hip implants and the materials used for the additional measurements, see Appendix A. The main measurements focus on the four used materials. Afterwards, the chapter considers an overview of the theoretical background to make the thesis easier to understand. The last section of this chapter defines the regions of interest. These are those areas where dangerous heating of the surrounding tissue can occur.

1.1 BASIC CONCEPT

Functional Magnetic Stimulation (FMS) is becoming more and more popular in different groups of patients. More generally the field of FMS applications extends over a multitude of different possibilities, starting with the transcranial magnetic stimulation for tinnitus treatment (Langguth B, 2014) (Robert L. Folmer, 2015), treatment of migraine (Ria Bhola, 2015) or epilepsy (Vasilios K. Kimiskidis, 2013) over pain relief to strengthen the pelvic floor, stress urinary incontinence (Yesim Bakar, 2011) and overactive bladder (H.D. Bradshaw, 2003).

Michael Faraday discovered that a time-varying magnetic field can induce an electric current, which constitutes the basic of magnetic stimulation. If such a magnetic field is strong enough, it is able to depolarize nerve fibers and this leads to action potentials and elicit muscle contractions (Mark S. George, 2007) (Masahito Kobayashi, 2003). In contrast to electrical stimulation, magnetic stimulation is a more recent technique. The first exploration of electrical stimulation was already made in the 18th century by Luigi Galvani with the muscle stimulation of frogs. He placed electrodes on certain parts of the body of the frogs and discovered the electrically excitable of nerves by the stimuli (Geddes, 1994) (Martellucci, 2015).

In electrical stimulation, electrodes are required to be in direct contact with the body. Therefore the electrode placement for certain applications could feel uncomfortable. A significant advantage of magnetic stimulation is that the magnetic field can be wirelessly transmitted even over clothing and this allows a highly effective treatment through everyday clothing. This is particularly appreciated by patients for stimulating the pelvic floor because it avoids the use of vaginal or anal electrodes. Another advantage is the avoidance of possible skin irritations or

even burns due to high current densities in the electrode contact surface (Alfred E. Bent, 2008) (Medical Boston Center, 2017) (Maurice Lippmann, 1974) (Flora Margarida Barra Bisinottoa, 2017).

An important limitation of magnetic stimulation strong impulse fields is the potential heating of metal parts. If a metal piece, like a hip implant, is present in the magnetic field, this object heats up by eddy currents, if this object is in a time-varying magnetic field. Depending on the position and distance between coil and sample, the surrounding tissue is heating up differently. This heating can be particularly dangerous if the surrounding tissues cannot compensate this heating with natural mechanisms. Due to the increasing number of hip implants, a safe detection of the implants is becoming more important. The number of hip joint implantations has fallen slightly in Austria in recent years, but in comparison to other countries, Austria is at the third place, behind Germany and Switzerland. According to "Statista", 273 hip joint surgeries per 100,000 inhabitants were carried out in 2011 in Austria. In 2015, this number fell slightly to 271 operations (Statista). The proportion of people over 60-years is growing, through the longer life expectancy and the returning birth rates, faster than any other age group (Health). According to Statistik Austria, about 500.000 more people over 60 years will be living in Austria in the year 2050 and therefore the number of hip operations will rise rapidly (Wakolbinger, 2013). It is also known that especially elderly people have to undergo hip replacements. But also younger people get often an artificial hip. Already in 2008, 10% of operations were performed on patients under the age of 50 years (Standard, 2008). Therefore it is essential to carry out an examination of metallic objects before the magnetic stimulation starts.

There are nearly no studies of heating the metal parts on a magnetic field trainer. Since the heating of metal parts can also occur in Magnetic Resonance Imaging (MRI), many studies about the risk of burning to the surrounding tissue during an MRI examination have been consulted (Yigitcan Eryaman, 2011) (Peter Nordbeck, 2008) (Kenneth B. Baker, 2004) (Hansjörg Graf, 2007). As with the PelviPower Magnetic Field Trainer, the MRI works with magnetic fields, but these are stronger than the magnetic fields in the stimulation chair (Quick, 2011) (Wood R, 2012) (Girometti, 2015) and the distance between patient and coil is larger, but the risk of burning is given in both techniques. As shown in previous studies, there are several variables that affect the heating of guidewires and catheters. The study “RF Safety of Wires in Interventional MRI: Using a Safety Index” deals with a safety index which precisely calculates the maximum permissible heating (Christopher J. Yeung, 2002). Like in this study, a safety margin for the maximum power density was also defined in this thesis. Other different studies that investigate the heating of hip implants during MRI are concluding that the maximum temperature rise was at the peak with the largest curvature and that this value depends on the physical properties of the material (Hiroyuki Muranaka, 2009) (Yamazaki M, 2016).

This thesis describes the development of the metal monitor/detector developed by the Medical University of Vienna, in cooperation with gbo Medizintechnik AG, for PonteMed GmbH and the continuation of the master thesis "Safety Monitoring for Functional Magnetic Stimulation" (Nalbach, 2016). In this thesis, a prototype of a safety monitor for the PelviPower Magnetic Field Trainer is developed. This PelviPower Magnetic Field Trainer is used to treat an insufficient pelvic floor and resulting symptoms, such as urinary incontinence (D.D. Chandi, 2003) (Igor But, 2005) (Tomonori Yamanishi, 2014) (Tadeja Štrumbelj). Other areas of application include back pain in the lower back (Corey B. Simon, 2016) (Eun Jung Park, 2014) and the lumbar vertebrae (Timothy Wade Stippick, 2016) or strengthening the pelvic floor function before surgery.

The system consists of a magnetic coil embedded in a seat surface. The coil generates a magnetic field with short magnetic field impulses and a magnetic flux density up to 1 Tesla (PonteMed, Bedienungsanleitung, 2016). Depending on the intensity, the depth of penetration is between 5cm and 15cm. The pulses generate a contraction of the muscle, where they are kept under tension for a certain time and then relaxed again.

To ensure the safety of patients, it is particularly important to identify any implants in the field range before starting the treatment to avoid possible damage of tissue around these objects. Therefore, this thesis focuses on three main topics: the temperature rise during a standard treatment, identifying the regions where typical hip implants parts are dangerously heated up and the development of a metal monitor.

For the metal monitor, a hardware and software design is developed. The hardware is designed to inject a current sinewave and measure a voltage drops if a metal part is in the immediate vicinity of the coil. The metal detector itself is designed as a slave device. This means that the detector only responds to commands receives via the UART port. The microcontroller is programmed with the MPLAB HARMONY Configurator v1.09 on MPLAB X IDE v3.45. A problem with the system is the heating of the operational amplifier. Therefore a fan has been added to control the temperatures of the operational amplifier. As secondary software, a Microchip Technology Inc. AN1388: PIC32 bootloader is integrated into the microcontroller. This algorithm allows the PelviPower Box to perform software updates directly from the UART port. For the temperature rise, the measurements were carried out with an infrared thermometer and evaluated with the associated software. In order to determine the device settings, where the metal heated up the most, a worst case scenario was tested. The evaluated metal samples were a flat cylinder of iron as a reference value, a cobalt-chrome sphere shaped hip head, a titanium and a titanium-aluminum alloy acetabulum prosthesis, which was measured over five different positions of the coil at four different distances. The distance between the metal samples and the seat surface was increased by stacking 20mm plexiglas sheets. Because of the material

properties of plexiglas, these sheets were not affected by the magnetic field and had no effect on the measurement. To prevent damage to the chair's seat, all measurements started at a distance of 20mm and increased up to 80mm for the temperature measurements. The five positions were located in the center of the coil (Center), above a pole (Corner), in the center of two poles (Edge), between the Center and the Edge (MidEdge) and between the Center and the Corner (MidCorner). The temperature measurements are evaluated with the aim to identify the regions of interest, where the power density is above the critical power density. According to Wolf (Wolf, 2008), the maximum power density is defined at 40mW/cm^2 before it could become dangerous for the surrounding tissue. The temperature values were monitored during the whole stimulation and then post-processed with MATLAB (The MathWorks, Inc., Natrick, USA) to estimate the maximum power density. For the sensibility measurements, the regions of interest are particularly important to detect. In order to increase the safety margin, an additional distance of 20mm is added at each position and for each sample. Because of varying magnetic remanence effects in the core of the therapy coil, recalibration is necessary at the beginning of new application sessions. This magnetic remanence affects the measured voltage even if no metal is present. Therefore, the system must be calibrated, with every 10% step measurements are taken and stored as reference values. After successful calibration, the patient can sit down on the chair and every 10% step a measurement is made and compared with the previously measured reference value. If a metal is detected during this measurement, the voltage level changes during the measurement, the detection stops, and a warning signal is displayed on the control screen. After successful detection, the actual treatment can start.

The highest power densities are measured with the iron sample, as expected. Since this sample does not occur in the human body in this form, it is taken as a reference value for other non-biocompatible materials. The comparison of the other samples shows, that pure Ti in the Center of the coil has the highest power density. In order to discover the implant safely, the maximum detectable distance is determined depending on position and distance. Therefore the highest detectable distance can be detected in the position Center, independent of the used sample. In the MidCorner and MidEdge position, CoCr29Mo measure the highest distance. Edge and Corner detection are not possible in any of the three samples. But damage to the surrounding tissue occurs only if the power density is above the critical mark and in these two positions, the power density is well below the critical mark. In all other positions, each sample with a power density above 40mW/cm^2 was reliably detected and, exception iron at one specific position, all samples were detected with an additional 20mm safety margin between the maximum detectable distance and the distance where the power density is below the critical mark.

Eddy currents, and therefore the heating depends on the material, the geometry and the orientation of the object. Therefore, it is not possible to test all the possible scenarios. Additional

measurements with a smaller CoCr29Mo sample are carried out to prove if the detection range changed with changed dimensions of the sample. In summary, it can be concluded, that the small sample can also be reliably detected on the dangerous positions. Although these measurements were not extensive, they provide a hint that this tendency might apply to different geometries and positions. Other additional measurements are carried out with an intrauterine device and a piercing. The result of the measurements represents no significant heating and therefore no damage to the surrounding tissues. Furthermore, tests to investigate the mechanical vibrations of the intrauterine device are carried out. The tests show that the device does not move above the seat of the PelviPower Magnetic Field Trainer during treatment. Nevertheless, more detailed investigations should still be made in order to obtain reliable statements about these results.

1.2 MATERIALS

The main focus of this thesis has been set on the various hip implants, as this represents the greatest risk for the health of patients. Although there is a great amount of implants commercially available, the most commonly used materials are implants based on pure titanium, titanium alloys (e.g. Ti6Al4V), cobalt-chrome alloys (e.g. CoCr29Mo) and some types of stainless steel (e.g. 316L) (M. Geetha, 2009) (Ke Yang, 2010) (Monika Saini, 2015).

1.2.1 IMPLANT MATERIALS

The hip joint is a ball joint and connects the pelvis to the thighs. It consists of the acetabulum and the femoral head, both are covered with a cartilage. Between these parts is the joint fluid. In an artificial hip joint, the damaged parts of the hip are replaced with an artificial joint. Figure 1 shows the artificial hip joint, consisting of a femoral shaft, the head and acetabulum component.

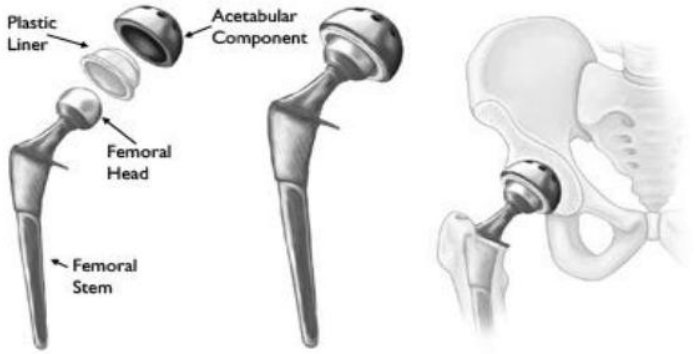

Figure 1: Components of an artificial hip joint (Sachin G. Ghalme, 2016)

There are different materials for the production of artificial joints. It is distinguished among polymer-, ceramic- and stainless steel materials. In contrast to metallic objects, polymer and ceramics objects do not heat up due to eddy currents, described in section 1.3.5. For this reason, these objects aren`t included in this thesis.

The most commonly used materials are implants based on pure titanium, titanium alloys (e.g. Ti6Al4V), cobalt-chrome alloys (e.g. CoCr29Mo) and some types of stainless steel (e.g. 316L) (M. Geetha, 2009) (Ke Yang, 2010) (Monika Saini, 2015) (Sachin G. Ghalme, 2016).

Stainless steel materials are more resistant and allow the formation of self-healing and corrosion-resistant coating oxide of Cr203. Nevertheless, the materials are degraded by the body over time. This is due to fatigue and various types of corrosion. The wear resistance is also relatively weak and leads to a damage to the joint. A disadvantage of surgical steel is the release of nickel into the surrounding tissue. This can lead to swelling, redness, eczema, but also to other allergic actions.

There are two cobalt-chromium alloys used: Co-Cr-Mo and Co-Ni-Cr-Mo. These alloys produce an oxide deposit within the fabric and make the material highly corrosion resistant. They have a high resistance to fatigue and wear resistance. Due to the corrosive environment in the tissue, the elements Ni, Cr and Co are released in the body.

Another type of alloy is titanium-based (e.g. Ti6Al-V4). Advantages of this type are their low density, high specific strength, good corrosion resistance by the formation of an oxide layer. Moreover, these alloys are wear-resistant (Sachin G. Ghalme, 2016) (Ke Yang, 2010).

Although new stainless steels are under development, the gold standard for this type of implants is the cobalt-chrome alloys and, mainly, titanium alloys (M. Geetha, 2009). Therefore, this development will focus on three main materials: Pure titanium (Ti), one representative cobalt-chrome alloy (CoCr29Mo), and one representative titanium alloy (Ti6Al4V). Also, an iron sample will be included in the measurement as a reference value to representative data for other non-biocompatible materials.

1.2.2 Other Materials

Apart from the implants, there are also various materials for intimate piercings and contraceptive devices.

Piercings can be made from different materials. The best-known materials are titanium, gold, silver and surgical steel. But also platinum, niobium, bones and various plastics can be used. In particular, nickel alloys, which occur in surgical steel, gold, and silver, can trigger allergies. Titanium or platinum is suitable as a substitute for this alloy. This makes pure titanium and titanium alloys more and more popular (Ebner) (Bär, 2008).

There are two different types of spirals as receptive devices, namely copper and hormone spirals. The copper spiral is distinguished between a spiral with a silver core or a gold core. Both cores are wrapped with a copper wire and discharge copper ions. The hormone spiral has a

supply of the progestogen Levenorgestrel instead of the copper windings, which is also present in anti-baby pills (Bürscher, 2016). In this thesis, an intrauterine device is used.

1.3 THEORETICAL BACKGROUND

1.3.1 CHARACTERISTICS OF THE MAGNETIC FIELD

Permeability

The influence of the materials in the magnetic field is known as absolute permeability and can be described as the relation between the magnetic flux density (Formula 1) and the magnetic field strength on a given material. The absolute permeability can be broken down into a permeability proportion in relation to the one of the vacuum.

$$B = \mu_0 * \mu_r * H$$

Formula 1: Magnetic flux density

The magnetic field constant μ_0 (Formula 2) is equal to the vacuum permeability. The relative permeability μ_r depends on the material and is a dimensionless factor (Bernstein, 2012) (Weißgerber, 2013) (Kallenbach, 2008).

$$\mu_0 = 4 * \pi * 10^{-7} \frac{Vs}{Am}$$

Formula 2: Magnetic field constant

Electrical resistance

The electrical resistance ρ (Formula 3) is a material-specific variable, as can be seen in Table 1, and indicates the conductivity of a material through its electrons. It depends on the movement of the charge carriers, which collide with the ions sitting in fixed places. The oscillation of these ions is depending on the temperature. At higher temperatures, the mobility of the charge carriers is smaller and therefore the resistance is higher. For metals, the electrical resistance depends on the temperature and increases with increasing temperature.

$$\rho=\rho_{20}*[1+\alpha_{20}*(\vartheta\text{-}20°C)]$$

Formula 3: Electrical resistance

Based on the resistance, it is also possible to distinguish between the conductor, the semiconductor, and the non- conductor. Metals are particularly good electrical conductors since they consist of a positively charged atomic core and electrons that can move freely.

Table 1: Characteristics of electrical conductors (Peter Kurzweil, 2008)

	Electrical resistance ρ [Ωm]	**Electrical conductivity κ [Sm^{-1}]**	**Example**
Conductor	< 10^{-5}	> 10^{5}	Copper
Semiconductor	10^{-5}... 10^{7}	10^{5} ... 10^{-7}	Silicon
Non- conductor	>10^{7}	< 10^{-7}	Glass

Characteristics of electrical conductors are the high number of mobile charge carriers, the associated good electrical conductivity, and small electrical resistance (Peter Kurzweil, 2008). The specific electrical resistance depends on the material electrical resistance, the length and the cross-section (Wilfried Plaßmann, 2009) (Obermann, 2006) (Steffen Paul, 2014).

The electrical conductivity is the reciprocal of the specific resistance and indicates how well the current is conducted in a specific material.

Specific heat

The specific heat indicates the heat absorption and release capacity of a material and expresses the amount of heat needed to heat 1 gram of a material by 1K. The lower this is, the faster the material heats up but cools down quickly as well. Metal is therefore a relatively low heat storage but because of its good mobility of the valence electrons a good heat conductor. In addition to the lattice vibrations, electrical charges also make a contribution to heat transfer. At the same time, this mobility also ensures its good electrical conductivity and is therefore based on the same mechanism.

The relationship between thermal conductivity and electrical conductivity can be explained by Wiedemann-Franz's law and states that the ratio is equal to the Boltzmann constant and the elementary charge multiplied by the absolute temperature (Rau, 2004) (Welsch, 2013) (Gerthsen, 1964).

1.3.2 MAGNETIC REMANENCE

The magnetic remanence is the flux density remaining after switching off an external magnetic field in a ferromagnetic material. When a magnetic field is applied again, the flux density depends on the new field and on the previous history. The unit of remanence is given by the magnetic flux density in Tesla. It can be described by remanence magnetization M_r, remanence

induction B_r (Formula 4), and remanence polarization J (Czichos, 1991)(P. Weinzierl, 1970)(Schönekeß, 2009).

$$B_r = J_r = \mu_o * M_r$$

Formula 4: Remanence induction

1.3.3 ELECTROMAGNETIC INDUCTION

Electromagnetic induction produces a voltage and thereby a current flow. This generation takes place by movement of an electrical conductor in the magnetic field or by a temporal change of the magnetic field. Faraday's law of induction states that a time-varying magnetic field can induce an electric current. This proved the relationship between electric and magnetic fields. The induced electrical voltage U_{ind} (Formula 5) depends on the magnetic flux $d\Phi$ and the differential dt. This voltage is proportional to the strength and rate of change of the magnetic field, which can be caused by the modification of the magnetic field itself or by the spatial movement of a coil across the field. For the coil, the voltage is higher the greater the number of turns and the cross-section of the coil are. The sign of this equation is determined by Lenz's law. The induced voltage counteracts the change in flux (Georg, 1999) (Giancoli, 2010) (Breuer, 1989) (Karl Küpfmüller, 2013).

$$U_{ind} = -\frac{d\Phi}{dt}$$

Formula 5: Electromagnetic induction

1.3.4 SKIN EFFECT

The skin effect is described as the currents concentration in the areas near the surface, and its exponential decrease with the distance. It is directly linked to Faraday's Law and depends on frequency, the diameter of the conductor and the properties of the used material, like magnetic permeability and electrical conductivity. The higher these values the higher is the skin effect. The resistance of the conductor is inversely proportional to the cross-sectional area of the conductor. The skin effect results in a reduction of the cross-sectional area and thus in an increasing of the resistance. This leads to a higher temperature at higher frequencies with the same current. The depth of penetration δ (Formula 6) describes the distance where the current fall to 37% of the original value. At low frequencies, there is a small increase near the surface of the conductor and at high frequencies, the current flows only on the surface of the material (Brooks, 2009) (E. Hering, 2005).

$$\delta = \sqrt{\frac{2}{\sigma * \mu * \omega}}$$

Formula 6: Depth of penetration

1.3.5 EDDY CURRENTS

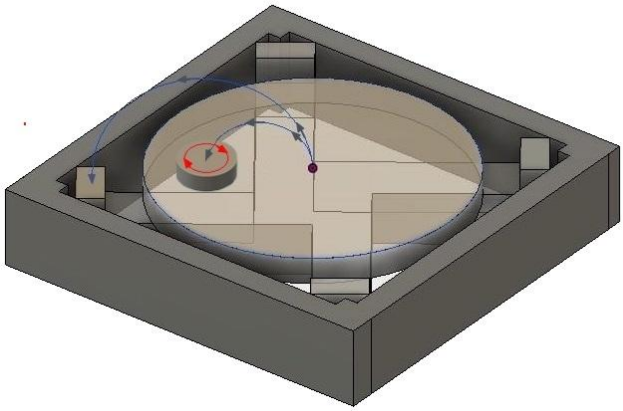

Figure 2: Used coil with the magnetic field (blue line) and eddy current (red line)

If an electrically conductive material is in a magnetic field, eddy currents (Figure 2) are induced according to induction law. These currents flow in closed loops perpendicular to the magnetic flux and can arise by a time-variable magnetic field or by the change in time caused by the movement of a conductive object. The eddy currents themselves generate a magnetic field and counteract the original field. The electrons are accelerated by the resulting eddy currents and collide with the immobile metal atoms and cause them to vibrate. The kinetic energy is converted into Joule heat, which finally heats the conductor depending on the electrical conductivity of the material.

Due to the skin effect the eddy currents concentrate near to the surface and decrease exponentially with the distance. Low frequencies produce weak eddy currents that penetrate deeply into the material. In contrast, high frequencies produce strong eddy currents that cannot penetrate deeply through the skin effect.

Eddy currents depend on several factors and properties of the metal part and the induced magnetic field. From the metal part, eddy currents are influenced by the material properties like magnetic permeability, electrical resistance, electrical conductivity, and, on the other hand, it is also influenced by the geometry of the part and the cross-section that is exposed to the magnetic field. An increase in the magnetic permeability and the electrical resistance leads to a decrease in the penetration depth of the eddy current. Eddy currents are also dependent on the magnetic flux density and magnetic field strength. The larger these values, the larger are the eddy currents. Because the magnetic field becomes smaller with the distance to the coil, the eddy currents also decrease with increasing distance. With increasing frequency the magnetic flux density and magnetic flux increases, resulting in a higher induction voltage and a higher current in the object. In addition, the eddy currents are becoming weaker with increasing distance from

the seat surface to the sample (Brooks, 2009) (E. Hering, 2005) (Mukerji, 2015) (Jiles, 2007) (Heintze, 2016).

1.3.6 INDUCTIVE HEATING

When a metal part is within a magnetic field, the induced eddy currents flowing through the electrical resistance of the material are producing energy dissipation, also called inductive heating. This process is a direct conversion with high efficiency. A further advantage is the heating of the material through non-conductive materials, such as, for example, the pad of the PelviPower chair.

The heating depth depends, on the one hand, on the material properties like magnetic permeability or electrical resistance of the material and, on the other hand, on the used frequency. A lower frequency results in a higher penetration depth (EMAG eldec Induction GmbH, 2017) (Kurt Steinhoff, 2011).

1.4 DEFINITION OF REGIONS OF INTEREST

This thesis focuses on the detection of metal implants that could damage the surrounding tissue. Therefore, the regions of interest are those regions where the inductive heating of an implant reaches critical values. Because of that, the surrounding tissue is not able to compensate this heating by natural dissipation mechanisms which lead to tissue damage and harm the patient. The heat irradiation to the surrounding tissues by a heated metal is described by the heat flux P (Formula 7). The heat flux depends on the specific heat c_p of the material, the mass m of the sample and the change of temperature ΔT at a given time t.

$$P = c_p m \frac{\Delta T}{t}$$

Formula 7: Heat flux

The resulting rate of thermal energy is then divided by the metal part's surface area in cm^2 to calculate the heat flux (power density).

Wolf (Wolf, 2008) estimated the limits of heat flow in transcranial implants using the Pennes-designed bioheat equation. Pennes links the temperature change of a tissue having a specific heat to the tissue's thermal conductivity, volumetric heat losses, heat losses due to blood perfusion and metabolic heat generation. According to this equation, Wolf concludes damage to the surrounding tissue with a heat flux of $40mW/cm^2$. Heat fluxes smaller than this critical power density has no negative effects on the tissue and is compensated independently. Based on these findings, the regions of interest are defined as any location where a metal part is able to produce a heat flux of $40mW/cm^2$ or more (Wolf, 2008) (Pennes, 1948).

CHAPTER 2 DEVELOPMENT

This chapter discusses the hardware and software design of the PelviPower Magnetic Field Trainer. The main focus of this thesis is on the different temperature and sensibility measurements, with the aim of detecting a metal object reliably if this object has a power density above the critical mark and is therefore dangerous for the patient. Therefore only a brief overview of the hardware and software design is given in this chapter. The detailed description can be found in the thesis "Safety Monitoring for Functional Magnetic Stimulation"(Nalbach, 2016) and in the report “Development of a monitor to detect metallic implants in the surroundings of the PelviPower MTF coil” (Vargas Luna, 2016). This thesis followed previous results and modified them for subsequent prototype measurements.

This chapter is divided into two parts. The first section describes the hardware design, including the circuit design. The second section considers the software design. It explains the state machine, the universal asynchronous receiver/transmitter (UART) protocol, but also the temperature control and the used bootloader. Another important sector is the calibration and detection, which is especially important for the measurement of sensibility, see chapter 4.

2.1 HARDWARE DESIGN

The hardware is designed to inject an excitation current to a resonant circuit composed by the coil and a capacitor. If a metal is in the immediate vicinity, a voltage drop occurs. The hardware measures this voltage drop and will process it further. In addition, the system is disconnected when the magnetic stimulation is active. This protects the system from the high-power electronics of the PelviPower Magnetic Field Trainer by using relays that connect and disconnect the coil, bidirectional digital isolators, and isolated power supplies. In Figure 3 the connections through the red box can be seen. Inside the device, the controller is organized by a microcontroller. This executes all functions depending on the requests received by the main stimulator. The amplifier block includes a sine-wave generator that generates a voltage at a specific frequency. The signal is adjusted as required and comes to a voltage-current converter that generates this excitation current signal. The current wave comes to a resistor or capacitor, depending on the application. These are connected in parallel to the coil by two isolation relays. To check the voltage level itself, a dummy resistor has been added. Once the current is diverted

to the desired load LC tank or dummy resistor, the voltage on the load is rectified and the peak level is detected. Since the LC tank requires relatively high power, there is a temperature increase in the main amplifier, which can lead to current drifts. To avoid this, a temperature control system is implemented. This system includes a heat sink with a temperature sensor and a fan to keep the temperature stable. Figure 3 shows an overview of the functional blocks and the processes of the system.

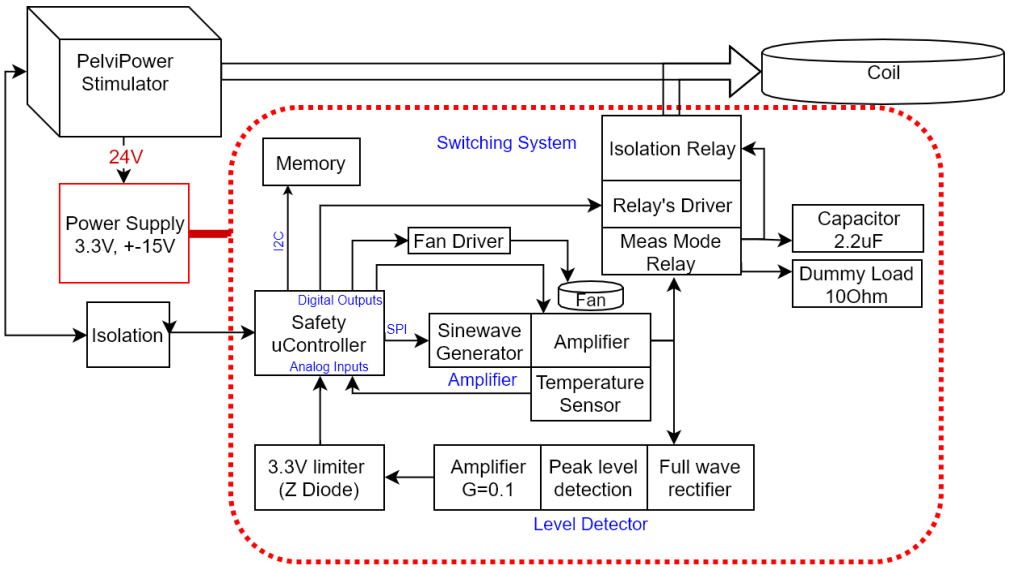

Figure 3: Basic schematic of the hardware design. The red box shows the isolation through the relays, the bidirectional digital isolator and the isolated power supplies (Vargas Luna, 2016)

2.1.1 *Circuit design*

The concept and circuit schematic are developed at the Medical University of Vienna and finally implemented by gbo Medizintechnik AG. The complete circuit diagrams can be found in Appendix C.

2.2 Software design

The metal detector is designed as a slave device that can only respond to commands received via the UART port. For this reason, the monitor considers the stimulator box as a prerequisite for proper operation. Therefore some conditions must be satisfied. First, the capacitor must be completely discharged in the stimulation box. There is no stimulation during calibration or detection. The coil position provided via UART is true and the position of calibration and detection must be in the same position. This ensures that the appropriate position values are compared and thus a correct detection is made.

The microcontroller was programmed to MPLAB X IDE v3.45 using the MPLAB HARMONY Configurator v1.09.

2.2.1 STATE MACHINE

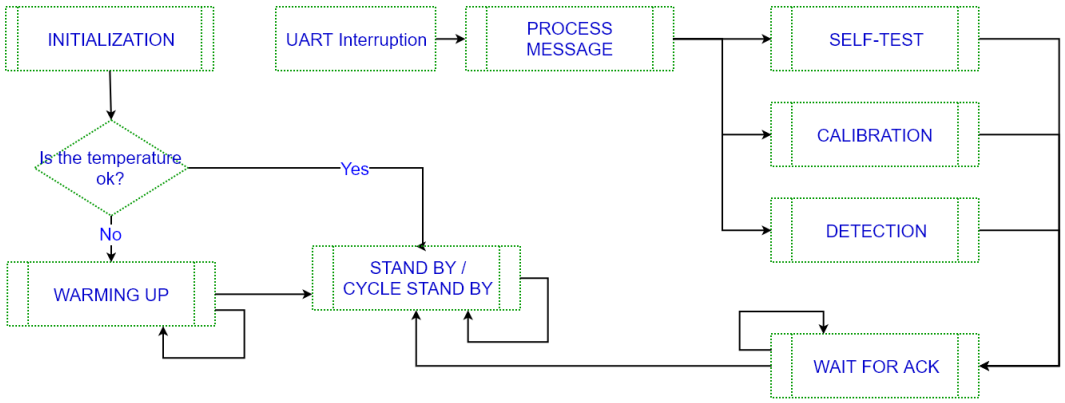

Figure 4: Simplified flowchart of the state machine behavior (Vargas Luna, 2016)

The device is designed to work as a state machine. The first state is the initialization, where the system variables are initialized and a check, if an active warm up to increase the temperature faster is required. If this state is called during initialization, a temperature measurement is taken and the system is warmed up to a certain temperature value. Thereafter, the standby mode is activated, which is the default state of the device. In this mode, the device waits for a request from the main unit. In addition, the operational amplifier (OPA) temperature is monitored and if the temperature reaches a given threshold of 45°C, the fan is started. Once the calibration detection cycle is active the cycle standby mode gets activated. It is conceptually similar to the standby mode but with the difference that the system is connected to the coil. The self-test analyzes and evaluates the internal systems. Another mode is the calibration, described in section 2.2.3, which measures the voltage level of the coil and saves the value as the reference value for each position of the coil. During this process it is important that the system seat is completely empty, since any metal in the immediate vicinity of the chair could compromise the calibration reliability. After a successful calibration, the recognition phase starts. Here the actual metal detection takes place by measuring the voltage level and comparing this value with the reference value. The voltage is evaluated along the same positions in which the calibration took place. If a metal is present in one position, the voltage level changes during the measurement. This value is compared with the previously measured reference value and an error message is displayed on the control screen. After that, the detection stars again.

Once the system responds to the main box instruction an acknowledgment message (ACK) is awaited. This phase is intended to support the UART protocol and is called after a command or response has been sent to the box. The confirmation must be made within a limited period of time. Figure 4 shows a flowchart of the state machine behavior. Most of the time the state machine behavior is in the standby mode or in the cycle state until a chain is received and another action is taken. In addition to these main states, other three commands are also

implemented. First, a watchdog sends an acknowledgment message to the box to proof the responsiveness of the monitor. Furthermore, a service allows accessing specific parameter values to assess the system functionality. At last a state request allows requesting the current state of the system.

2.2.2 UART PROTOCOL

The main communication between the monitor and the stimulation box happens via UART. Frames of 3, 10 or 12 bytes are exchanged over this communication port, either long or short answers are given. The 10 byte long answers contain the command and responses regarding the system itself and the 3 byte short answers are confirmations of the received messages or ACK. The 12 byte frames are reserved for service commands. All messages or frames start with a Start Of Heading (SOH) — '&' for commands and responses and '$' for acknowledgment messages— and finish with an End Of Frame (EOF), which is 0x0A ('\n') in all cases. Figure 5 shows the sequence of the messages defined in the UART protocol. See Table 12 and Table 13 in the appendix B for the full set of commands and responses available.

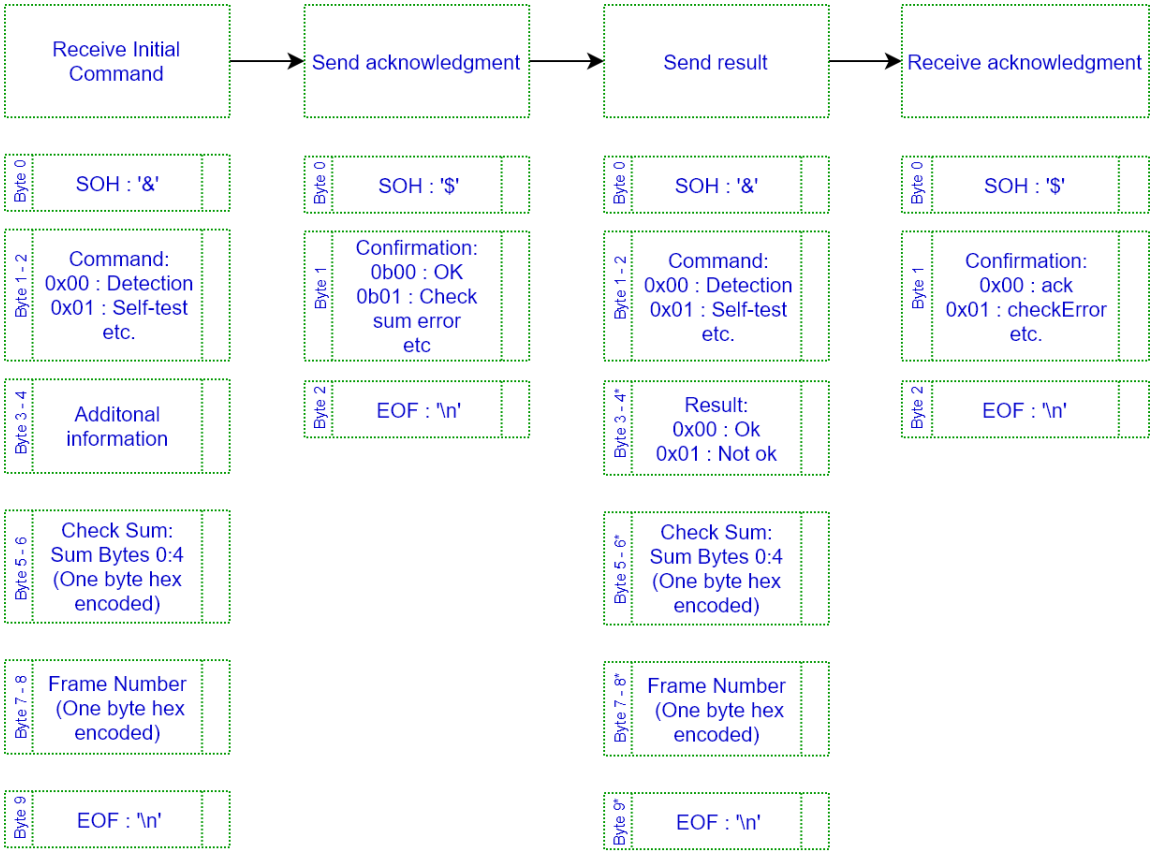

Figure 5: UART communication protocol sequence (Vargas Luna, 2016)
* When answering a service command, the result section uses 4 bytes instead of 2 bytes, which increases the frame size from 10 bytes to 12 bytes

The checksum is the sum of the American Standard Code for Information Interchange (ASCII) values of the bytes 1 to 4 and is implemented to verify the correct reception of information.

Additionally, a frame counter is used to track the transmission and reception of information and avoid the loss of packages.

Since the metal monitor has no access to the current state of the overall system, it is important that when receiving an initial command, additional information required to execute a given command is send. The position of the coil is important because of the structural design of the PelviPower system, the amount of metal surrounding the coil varies along the coil's path, changing the detection levels up to 13%. For a service command, additional information bytes are used to specify which internal parameter is wanted. The available commands which the device is programmed to understand and answer are listed in the appendix B (Table 12). In order to facilitate the correct communication, short acknowledge messages are also implemented and listed in the appendix B (Table 13).

2.2.3 Calibration and Detection Processes

A major problem for metal detection is the massive amount of metal in the design of the chair and the coil. As already mentioned, various metal structures are surrounding the coil along its path. In addition, the effect of the metal core of the coil changes, although it is constant in volume, as soon as a stimulation pulse is given due to a magnetic remanence on the material. Magnetic remanence increases the measured voltages when no metal is present. This difference decreases over time and estimates that the voltage level returns to its original value after more than 70 minutes when everything else remains constant. This phenomenon varies depending on the applied stimulation pulses, and since the pulses are not monitored, the system cannot compensate for these changes. In view of the very slow rate of change, when the calibration and metal detection process is carried out in a short period of time, it is possible to consider the changes due to the magnetic remanence as constant.

Figure 6: Coil Positions for the calibration process

The calibration process is performed continuously, starting with the empty chair and taking place in eleven steps starting with the reference position of 0%, which can be seen in Figure 6, and moving the coil towards 100% in steps of 10%. In the reference position the frequency calibration is performed, the fan is turned on and the relays are closed. After the initial calibration, the coil moves every 10% to a new position and recalibrates the calibration. After ten steps the coil is in position 100% and the calibration stops.

After a successful calibration, the detection of the patient starts. The patient sits on the chair and every 10% steps the coil movement stops and a measurement is carried out. Thereafter, this measured value is compared with the value of the calibration. Then a metal detection can be requested at any point of the locations - ideally at all locations. It is important to note that in a ScanOn mode from calibration to detection, when no metal is detected and completed at a coil position at 0%, the system remains in a coil position of 0%. This is important because in the ScanOn mode the system is connected to the high-power electronics of the device and therefore any stimulation during this time can damage the system. Once all calibration points have been acquired, the detection can be performed in any location sequence. If a piece of metal is detected, the measurement stops and a warning signal is displayed on the control screen. For the repetition of the measurement, the coil is brought back to the initial position and the measurement starts again.

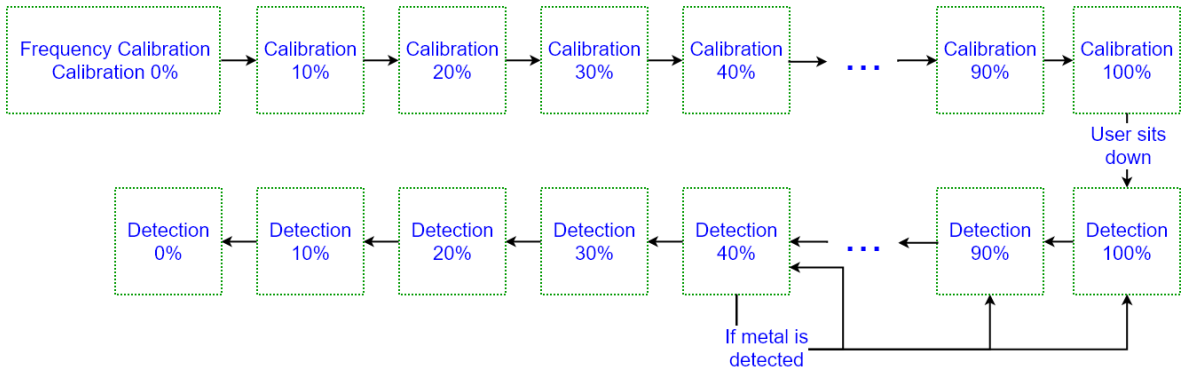

Figure 7: Recommended procedure for calibration and detection cycle (Vargas Luna, 2016)

To increase the safety of the system, the entire distance is examined via the coil. This allows the system to detect metals even if the patient is moving during the treatment. Figure 7 shows the calibration – detection process. Every box represents a command send to the metal monitor.

Figure 8 shows the flowchart of the software implemented in the metal monitor and the possible errors. The frequency calibration process, shown as a single box in Figure 8, consists of a frequency sweep beginning 20Hz before the last used measurement frequency and allows compensating differences due to the system temperature. There are two possible conditions for determining the measurement frequency. First, two samples in a row over a minimum value

(650) and below a maximum value (900) to prevent the voltage from rising to an unstable level and to prevent saturation because the voltage is higher at higher coil positions. The second condition is the reaching of the resonance frequency where the minimum value was not reached, but a further increase would reduce the voltage levels and therefore the resolution of the system.

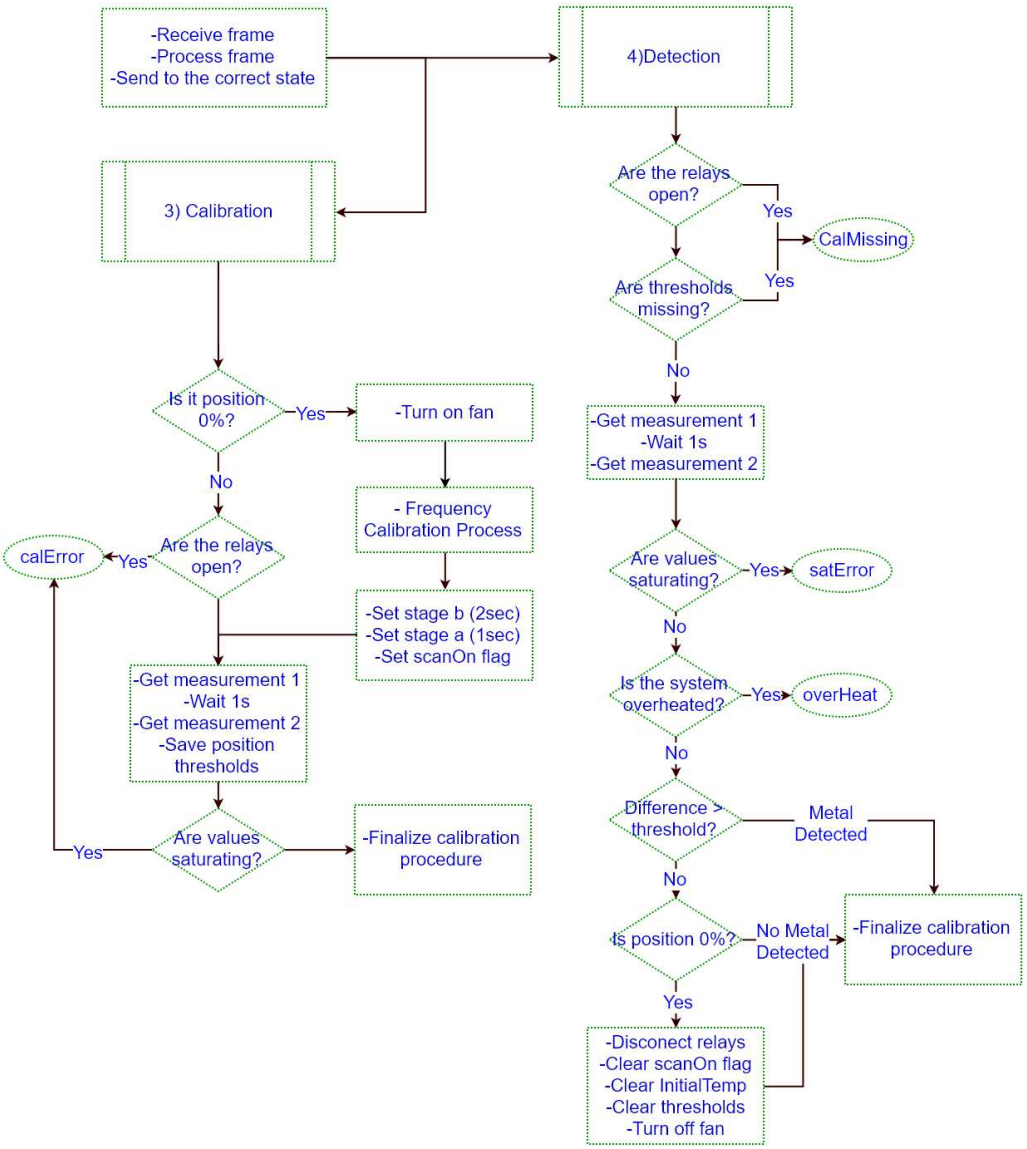

Figure 8: Flowchart of the calibration and detection processes in the metal monitor (Vargas Luna, 2016)

2.2.4 Temperature Control

The heating of the system due to the power requirement cannot be neglected in the system. The OPA548 main operational amplifier is the most temperature-dependent, as it drives a current of up to two amps at ±15V. Although the individual measurements are relatively short (400ms) and do not affect the temperature of the system, the implemented sampling method requires continuous sampling. This significantly increases the temperature of the power amplifier. Therefore, a fan was added to sink the temperature of the operational amplifier.

The sensor was calibrated based on two cycles of heating cooling, with the temperature values (T_M) measured by the Analog to Digital Converter (ADC) of the microcontroller and the real temperature measured by a type K thermocouple (T_R) disposed on the heat sink. Afterwards, a comparison of the two temperatures takes place. As can be seen in Figure 9, the data shows a linear behavior in the range of 25°C to 53°C.

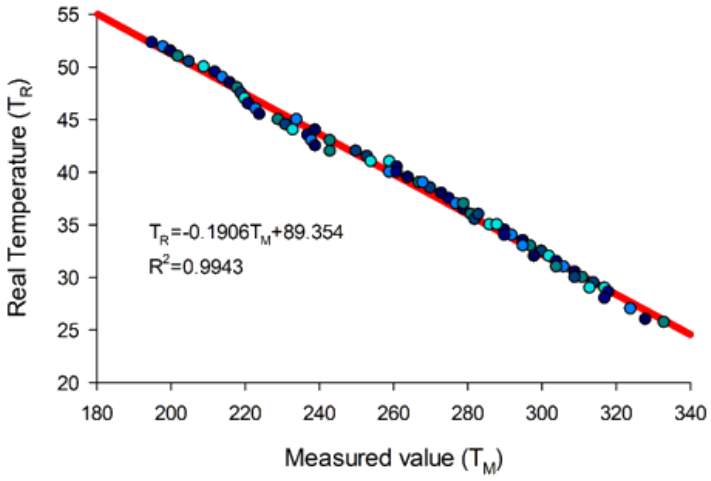

Figure 9: Relation of temperature values (T_M) by the ADC of the microcontroller and the real temperature by a thermocouple of type K (T_R) (Vargas Luna, 2016)

The temperature control is done on two different levels: standby mode and ScanOn mode. During standby, the temperature is monitored continuously. If the temperature reaches a value of 55°C, the system is blocked, since such a temperature could produce current drifts large enough to compromise the results. To avoid this, the fan is turned on if the system reaches a temperature of 45°C. During ScanOn mode, the fan turns on during frequency calibration. After the first calibration at the coil position 0%, an initial temperature is stored. The temperature control system is able to keep the system temperature constant so that drifting due to heating of the OPA is negligible by turning the fan on as soon as the temperature reaches this value and turning the fan off when the temperature drops below that value. The quiescent currents flowing through the operational amplifier produce an additional heat source that raises the temperature until it reaches a plateau. When the system is initialized and the OPA is relatively cold, the heating due to these quiescent currents could add up voltage variations to the measurements, which can compromise the results and cause false negatives. Figure 10 observed an example of how the initial warming of the device behaves in the case of 33°C. The temperature rise during the first minute is caused by the active heating. The aim of this warming is the rapid achievement of a temperature level to prevent an additional influence on the measurement. As shown in Figure 10 (OPA Temp Passive), the stabilization of the temperature takes about 15 minutes.

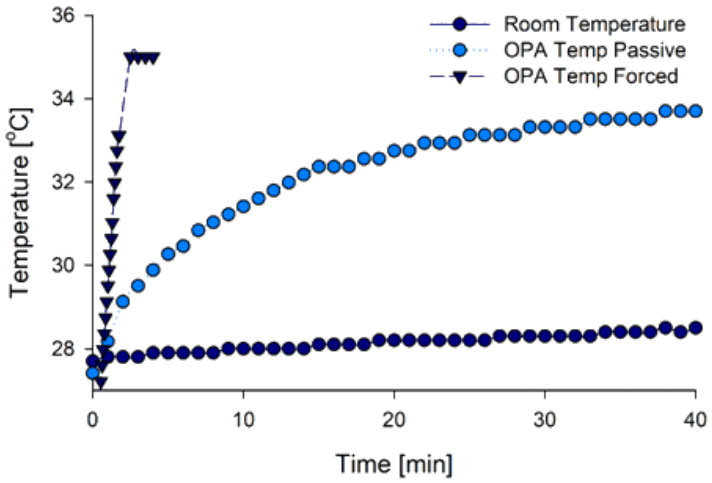

Figure 10: Example of how the initial warming of the device behaves (Vargas Luna, 2016)

For the purposes of the calibration detection cycle, a maximum temperature increment of 1°C is allowed. This prevents the reliability of the system from being affected. To overcome the heating, active heating is performed to increase the temperature faster (Figure 10 OPA Temp forced). This feature should allow the operational amplifier temperature to rise to plateau temperature or higher, allowing the fan to prevent overheating during the calibration acquisition cycle. Since there is no information on the room temperature, a fixed value of 32°C was chosen, which is in most cases higher than the plateau.

2.2.5 BOOTLOADER

A bootloader is included into the microcontroller, which allows the PelviPower box to make software updates directly through the UART port.

The bootloader algorithm is based on the application note from Microchip Technology Inc. AN1388: PIC32 bootloader, and was implemented with the help of the Harmony Framework. Every time the microcontroller is started, the bootloader is invoked. A trigger pin was implemented to allow the PelviPower system to decide between starting the bootloader or go to the main state machine.

CHAPTER

3 TEMPERATURE MEASUREMENTS

In this chapter, the temperature measurements are evaluated with the aim to identify the regions of interest. These regions are the respective positions and distances where the power density is above the critical 40mW/cm^2 mark and damage to the surrounding tissue could occur. For further sensitivity measurements, these regions are particularly important to detect, see chapter 4.

This chapter is divided into four sections. The first section explains the equipment and the used materials. First, the used PonteMed PelviPower system and the coil characteristics will be evaluated. Afterwards, the material samples and the infrared thermometer to record the values are described. The next section describes the methods of the measurement. First, the worst case scenario is created to get the standard settings for the temperature and sensibility measurements. Afterwards, the used positions and distances are defined on the seat of the device and the processing of the measurement is described. The next section presents the results of the individual measurements. The chapter ends with the description and discussion of these results.

3.1 MATERIALS

3.1.1 PONTEMED PELVIPOWER SYSTEM

The PelviPower Magnetic Field Trainer is a device for the muscular strengthening of an insufficient pelvic and the surrounding muscles. The technology in this systems is the “repetitive peripheral muscle stimulation” (RPMS) or “extracorporal magnetic stimulation”, wherein the magnetic field is generated by an external source, the therapy chair. As can be seen in Figure 11, the system consists of a magnetic coil embedded below the seat surface.

Figure 11: PelviPower Magnetic Field Trainer with the magnetic field on the seat surface (PonteMed A. , 2016)

The electrical induction produces a potential shift which leads to a depolarization of the peripheral nerves and contractions of the associated muscles. Similarly to electrical stimulation, single pulses produce single twitches, while titanic contractions, when individual contractions can no longer be distinguished, are produced by fusion frequencies between 15Hz and 25Hz depending on the muscle tone. The system allows the setting of different frequencies (PonteMed, Bedienungsanleitung, 2016) (PonteMed, Instruktions-Handout, 2016)(TENS-EMS-Reizstrom).

- Low frequency between 5Hz- 15Hz activates the blood circulation in the respective body areas (Dobsák P, 2006).
- In the range between 15Hz- 35Hz, the muscle tension is controlled. Around 25Hz, maximum muscle contraction is achieved (Kenneth W. Hinchcliff, 2014).
- Between 35Hz- 50Hz the blood flow is stimulated and scarring is solved (Kraft, 2010).

In addition, different therapy sessions with different intensities can be selected. From level 1, which means 20% of the maximum intensity and level 5, which is the maximum intensity. The stimulation or pause time during the individual pulses can additionally be changed.

With the help of the different sitting positions (Figure 12 number 3), the individual needs of the patients can be considered and a comfortable and effective sitting position can be found. For optimum training, the coil can be moved 18cm forward and backward to stimulate different areas (Figure 12 number 2) of the body (PonteMed, Bedienungsanleitung, 2016) (PonteMed, Instruktions-Handout, 2016).

Figure 12: Composition of the PelviPower Magnetic Field Trainer (1) Touch Screen (2) Adjustable magnetic field coil (3) Seating position (4) Adjustable armrest (5) Covers (PonteMed A. , 2016)

3.1.2 COIL CHARACTERISTICS

The coil is designed for stimulation of the pelvic floor and the surrounding muscles. The magnetic coil generates therefore a magnetic field of repetitive and short magnetic pulses of 200µs to 500µs and a flux density of up to 1 Tesla. Depending on the intensity, the penetration depth is between 5cm and 15cm (PonteMed, Instruktions-Handout, 2016).

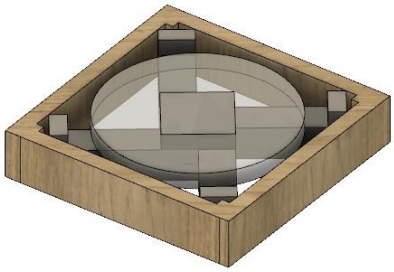

Figure 13: 3-dimensional overview of the used coil

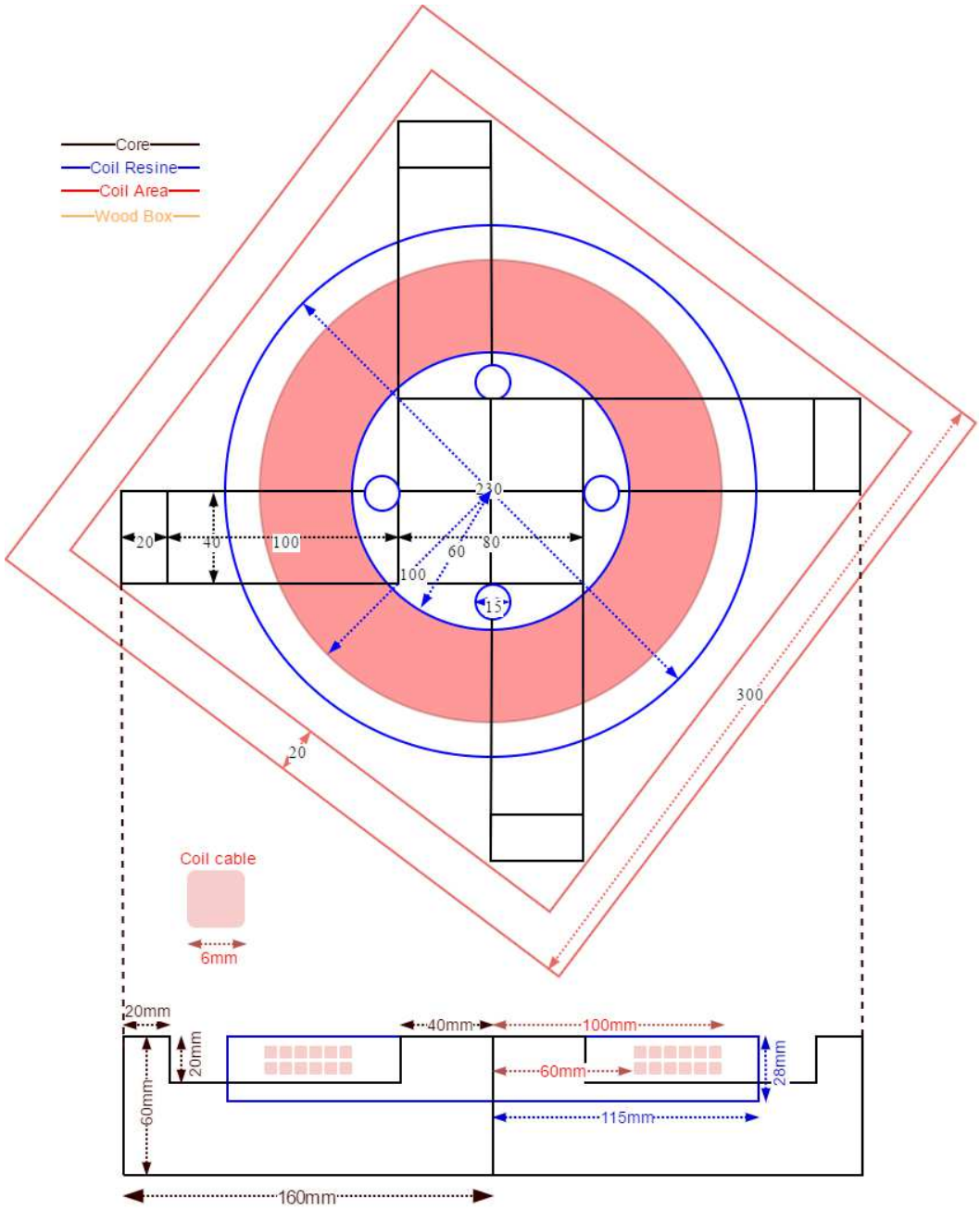

Figure 14: Overview and dimensions of the used coil

Figure 13 and Figure 14 show the overview and dimensions of the used coil. The inner diameter of the coil is 60mm and the outer diameter is 230mm.The windings are made of litz wire with a

diameter of 6mm. To reduce the skin effect, the wire consists of individually insulated copper wire strands that are twisted. The coil area is located between 60mm and 100mm from the center and is made of two spiral layers of wire with six windings per layer. For the amplification of the magnetic field, a laminated core is used. A square core with a dimension of 80mm is at the center of the coil. The core consists of four stacks, to reduce the eddy currents and four magnetic poles in the corner of the housing. Each stack has a side length of 40mm and a length of 160mm and consists of insulated metal sheets. Overall the housing of the coil consists of wood and has a square shape with a length of 300mm, the housing itself is 20mm wide and has a height of 60mm (Nalbach, 2016)(Reth, 1959)(Kühn, 1963).

Table 2 shows the characteristics of the used coil.

Table 2: Coil characteristics

Parameter	Value
Coil Resistance	<100mΩ
Capacitor	2,2 µF
Resonance frequency	8,560kHz
Inductance	≈157µH
# wires on the cable	~600
Layers per segment	80

3.1.3 IMPLANTS TESTED

As explained in section 1.2.1 there are several materials that can be influenced by magnetic stimulation. In order to test more realistic scenarios, the main metal samples are part of different artificial hip replacement systems, which are used for the treatment of a joint failure. The main parts for a total hip replacement are the stem, hip head, and acetabulum. Since the stem is usually large, we used only the hip head and the acetabulum parts.

Four different metal samples were investigated: a flat cylinder of iron, a cobalt-chrome sphere shaped hip head (part number NK544K, BBRAUN), a titanium (part number NA650, BBRAUN) and a titanium-aluminum alloy acetabulum prosthesis (part number NH044T, BBRAUN) (Aesculap, 2017). Metallic materials used for surgical implants are standardized and described in the ISO 5832. The ISO 5832 consists of several parts, including the used materials such a CoCr29Mo hip head, described in the ISO 5832- 12 and the Ti6Al4V parts described in the ISO

5832-2.(5832-2, 2007) (5832-12, 2007). A size comparison of the used samples can be seen in Figure 15. Table 3 shows the different materials. It highlights the most important material properties and characteristics of each sample.

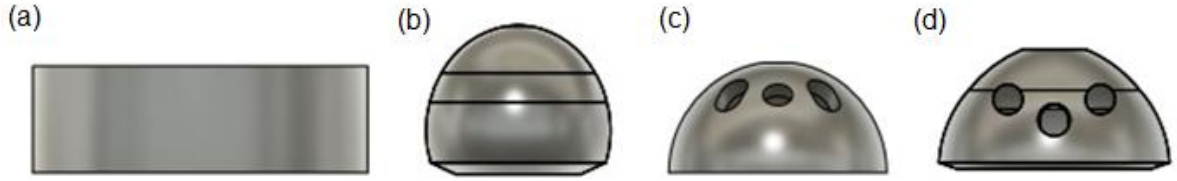

Figure 15: Size comparison of the used samples (a) Iron (b) CoCr29Mo (c) Ti (d) Ti6Al4V

Table 3: Material properties and characteristics (Cadena, 2010) (MatWeb, 2017) (Rodney Boyer, 1994) (Engineering, 2017)(Processors, 2012)
(1) Since no exact material properties were found for CoCr29Mo, the values for a CoCr alloy were entered

		Iron	CoCr Alloy(1)	Ti6Al4V	Ti
MATERIAL PROPERTIES	Magnetic permeability μ [H/m]	5000	<1,2	1,00005	1,0000013
	Electrical resistance ρ [$\mu\Omega$cm]	9,71	90,76	178	55,4
	Specific heat c_p [kJ/kgK]	0,450	0,452	0,540	0,540
MATERIAL CHARACTERIS	Surface area [cm^2]	163,36	67,46	81,62	82,22
	Volume [cm^3]	125,7	35,18	18,3	15,83
	Mass [kg]	1	0,16698	0,1062	0,0681

A 1kg heavy iron flat cylinder sample (Figure 16) was also included in the measurement as representative data for other non-biocompatible materials and since this material cannot be found in any kind of implant sample in this form, it was taken as a reference value. The sample has a diameter of 80mm and a high of 25mm. The surface area is 163,36cm^2 and the volume results in 125,7cm^3. On the basis of the material properties and characteristics, this sample

shows the highest inductive heating and thus the worst case scenario, described in section 3.2.1, of the measurements.

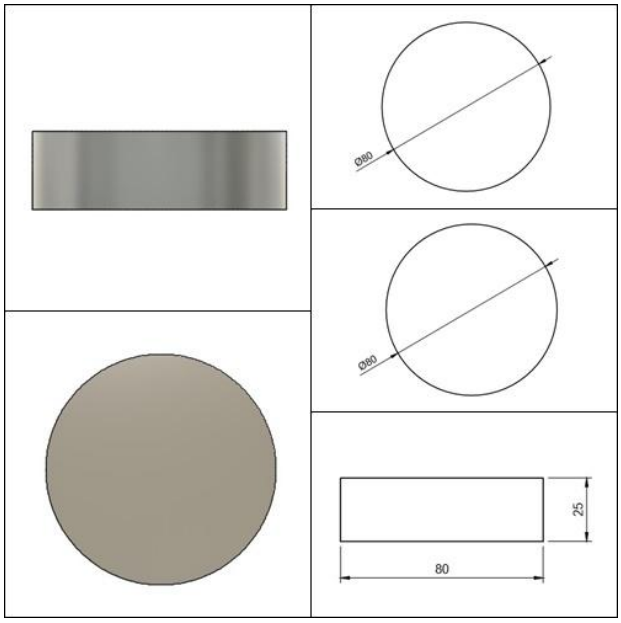

Figure 16: Overview and dimensions of the iron sample

The used cobalt-chromium-molybdenum sphere shaped hip head (Figure 17) is designed from the company BBRAUN Austria with the part number NK544K for the BiCONTACT® Hip Endoprosthesis System. It consists of 90,7% chromium, 5,8% molybdenum and 3,5% cobalt. This sample is a unipolar hip head with a diameter of 44mm, a surface area of 67,46cm^2 and a volume of 35,18cm^3. Because there is no accurate recording of the magnetic permeability and electrical resistance of CoCr29Mo, similar values were assumed as from the material CoCr alloy.

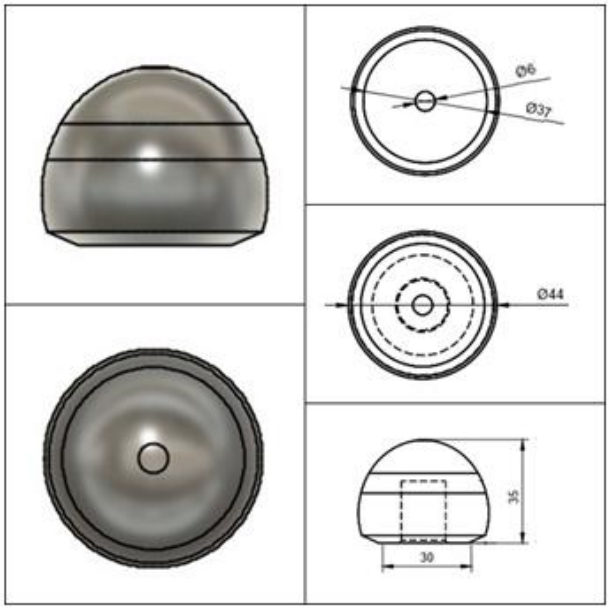

Figure 17: Overview and dimensions of the CoCr29Mo hip head

The titanium-aluminum alloy acetabulum prothesis (Figure 18) is designed from the company BBRAUN Austria with the part number NH044T for the BiCONTACT® Hip Endoprosthesis System. The composition consists of approximately 6% aluminum, 4% vanadium, <0.5% "other" and the rest of titanium. This sample belongs to the Plasmacup® implants with a diameter of 55mm, a surface area of 91,26cm^2 and a volume of 18,43cm^3.

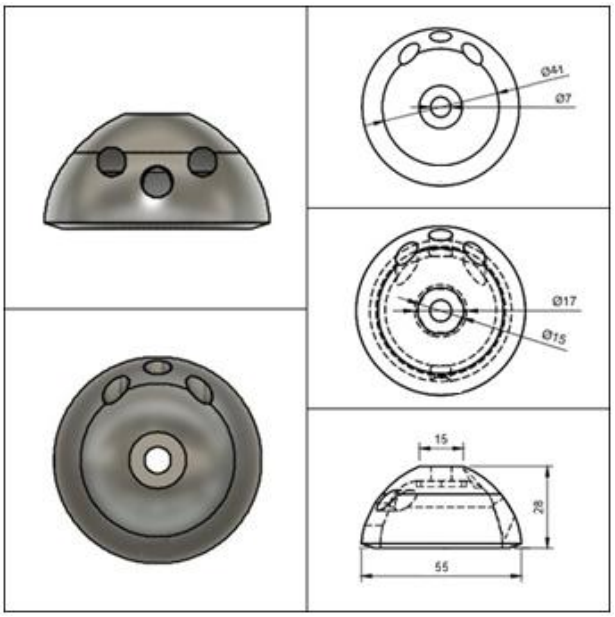

Figure 18: Overview and dimensions of the Ti6Al4V acetabulum

The titanium acetabulum prothesis (Figure 19) is designed from the company BBRAUN Austria with the part number NA650 for the BiCONTACT® Hip Endoprosthesis System. This sample has a diameter of 52mm, a surface area of 81,19cm^2 and a volume of 15,83cm^3.

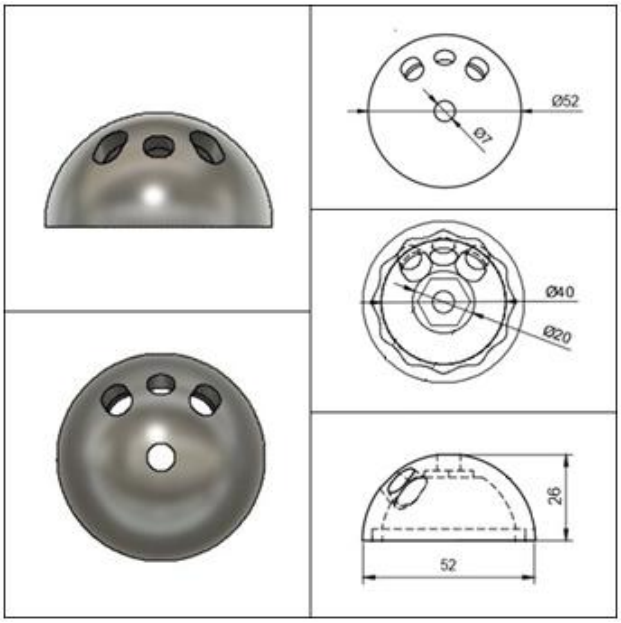

Figure 19: Overview and dimensions of the Ti acetabulum

3.1.4 INSTRUMENTATION

The resulting heating was monitored with a VOLTCRAFT IR-365 RF infrared thermometer (VOLTCRAFT Conrad Electronic AG, Wollerau, Switzerland) and evaluated with the associated software. An overview of the infrared thermometer is shown in Figure 20.

Figure 20: Overview and example of the VOLTCRAFT IR-365 RF infrared thermometer (a) side and (b) rear view (c) example of a measurement with the corresponding (d) wireless connection to the computer

This infrared thermometer detects the emitted, reflected and transmitted heat radiation of the object to be measured and converts this value into a temperature value. All samples were treated with a black mate spray car-varnish. This allows reducing artifact due to the infrared technology of the pyrometer, which is not reliable when shiny surfaces are being measured. For accurate measurement results, the object must be larger than the measuring point of the thermometer. Otherwise, temperature changes on the sample may occur and can affect these measurements. Depending on the size of the object, the distance between the thermometer and the object must be adjusted. It is important that the infrared thermometer is far enough away from the chair so that the magnetic field has no effect on the thermometer and thus no influence on the measurement. The thermometer is equipped with a 433MHz radio transmission of measured values to the computer and provides a cable-free transmission of the measured temperature values to the supplied software, which subsequently stores and further processes the values. The wireless transmission prevents additional influences of the magnetic field due to cables. An accuracy of ±1,5% of the measured value, corresponding to approximately ±2°C, was ensured (VOLTCRAFT Conrad Electronic AG) (Infrarot-Thermometer IR-365RF Operating instructions, 2005).

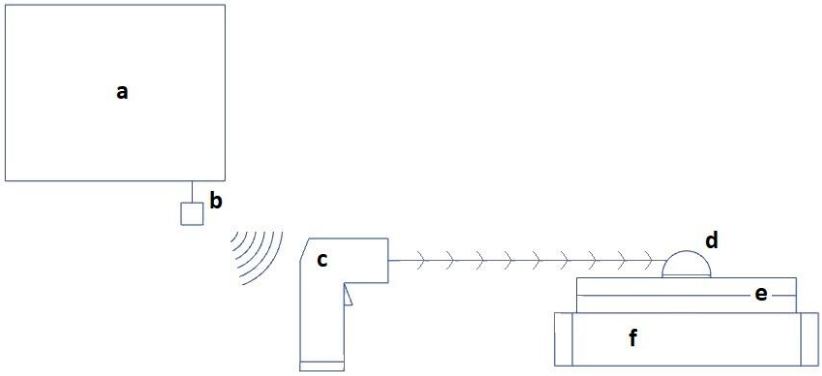

Figure 21: Instrumentation of the temperature measurement: (a) computer (b) wireless receiver (c) infrared thermometer IR-365RF (d) sample (e) plexiglas sheets (f) coil

As can be seen in Figure 21, the infrared thermometer (c) measures the temperature of the sample (d), which is measured at a defined distance, changeable by plexiglas sheets in a distance of 20mm up to 80mm (e), from the coil (f). The values are sent to the computer (a) via a wireless connection (b).

For evaluations, the temperature was recorded before the stimulation start, during the training and after the end of the stimulation. The resolution of the temperature in this device is 0,2°C. The temperature values are sent to the computer with a rate between 1 and 4 samples per second.

Table 4: Example of the recorded temperature measurement

Numbering	Data	Unit	Time	Time difference
1	26,10	C	11:01:55	0
2	26,00	C	11:01:55	0
3	26,20	C	11:01:56	1
4	26,20	C	11:01:56	1
5	26,20	C	11:01:57	2
6	26,20	C	11:01:57	2
7	26,20	C	11:01:57	2
8	26,20	C	11:01:58	3
9	26,20	C	11:01:58	3

An example of the stored list can be observed in Table 4 and consists of 4 columns and depending on the duration of the measurement, any number of rows. Depending on the start and end point, the number of measured values is usually between 2000 and 2200, with the first row as heading. In the first column, the rows are numbered, the second column contained the temperature values and the appropriate unit is comprised in the third column. The last column involved the time. The first row is removed for further processing in MATLAB (The MathWorks, Inc., Natrick, USA) and the time difference between the start and the respective measured value is calculated in the 5 column.

3.2 METHODS

As already mentioned in section 1.3.6 the various metallic samples are heating up in a magnetic field due to the eddy currents. Depending on the sample, position and distance between the seat surface and the sample, different temperatures and thus different power densities occurred. Since the device has a software limitation, the worst case scenario for the following measurements was first determined with the aim to find the device settings for the most influential adjustments. Thereafter, the various samples were placed at different positions and distances between seat surface and sample, and the temperature was measured during a treatment session using the infrared thermometer. Subsequently, the values were further processed and the results calculated and graphically evaluated in various programs. To guarantee the same measurements, the room temperature always fluctuated in the same ranges. It had been established that no significant changes in the measurements occurred with increasing room temperatures. In order to have the same initial conditions, the samples were cooled down after each measurement.

For the following temperature measurements, the sample was placed in the respective position and the corresponding distance between sample and seat surface. The infrared thermometer was placed in front of the chair according to the height so that the measurement took place in a horizontal line to the laser point on the sample. As already mentioned, the distance between the infrared thermometer and the sample was chosen so that on the one hand the infrared thermometer did not influence the measurement and on the other hand the measured point located only on the sample and thus the environment had no influence on the measurement. During the measurement, the temperature values were saved and then stored in a file for further processing. The further processing took place with the program MATLAB (The MathWorks, Inc., Natrick, USA). The PelviPower Magnetic Field Trainer allowed choosing between different training models. It was possible to select out between different frequency and intensity settings. The frequency range extended from 0Hz to 50Hz and the intensity levels could be adjusted from 0% to 100% as desired.

3.2.1 *Worst Case Scenario*

The aim of the worst case scenario was to determine the device settings, where the highest temperature difference between the beginning and the end of the training session occur. In these measurements, the coil in the seat of the PelviPower Magnetic Field Trainer was placed in the position 100%. To determine the Center of the coil, a magnetic flux detector (Figure 22) was used (Webcraft).

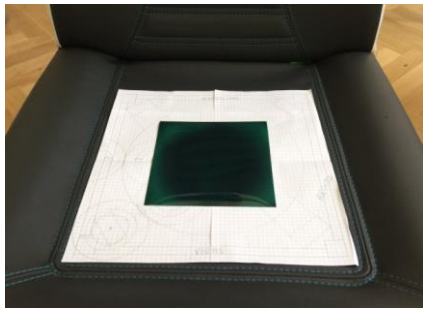

Figure 22: Testing the Center of the coil position with a magnetic field indicator film

Because of limitation of the PelviPower system, the stimulation frequency is restricted to 35Hz on the highest intensity. Since the frequency, the different materials, the stimulation time and the intensity influence the heating process, different scenarios were tested. As is apparent from the theory, the iron sample will be most heated. In the first step, we tested the different materials with the same settings over a defined period of time to make sure that the iron sample heats up the most and to confirm the theory. Based on the theory and consistent with the measurements, the iron sample was selected as a test object and placed at a distance of 20mm above the Center of the coil. Table 5 shows the temperature increase after 5 minutes of stimulation using different intensities, frequencies and stimulation time.

The results show the maximum heating at an intensity of 4, a frequency of 50Hz, a stimulation time of 12 seconds and a minimum pause period of 4 seconds.

Table 5: Intensity test

Intensity	Frequency [Hz]	Duration [min]	Temperature difference [°C]	Stimulation time [s]
4	50	5	15,7	12
6	35	5	13,7	12
4	50	5	15,4	8
6	35	5	11,2	8

3.2.2 PROCEDURE

As described in section 3.2.1, the stimulation setup was defined as an intensity of 4 with a frequency of 50Hz, a stimulation time of 12 seconds and a minimum pause period of 4 seconds. The measurement time was set to 15 minutes, which is the maximum duration time of the therapies.

As mentioned in section 3.1.3, the main tested materials were pure titanium, titanium-aluminum alloy Ti6AL4V, cobalt-chrome alloy CoCr29Mo and iron as reference material. As could be seen in Figure 23, the five used positions were the center of the coil (Center), above a pole (Corner), in the center of two poles (Edge), between the Center and the Edge (MidEdge) and between the Center and the Corner (MidCorner). In order to ensure the reliable and repeatable positions—thus the same conditions—a 1:1 paper template of the coil was made, and the positions were marked on the paper template. At the coil position of 100%, the template was fixed on the chair.

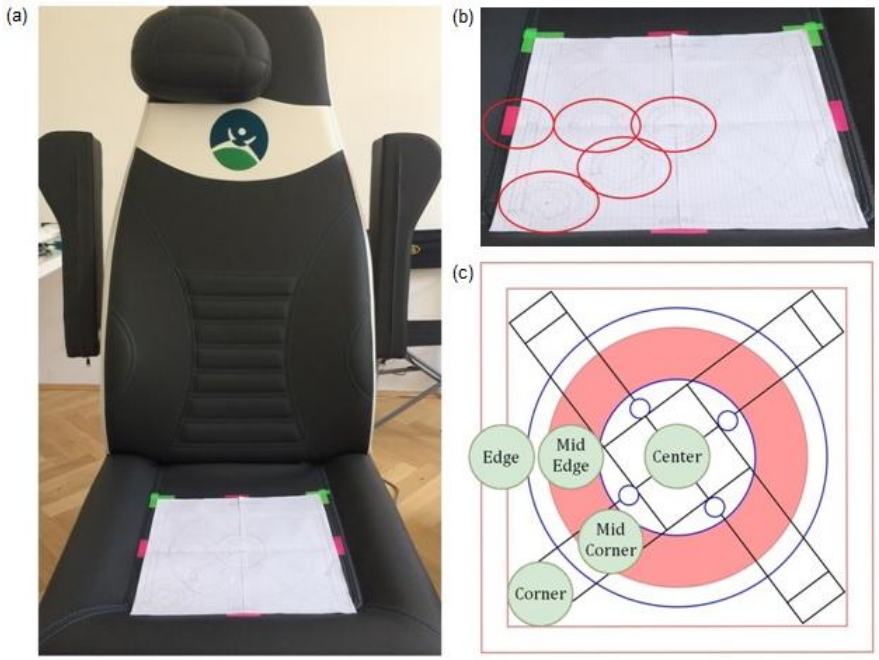

Figure 23: Paper template of the used positions: (a) PelviPower Magnetic Field Trainer with the paper template. The Center of the coil was determined with the previously used magnetic field indicator film (b) Overview of the five measured positions on the paper template and (c) the marked and named positions on the coil

The distance of the material samples to the seat surface is increased by stacking 20mm plexiglas sheets, which had no influence on the measurements. To prevent damaging of the chair's seat, all the measurements started at 20mm and increased up to 80mm. For the temperature measurements, 80 measurements were planned and a total of two repetitions were carried out. The subsequent evaluation was carried out with the respective maximum values of the measurement. Exceptions are the measurements with the Ti6Al4V sample, where only one repetition has been performed.

Table 6 shows a brief overview of all materials, positions, and distances between material and coil. It could be seen, all five different materials were measured in every position and distance and result in 20 measurements per sample and altogether in 80 measurements.

Table 6: Overview of all used materials, positions, and distances between sample and coil

Material	Position	Distance
Ti6Al4V	Center	20
Ti	MidCorner	40
CoCr29Mo	MidEdge	60
Iron	Corner	80
	Edge	

3.2.3 SIGNAL PROCESSING

As described in section 3.1.4 temperature measurements were taken with a VOLTCRAFT IR-365 RF infrared thermometer (VOLTCRAFT Conrad Electronic AG, Wollerau, Switzerland). Further processing to calculate the power density (Formula 8) took place with the software program MATLAB (The MathWorks, Inc., Natrick, USA). The power density depends on the specific heat c_p of the material, the mass m of the sample and the change of temperature ΔT at a given time t. To complete the analysis of the measurements, the basic values of the individual samples were defined in the program. These were the used intensity and frequency, but also material properties such as the mass, the specific heat, and the area. In addition, all used materials, positions and distances were defined. Subsequently, all 80 Excel files were read in and processed further. The first row and the third column were deleted. In the fourth column, the difference between the respective measurement and the initial value was calculated and multiplied by 86400 seconds, which corresponded to one day. The room temperature was the mean value of the first 40 temperature values.

$$P = c_p m \frac{\Delta T}{t}$$

Formula 8: Heat flux

To calculate the power and power density the temperature values were first smoothed and then filtered with a low-pass Butterworth filter, order 2. Subsequently, the data were further processed with a zero-phase digital filter, where the interpolation temperature values served as input data. The starting point and the maximum temperature from the interpolated values were

determined. These values were used to calculate the corresponding slope. Finally, the slope was used to calculate and output the power and power density according to the used sample.

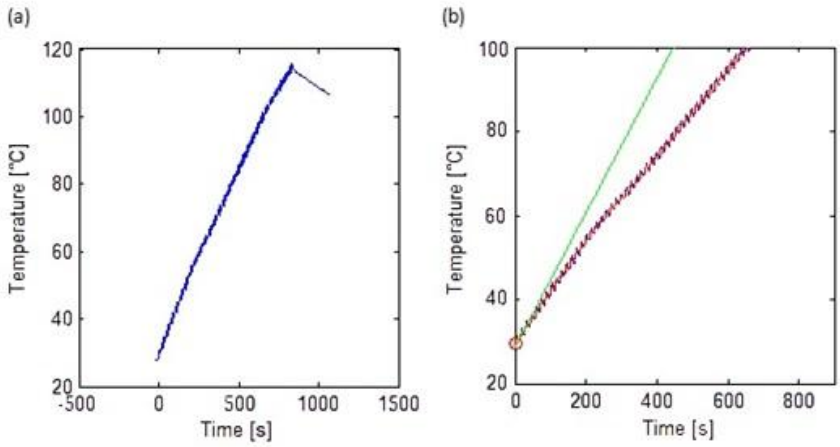

Figure 24: Plot example of the iron sample: (a) original data of the temperature measurement, starting at time zero. After the end of the measurement, the temperature drop can be seen (b) slightly magnified section of the maximum slope (green line) and the filtered temperature sequence (red line) with the starting point

Figure 24 shows a typical heating up of the iron sample in the Center at a distance of 20mm between seat surface and sample. The temperature is plotted on the x-axis and the time on the y-axis. Figure 24a) shows the original temperature curve of the iron sample, starting at the time zero. After the end of the measurement, the temperature drop can be seen. Figure 24b) shows the heated curve after the low-pass Butterworth filter, order 2. The red line represents the temperature profile after the low-pass Butterworth filter and the green line represents the maximum slope. The maximum slope sustained over 40 seconds was determined to calculate the power and power density.

3.3 RESULTS

This section presents the results of the power density calculated from the temperature measurements. The results that have been used are the maximum values of the individual repetitions. The procedures of the measurements were always the same for each measurement.

The results of each sample consist of two different diagrams. The first diagram shows the calculated power density over the different distances. This figure consists of two different parts. The graph highlights the power density from the different distances between the seat surface and the sample. The different measurement positions are indicated on the x-axis and y-axis. The corresponding power density is plotted on the z-axis. The second part of the figure is the 3-dimensional picture of the used coil, displayed on the x-axis and y-axis. Each figure shows the power density estimation at the distances of a) 20mm b) 40mm c) 60mm and d) 80mm between the sample and the seat surface. The second diagram shows a 2-dimensional line graph of the

different power densities in relation to the distances. For iron another diagram with a trend line at a distance of 100mm was inserted.

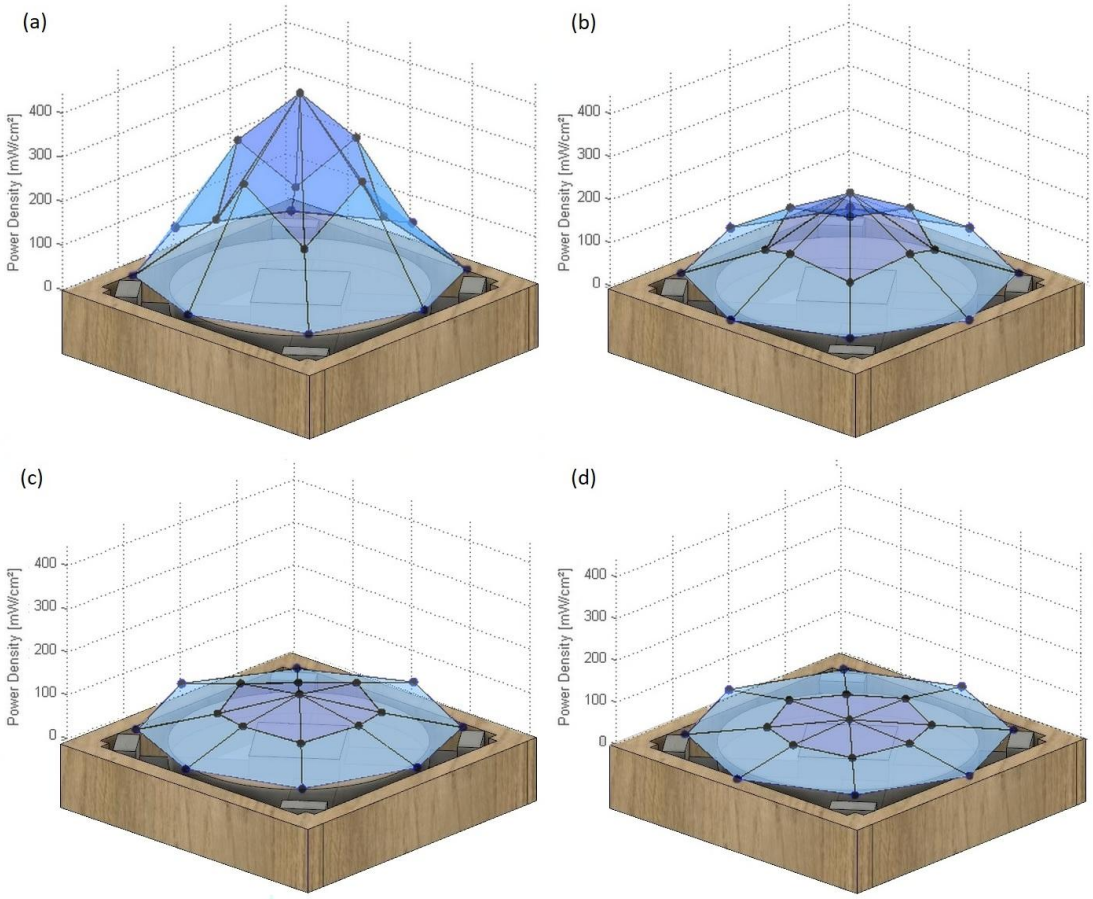

Figure 25: Iron: 3-dimensional diagram of the power density plotted over the positions (black marked) at a distance of (a) 20mm (b) 40mm (c) 60mm (d) 80mm between seat surface and sample

The power density sequence of the iron sample is represented in Figure 25. As expected, the iron sample had the highest power density of all samples. In the Center and at a distance of 20mm between the seat surface and sample the power density results in a value of 435,98mW/cm^2. In the MidEdge position the power density results in a value of 282,04mW/cm^2 and in the MidCorner position to a power density of 152,43mW/cm^2 for the first 20mm. In the Center and MidEdge position, the power density is still above the critical power density of 40mW/cm^2 in a range of 80mm. The power density in the Center results to 52,02mW/cm^2 and to 46,43mW/cm^2 in the MidEdge. In the position MidCorner the power density is below the critical mark at a distance of 80mm. In the Edge and Corner position, no critical power density can be measured at a distance of 20mm. As indicated in Figure 25 the power density decreases rapidly with increasing distances in each position.

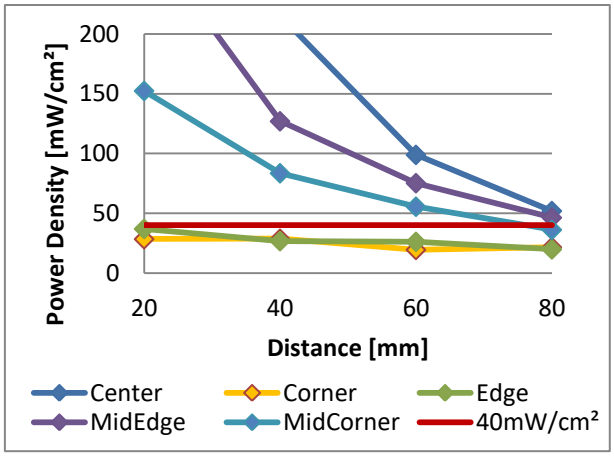

Figure 26: Iron: 2-dimensional line graph of the power density plotted over the distances

A 2-dimensional line graph of the different power density in relation to the distances can be seen in Figure 26. The red line marks the critical power density. Above this line, the surrounding tissue could be damaged by heating, therefore a reliable detection of the metal in this area is particularly important. It can be seen, that the power density shows a sharp decrease with increasing distances.

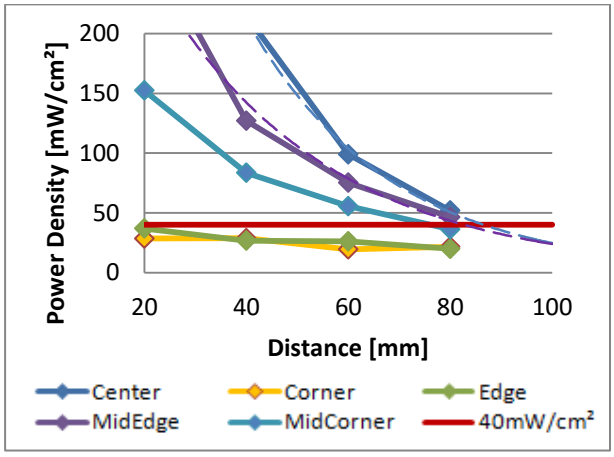

Figure 27: Iron: 2-dimensional line graph of the power density plotted over the distances. The dashed line shows the trend line of the respective position at a distance of 100mm

In the position Center and MidEdge, the power density was just above the critical mark in a range of 80mm. As can be seen in Figure 27 it can be assumed that distances higher than 80mm will produce a non-dangerous power density and the power density drops below the critical 40mW/cm² mark at a distance of 100mm.

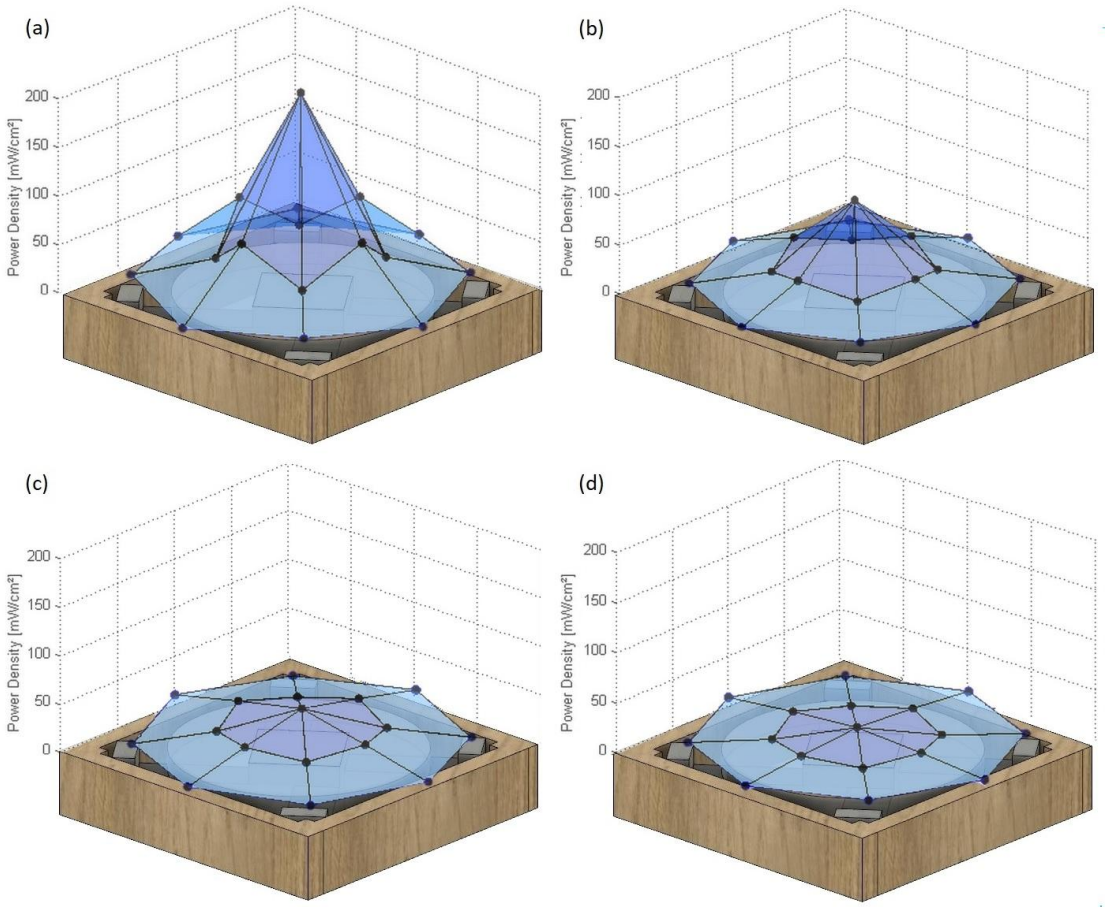

Figure 28: CoCr29Mo: 3-dimensional diagram of the power density plotted over the positions (black marked) at a distance of (a) 20mm (b) 40mm (c) 60mm (d) 80mm between seat surface and sample

Figure 28 shows the 3-dimensional diagram from the power density sequence of the CoCr29Mo sample. As can be seen in the figure, the power density, in each position, decreases rapidly with increasing distance. As expected, the highest values are measured in the Center of the coil. In this position and at a distance of 20mm between the seat surface and sample the power density results in a value of 204,83mW/cm^2. At a distance of 60mm, a power density of 40,94mW/cm^2 was measured. This is just above the critical power density of 40mW/cm^2. At a distance of 80mm, this value drops already to 19.12mW/cm^2. In the position MidEdge the power density is only at a distance of 20mm above the critical mark, with a power density of 73,84mW/cm^2. In all other positions, no dangerous power density was detected, even at a distance of 20mm between the seat surface and the sample.

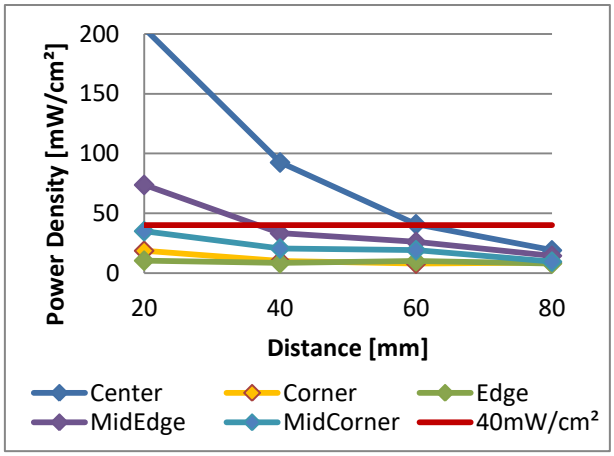

Figure 29: CoCr29Mo: 2-dimensional line graph of the power density plotted over the distances

Figure 29 summarizes a 2-dimensional line graph of the different power density in relation to the distance. The red line marks the critical power density. Above this line, the surrounding tissue could be damaged, therefore a reliable detection of the metal in this area is particularly important. As can be seen in Figure 29, the power density in the position of MidCorner, Edge, and Corner is still below the critical power density even at a distance of 20mm. With increasing distance, a fast decrease of the power density can be seen in the Center and MidEdge.

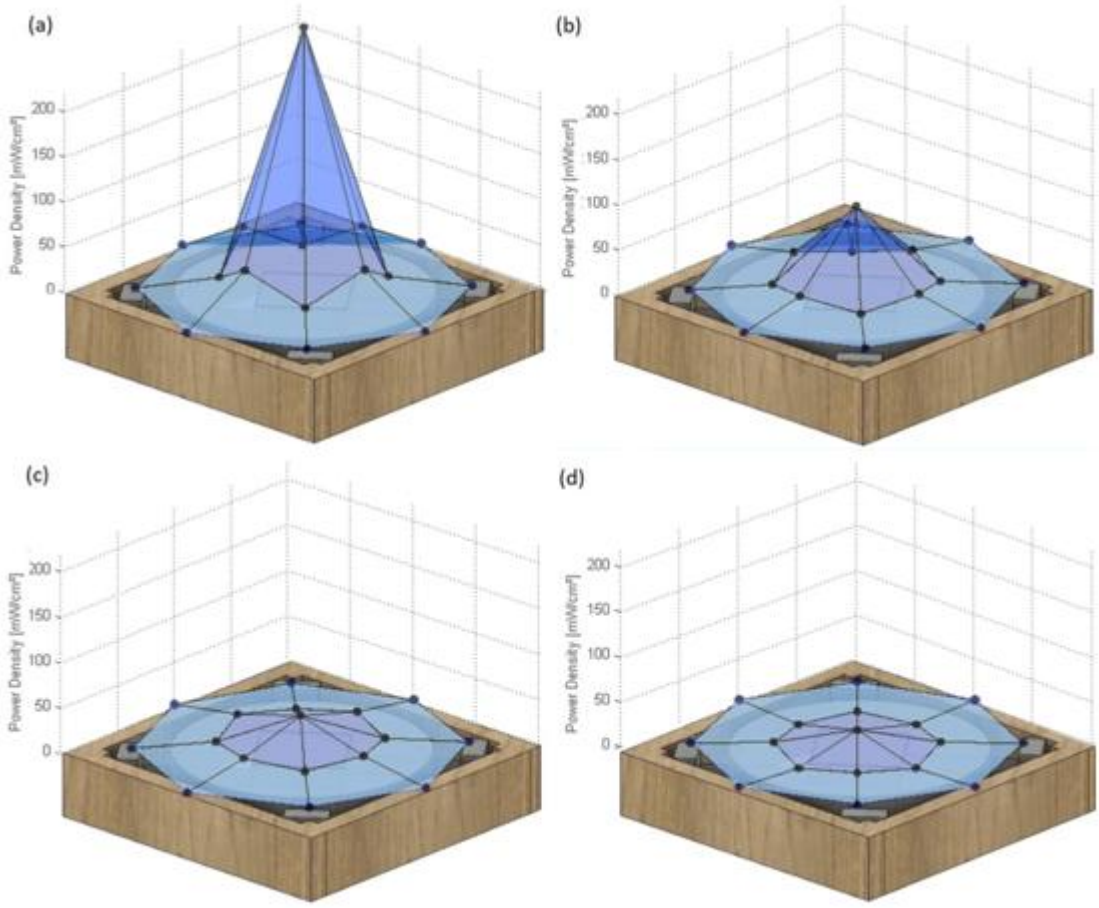

Figure 30: Ti: 3-dimensional diagram of the power density plotted over the positions (black marked) at a distance of (a) 20mm (b) 40mm (c) 60mm (d) 80mm between seat surface and sample

The power density sequence of pure titanium can be seen in Figure 30. The critical power density of 40mW/cm^2 occurs only in the Center of the coil in a range of 40mm and in the first 20mm of MidEdge. According to Figure 30, the power density remains nearly steady and, as expected, the highest values are detected in the Center of the coil. The power density in this position and at a distance of 20mm between seat surface and sample is 291,14mW/cm^2 and decreases very fast with increasing distance to a power density of 92,66mW/cm^2 at a distance of 40mm. At a distance of 60mm the power density is already below the critical mark. In the MidEdge position the power density results to 47,72mW/cm^2 at a distance of 20mm.

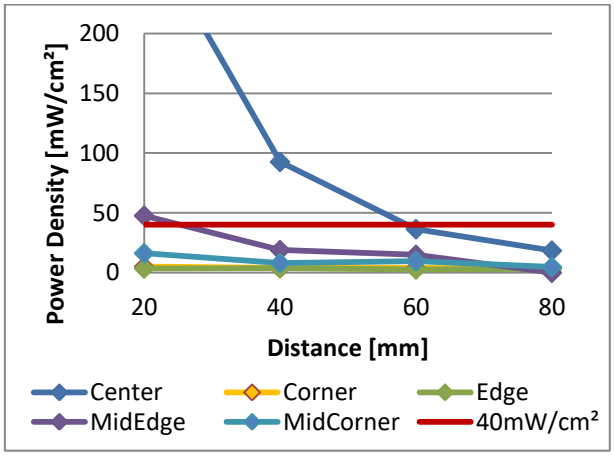

Figure 31: Ti: 2-dimensional line graph of the power density plotted over the distances

Figure 31 shows the power density of all positions in relation to the distance between coil and sample. The red line marks the critical power density. As can be seen the power density of MidCorner, Edge, and Corner is still below the critical power density even at a distance of 20mm. The power density in MidEdge starts in the critical area and decreases fast below this mark. A fast decrease of the power density with increasing distances can be seen in the Center.

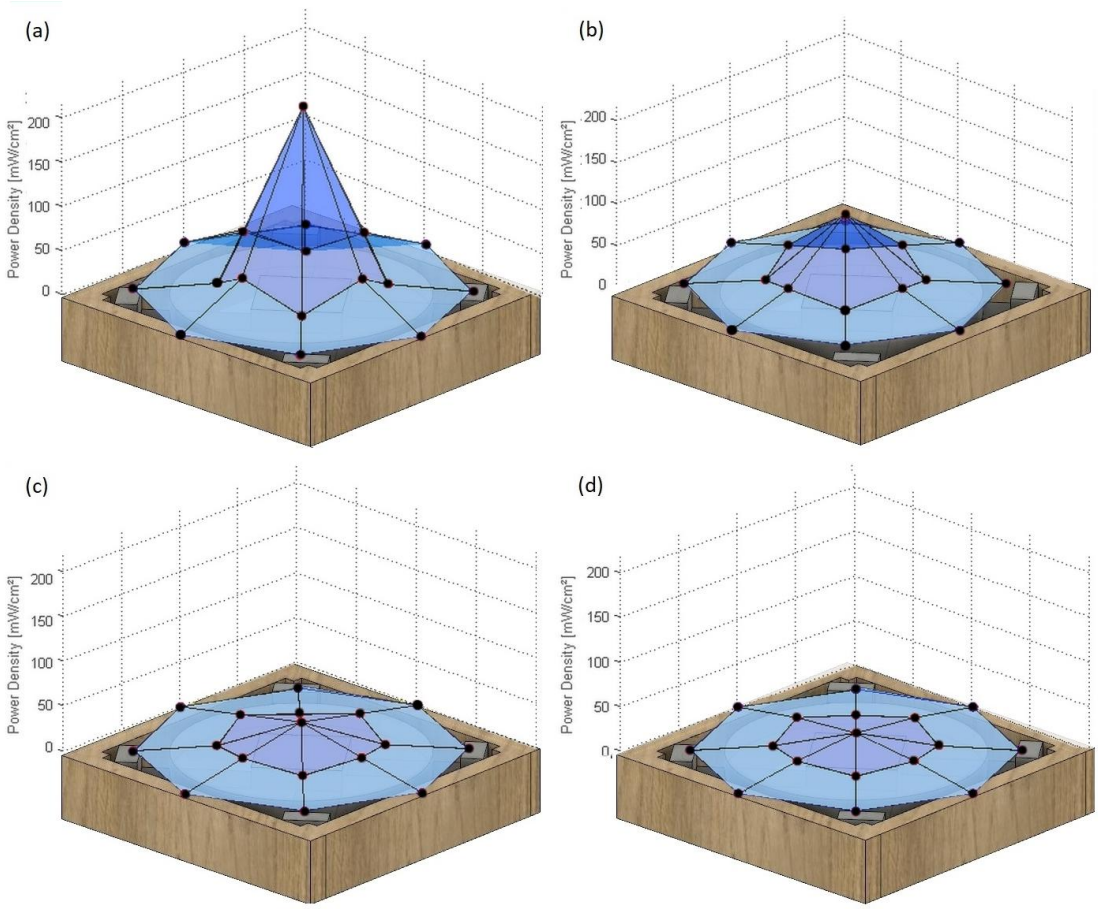

Figure 32: Ti6Al4V: 3-dimensional diagram of the power density plotted over the positions (black marked) at a distance of (a) 20mm (b) 40mm (c) 60mm (d) 80mm between seat surface and sample

Figure 32 shows the power density sequence of Ti6Al4V. According to this figure, the critical power density of 40mW/cm^2 only occurs in the Center of the coil in a range of 40mm and in MidEdge in the first 20mm. The power density exceeds to 213,55mW/cm^2 in the Center and at a distance of 20mm and decreases very fast with increasing distances to 86,86mW/cm^2 at a distance of 40mm. At a distance of 60mm the power density is already below the critical mark. In the MidEdge position the power density results to 44,85mW/cm^2 in the first 20mm and decreases fast with increasing distance. In the MidCorner, Edge and Corner position, the power density is still below the critical power density even at a distance of 20mm.

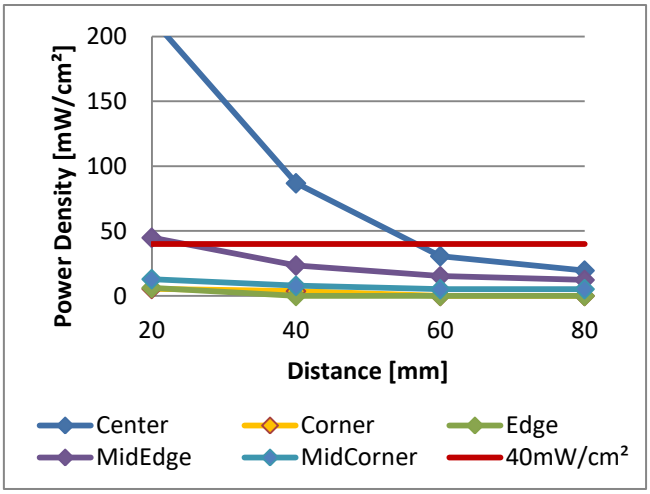

Figure 33: Ti6Al4V: 2-dimensional line graph of the power density plotted over the distances

Figure 33 shows the power density of all positions in relation to the distance between the seat surface and sample in a 2-dimensional line graph. The red line marks the critical power density. As can be seen in the diagram, the power density of the MidCorner, Edge and Corner position is below the critical power density the whole measurement. The power density in MidEdge starts just above the critical mark and decreases fast below the critical power density. A fast decrease of the power density with increasing distances can also be seen in the Center.

3.4 Discussion

This section compares the different samples based on their power density. The heating of the sample depends on the induced eddy currents. These eddy currents depend on the magnetic field and on the material properties and characteristics, as discussed in section 1.3.5, but also on the orientation to the magnetic field and generate heating due to the electrical resistance of the material. If higher eddy currents are induced, there is a higher heat transfer in the material and these results in a higher power density. Section 3.1.3 contains a table of the most important material properties and characteristics of the materials. As can be seen in the table, the specific heat is between 0,45kJ/kgK for Iron, and 0,54kJ/kgK, for Ti and Ti6Al4V. CoCr29Mo is close to the iron sample with a specific heat of 0,452kJ/kgK. The mass of the samples is between 0,0681kg for Ti, 0,1062kg for Ti6Al4V, 0,16698kg for CoCr29Mo and 1kg for Iron.

Based on the penetration depth, described in section 1.3.4, of the magnetic field, the stored values of the temperature difference between the beginning of the stimulation and the end of the stimulation can be explained well.

Figure 34 summarizes a 2-dimensional view of the power density at different distances to the coil and positions for each material. The x-axis shows the position and the y-axis shows the power density. As expected the power density in the Center position is the highest for all different samples and distances. These results can be explained by the design of the coil. Since

the square iron core consists of four laminated stacks and this occurs to the highest heating in this position. The corner forces the magnetic field closer to the coil surface, affecting the remaining positions. Comparing the position MidCorner and MidEdge, a reduced heating can be seen for MidCorner and also the Corner position influences the sample lower than in the Edge position.

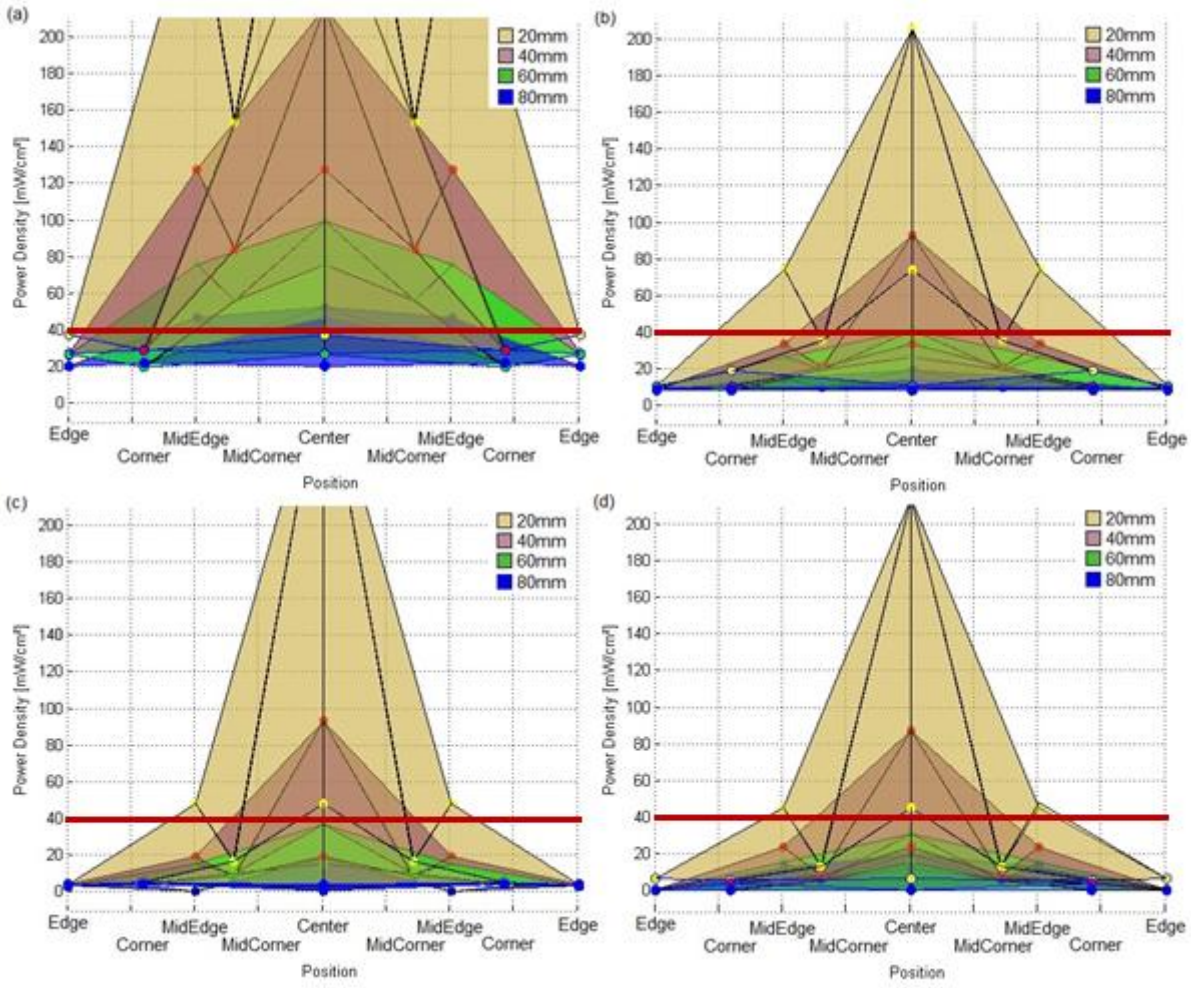

Figure 34: 2-dimensional diagram of the power density plotted over the positions at different distances for (a) iron (b) CoCr29Mo (c) Ti (d) Ti6Al4V. The red line corresponds to the critical power density of 40mW/cm²

As can be seen in Figure 34a) the iron sample shows a temperature difference between 4°C in the Corner, which corresponds to a power density of 28,51mW/cm² and 87,2°C in the Center, which corresponds to a power density of 435,98mW/cm², in the first 20mm. With increasing distances, these temperature values decrease rapidly resulting in only a few degrees difference in a distance of 80mm. In this distance the temperature difference is between 1,4°C in the Corner and 10,3°C in the Center, which corresponds to a power density of 21,71mW/cm² and 52,02mW/cm². In the Center position the temperature differences are measured between 10,3°C with a distance of 80mm and 87,2°C with a distance of 20mm corresponding to a power density of 52,02mW/cm² and 435,98mW/cm². For MidEdge and MidCorner, these temperature

differences are between 61°C and 37,9°C, corresponding to a power density of 282,04mW/cm² and 152,44mW/cm², with a distance of 20mm. With increasing distance, the material heats up worse and worse, so that there are only small temperature differences. In the Center and MidEdge position, the power densities are also above the critical 40mW/cm² mark even in a range of 80mm. Based on the trend line (Figure 27) it can be assumed that the power density is below the critical mark at a distance of 100mm in the positions Center and MidEdge. The iron sample has very small temperature changes in the Corner and Edge, resulting in the lowest power densities of 28,51mW/cm² and 37,02mW/cm², with a distance of 20mm. The power density takes very high values for a distance of 20mm, only a section up to 200mW/cm² was shown in this section to compare the different ranges.

As can be observed in Figure 34b) the temperature difference is between 1,8°C in the Corner, corresponding to a power density of 18,76mW/cm² and 78,4°C in the Center, corresponding to a power density of 204,84mW/cm² for CoCr29Mo and a distance of 20mm. At a distance of 80mm the temperature difference is between 0,8°C in the Corner and 9°C in the Center, which corresponds to a power density of 8,67mW/cm² and 19,13mW/cm². In the Center position, the temperature differences are measured between 9°C at a distance of 80mm and 78,4°C at a distance of 20mm corresponding to a power density of 19,13mW/cm² and 204,83mW/cm². At a distance of 60mm the Power Density is 40,93mW/cm² and is just above the critical mark. Similar results can be seen in the MidEdge position at a distance of 20mm. The remaining measurements arise in power densities below the critical 40mW/cm² mark and therefore represent no threat to the surrounding tissue. As can be seen in the diagram, the power density declines quickly and drops rapidly below the critical value.

As can be seen in Figure 34c) pure Ti occurs a temperature difference between 2,3°C in the Edge, which corresponds to a power density of 3,53mW/cm² and 95°C in the Center, which corresponds to a power density of 291,14mW/cm², at a distance of 20mm. At a distance of 80mm the temperature difference is between 0,5°C in the Corner and 15,3°C in the Center, which corresponds to a power density of 3,58mW/cm² and 18,44mW/cm². In the Center position, the temperature differences are between 15,3°C at a distance of 80mm and 95°C at a distance of 20mm, corresponding to a power density of 18,44mW/cm² and 291,14mW/cm². Up to a distance of 40mm, these values result in a power density that exceeds the critical mark. In the MidEdge position the critical power density occurs only in the first 20mm. The remaining measurements occur in power densities below the critical 40mW/cm² mark.

Finally the temperature difference, shown in Figure 34d) of Ti6Al4V at a distance of 20mm is measured between 2°C in the Corner, corresponding to a power density of 5,41mW/cm² and 101,3°C in the Center, corresponding to a power density of 213,55mW/cm². In the Center

position, the temperature differences are between 11,7°C at a distance of 80mm and 101,3°C at a distance of 20mm. This equals in a power density of 19,53mW/cm² and 213,55mW/cm². Up to a distance of 40mm, these values results in a power density that exceeds the critical mark. In the MidEdge position the critical power density occurs only in the first 20mm. The remaining measurements result in power densities below the critical 40mW/cm² mark. As detailed in the diagram, the power density decreases very quickly and drops rapidly below the critical power density. Since the power density in the Edge is the whole measurement in a non-hazardous area no additional measurements were taken.

Figure 35 summarizes the different samples compared with the respective distance. The red line represents the critical 40mW/cm² power density.

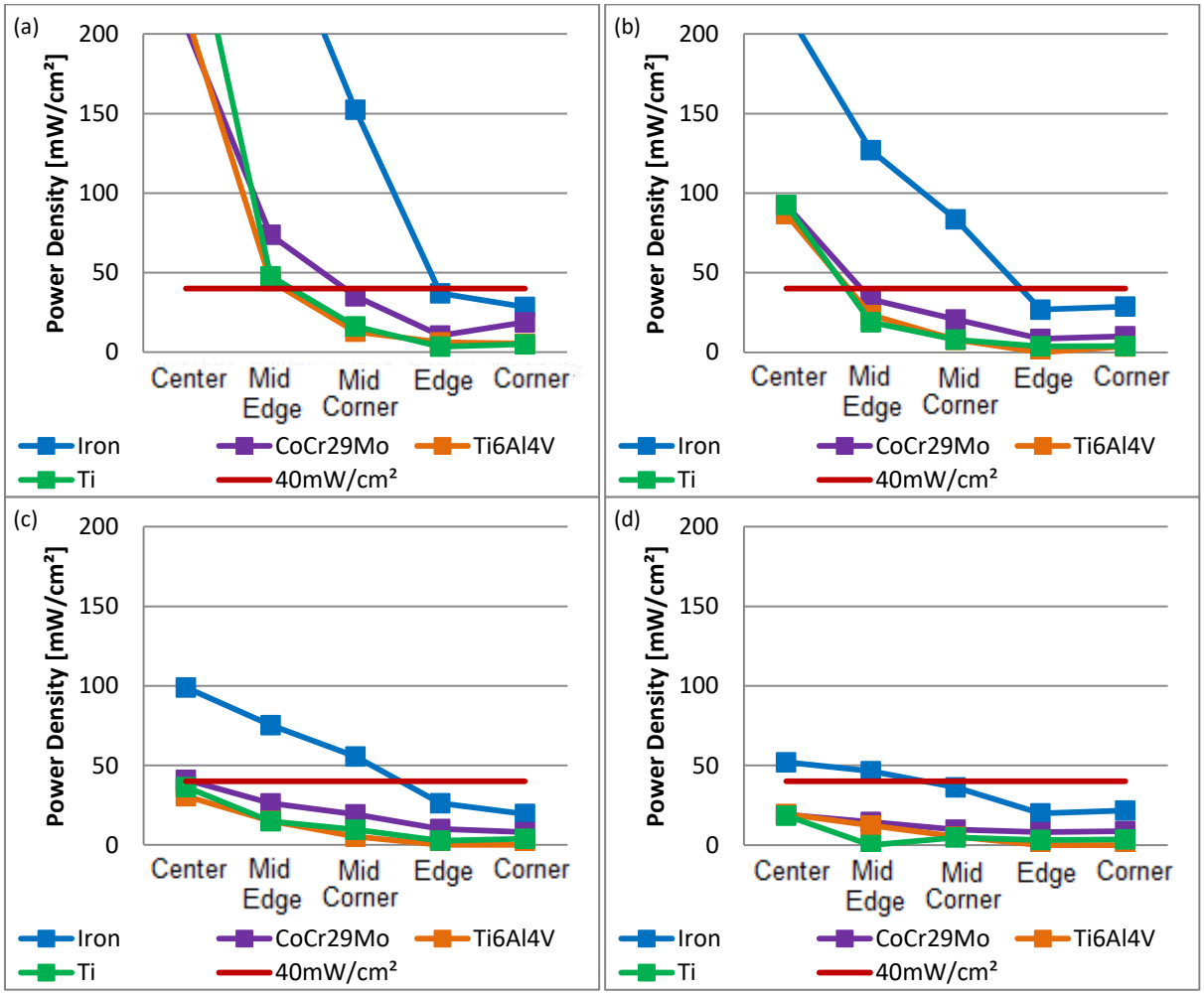

Figure 35: 2-dimensional line graph of the power density plotted over the different positions for all materials at a distance of (a) 20mm (b) 40mm (c) 60mm (d) 80mm. The red line represents the critical power density of 40mW/cm²

Figure 35a) represents an enlargement of the samples at a distance of 20mm from the seat surface. The different positions were plotted on the x-axis and the y-axis shows the power density. Comparing the different samples, it can be seen that the samples of Ti and Ti6Al4V have

similar curves. This can be explained by the fact that both samples have similar material properties and surface areas. Because of its material properties and shape iron heats the most and thus has the highest power density in each of the five positions. In contrast, the other samples have significantly lower levels. Comparing the power densities in the Center, iron has a significantly higher power density of 435,98mW/cm^2 as CoCr29MO, resulting to 204,84mW/cm^2. This corresponds to 46,98% of the iron power density measured in the Center. In further comparison with Ti and Ti6Al4V, the power density corresponds to 66,78% and 48,98% of the iron value in the center. In comparison, the power density of CoCr29Mo drops to 65,80% in the Corner, 28,38% in the Edge, 23,07% in MidCorner and to 26,18% in MidEdge of the respective iron values. In the case of Ti and Ti6Al4V the power density drops between 17,43% and 19% in the Corner, 9,55% and 16,80% in the Edge, 10,67% and 8,47% in MidCorner and 16,92% and 15,90% in MidEdge, compared to the respective iron value.

As shown in Figure 35b) iron has the highest power density even in the range of 40mm between seat surface and sample. As can be seen, the power density of TiAl4V, Ti and CoCr29Mo are already below the critical 40mW/cm^2 mark at a distance of 20mm and the MidCorner, Edge and Corner position. The only exception concerns the iron sample. In the Edge and Corner position, the power density is below the critical mark. In the Center position, the power density of iron results in 215,33mW/cm^2. Compared to the other samples, CoCr29Mo and Ti have almost the same power densities of 92,61mW/cm^2 and 92,66mW/cm^2, which corresponds to 43,01% and 43,03% of the measured iron value. TiAl4V has a slightly lower power density value of 86,87mW/cm^2, which corresponds to 40,34% of the iron power density. In comparison to iron, the power density of CoCr29Mo drops to 24,75% in MidEdge, 24,75% in MidCorner, 31,52% in the Edge and 35,25% in the Corner. Unlike the center, there are differences between CoCr29Mo and Ti between the remaining positions. As can be seen, the power density of Ti drops faster to 14,85% in MidEdge, 9,57% in MidCorner, 14,24% in the Edge and 13,48% in the Corner. For Ti6Al4V, the power density drops to 18,44% in MidEdge, 9,35% in MidCorner and 12,71% in the Corner.

As can be seen in Figure 35c) all samples, with exception of the iron sample and the tight value of CoCr29Mo in the Center, are below the critical 40mW/cm^2 mark at a distance of 60mm. In the Center position, the power density of iron results in 98,96mW/cm^2. Compared to the other samples, CoCr29Mo has a power density of 40,93mW/cm^2, which is just above the critical value, and this corresponds to 41,37% of the iron value. For Ti ad Ti6Al4V the power densities drops to 36,38mW/cm^2 and 30,65mW/cm^2, which corresponds to 36,76% and 30,97% of the iron power density. Comparing the different positions, the power density of CoCr29Mo drops to 34,73% in MidEdge, 34,64% in MidCorner, 38,35% in the Edge and 41,05% in the Corner. The power density of Ti shows significantly lower values, resulting in 19,83% in MidEdge, 17,24% in

MidCorner, 10,52% in the Edge and 19,96% in the Corner. For Ti6A4V the power density drops to 20,11% in MidEdge and 9,28% in MidCorner. Since the power density is already below the critical mark, no further measurements were carried out for the positions Edge and Corner.

As shown in Figure 35d) the power density of iron at a distance of 80mm is still 52,02mW/cm^2 in the Center and 46,43mW/cm^2 in the MidEdge. In the remaining position, these power densities are below the critical mark. Compared to the center position of the other samples, CoCr29Mo has a power density of 19,13mW/cm^2, which corresponds to 36,78% of the iron value. For Ti ad Ti6Al4V the power densities drops to 18,44mW/cm^2 and 19,53mW/cm^2, which corresponds to 35,44% and 37,54% of the iron power density. Comparing the different positions, the power density of CoCr29Mo drops to 31,35% in MidEdge, 26,74% in MidCorner, 40,62% in the Edge and 39,95% in the Corner. The power density of Ti shows again lower values, resulting in 13,21% in MidCorner, 16,05% in the Edge and 16,50% in the Corner. For technical reasons, no measurement could be performed for the MidEdge position. For Ti6A4V the power density drops to 26,50% in MidEdge and 14,43% in MidCorner. Since the power density is already below the critical mark, no further measurements were carried out for the positions Edge and Corner again.

In summary, it can be observed, that the iron sample heats up the most and thus results in the highest power density of the used samples. Even at a distance of 80mm between the seat surface and the sample, power densities in the Center still exceed the critical 40mW/cm^2. Although a rapid drop can be seen after 80mm, the values are only 11,93% of the original 20mm power density. This drop can also be seen in the other samples. CoCr29Mo and Ti6Al4V show similar values of 9,33% and 9,14%. Ti has a much smaller value of 6,33% of the original 20mm power density. In contrast, it can be concluded that the power density of CoCr29Mo did not decrease as quickly as Ti or Ti6Al4V. This can be explained by the different material properties and characteristics, described in section 3.1.3.

Furthermore, the strongest power density can be observed in the Center of each sample. This can be explained by the shape of the coil. In the Center, the sample heats up the most, because of the induced eddy current, and this results in higher power density. From the shape of the coil, it can be concluded that the magnetic field in the Corner is not as strong as in the Edge, and thus, smaller eddy currents heat the material. The same principle applies to the MidEdge and MidCorner and ensures that the power density in the MidEdge position is higher than in the MidCorner position.

Table 7: Summary of all distances where the power density is below the critical 40mW/cm^2 mark

	Iron	CoCr29Mo	Ti	Ti6Al4V
Center	100mm	80mm	60mm	60mm
MidEdge	100mm	40mm	40mm	40mm
MidCorner	80mm	0mm	0mm	0mm
Edge	0mm	0mm	0mm	0mm
Corner	0mm	0mm	0mm	0mm

An overview of all distances where the power density is below the critical 40mW/cm^2 mark is listed in Table 7. As can be seen, Ti and Ti6Al4V have the same measured distances where the power density is below the critical 40mW/cm^2 mark. CoCr29Mo differs from these samples only in the position of the Center. In this table, it can be seen once again that iron expands the highest power density and therefore the sample has to be the furthest away from the coil to fall below the critical power density.

CHAPTER 4 SENSIBILITY MEASUREMENTS

This chapter presents the metal detection of all materials in their respective positions and distances, with a particular focus on the regions of interest defined in Chapter 3. These regions are defined as the areas where the power density is above the critical 40mW/cm^2 mark and damage to the surrounding tissue could occur.

This chapter is divided into four sections. The first section describes the materials. These are the same four materials as used in the temperature measurements. The second section presents the methods of measurements. The calibration of the system is particularly important, otherwise the magnetic remanence could influence the result. Then the measurement process is shown. Again, the same standard settings were used as in the temperature measurements. Various conditions were tested and finally, a suitable threshold for the detection range was defined. After that, the actual detection is explained. The next section presents the results of all materials are presented and the last section of this chapter considers the description and discussion of these results.

4.1 MATERIALS

In order to not affect the tests and to make comparisons between the temperature and sensitivity measurements, all measurements took place under the same conditions as the temperature measurements, including the materials, positions, distances and the used device. A more detailed description can be found in section 3.1.

4.2 METHODS

4.2.1 CALIBRATION

Before the measurements start, the system has to be calibrated to ensure that the system is more robust against magnetic remanence.

The calibration process is performed continuously, starting with the empty chair and taking place in eleven steps starting from 0% and moving the coil towards 100%, as can be seen in section 2.2.3. After the initial calibration, the coil moves every 10% to a new position and recalibrates.

After a successful calibration, the screening of metals on the patient starts. The patient sits on the chair and every 10% steps the coil movement stops and a measurement is carried out. Thereafter, this measured value is compared with the value of the calibration.

4.2.2 PROCEDURE

The sensitivity test was used to determine the detection range. This ensured reliable detection and evaluation of the results for the various scenarios. Therefore different conditions were created and tested.

In the first condition, the measurement was made after the system was on standby for at least 12 hours to ensure that the magnetic remanence is negligible. Therefore, the device was connected to the mains overnight. Figure 36 shows the schematic sequence of this condition. As can be seen each position was tested after the calibration and then a test was performed without a sample. Subsequently, a plexiglas sheet was added and after 30 seconds the process was repeated until all distances were tested.

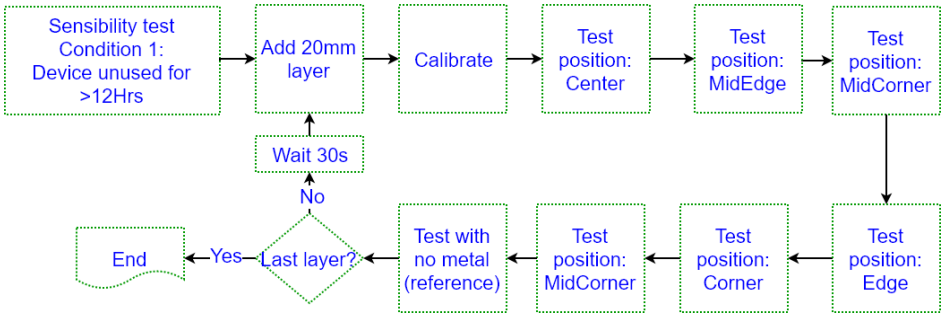

Figure 36: Schematic sequence of the first condition (Vargas Luna, 2016)

The next condition was measured 5 minutes after the last stimulation pulse of a treatment. This condition evaluated the robustness of the system to the magnetic remanence. In addition, this condition also investigated how the system affected a higher operating temperature because stimulation warmed up the environment inside the chair. Figure 37 shows the schematic sequence of the second condition. As with the previous condition, tests were performed for all positions and distances. Before this procedure could start, a complete treatment was performed and the first calibration took place five minutes after the end of the treatment.

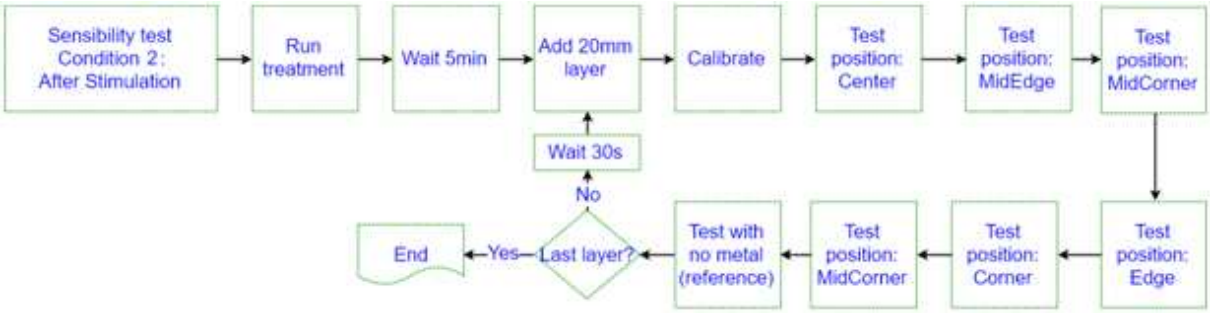

Figure 37: Schematic sequence of the second condition (Vargas Luna, 2016)

Sensibility measurement used the same PelviPower Magnetic Field Trainer settings as explained in section 3.2.1, which corresponded to an intensity of 4, a frequency of 50Hz and a stimulation time of 12 seconds.

4.2.3 Signal Processing

For the investigation of the detection threshold, a reference value with the sensibility measurements was searched. These values showed the differences between the recorded and stored calibration value and the subsequent measurement. It should be noted that the measurements were made at the same coil position so that the values can be properly compared. For the sensibility measurements, a calibration value was carried out for each sample and then all positions were tested in the coil position of 100%. For all tests, the metal monitor was completely assembled and installed inside the chair, the chair was completely closed and no metal sample was in the immediate vicinity of the coil.

The metal detection takes place after successful calibration. The respective sample was placed at the different positions and distances between sample and seat surface. If a metal sample is detected, the measured voltage changes and becomes smaller due to the metal. This result is converted to a digital value and compared with the value of the calibration. If this comparison is in the threshold of seven, which means a voltage value of ~21,875mV, no metal sample was detected. If the measured voltage value has a smaller value and is therefore not in the threshold, it could be assumed that a metal sample had been detected. The measurement stopped and a warning was displayed on the control screen. For the repetition of the measurement, the coil was brought back to the initial position and the measurement started again at a coil position of 0%.

After successful completion of the detection, the actual treatment could start. In order to determine the temperature effects, and thus the power density, of the individual sample, the temperature changes of the various samples were measured. The sequence of the measurements was repeated with each sample, each position, and distance. To ensure a consistent

measurement, all samples must have the approximate room temperature before the measurement started.

4.3 RESULTS

For the detection threshold, a total of 126 values were acquired under the different conditions. The calculated mean of the sample was μ=2,1 with a standard deviation of σ=2,3. The corresponded measured values can be seen in Figure 38.

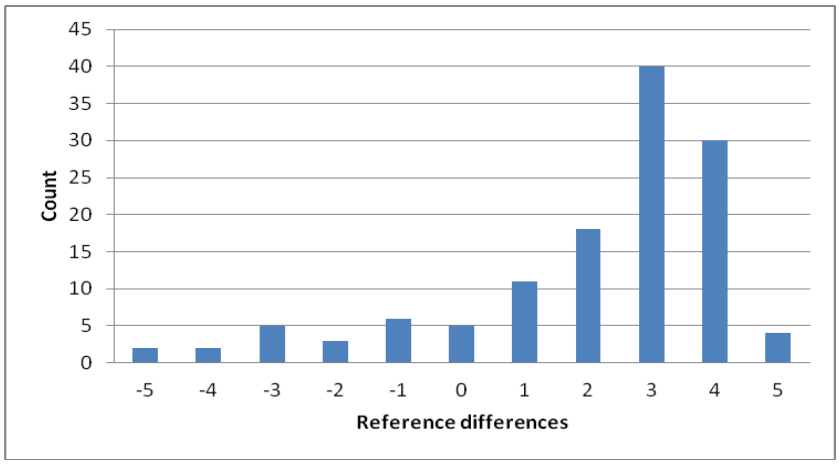

Figure 38: Threshold: Summary of the bar chart (Vargas Luna, 2016)

Table 8: Threshold: Summary of the bar chart (Vargas Luna, 2016)

Reference differences	Count	Reference differences	Count
-5	2	**1**	11
-4	2	**2**	18
-3	5	**3**	40
-2	3	**4**	30
-1	6	**5**	4
0	5		

As can be seen in the histogram and in Table 8, 70% of the measured values were in the range between 2 and 4. It was important to notice that most of the samples with values smaller than -1 were acquired during the first measurements of the second condition, and were a consequence of the magnetic remanence, that was changed relatively fast at the beginning.

In summary, the system was robust to these changes and the metal samples were detected within the required range. The detection threshold should be as small as possible so that metal parts located at a larger distance from the coil could still be detected. At the same time, this threshold should be large enough to minimize false positive values. The test measurements showed that the expected maximum difference was five, so a threshold of six would be sufficient. As the system may change due to aging and product variability, a threshold of seven had been chosen to counteract such changes.

For the sensibility measurements the maximum detectable distances from the samples are specified in Table 9. It shows the distances that can be detected from the seat surface up to the maximum detectable distance which were systematically detected under all repetitions and conditions.

Table 9: Maximum detectable distances

	Iron	**CoCr29Mo**	**Ti**	**Ti6Al4V**
Center	120mm	100mm	100mm	100mm
MidEdge	120mm	60mm	60mm	100mm
MidCorner	80mm	60mm	40mm	40mm
Edge	60mm	0mm	0mm	0mm
Corner	20mm	0mm	0mm	0mm

Figure 39 to Figure 42 show the maximum detectable distances over the positions and are divided into two parts. Figure a) consists of two different parts. The graph highlights the maximum detectable distances over the positions. The different measurement positions are indicated on the x-axis and y-axis. The corresponding maximum detectable distance is plotted on the z-axis. The second part of the figure is the 3-dimensional picture of the used coil, displayed on the x-axis and y-axis. Figure b) shows a 2-dimensional line graph of the same measurement. The different positions are plotted on the x-axis and the measured detectable distances can be seen on the y-axis.

As can be seen in Figure 39, a reliable detection in the Center and MidEdge can be ensured up to a distance of 120mm between the seat surface and the sample for iron. The maximum detection range was expected in the Center of the coil. The figure shows that the detection range is the same in these two positions. This can be explained by the fact that plexiglas sheets with a width

of 20mm were used in the measurements. The maximum detectable distance drops to 80mm in the MidCorner position. In the position Edge and Corner, the maximum detectable distance drops to a distance of 60mm and 20mm.

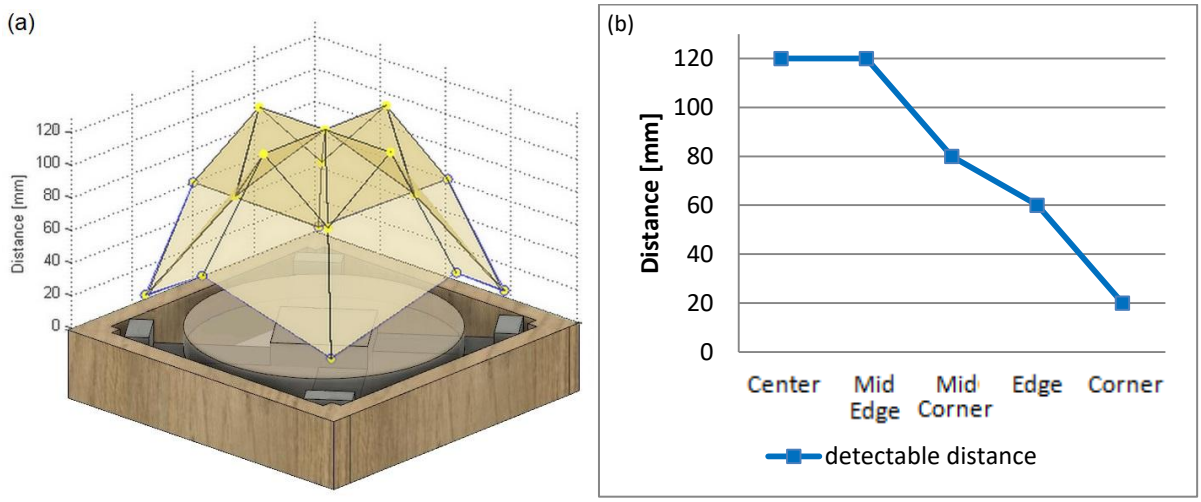

Figure 39: Iron: Maximum detectable distances plotted over the five positions represent in an (a) 3-dimensional diagram and a (b) 2-dimensional line graph

As shown in Figure 40, and expected with the theory, a safe detection for CoCr29Mo can be only ensured in the Center position in the range of 100mm between the seat surface and the maximum detectable distance. The maximum detectable distance drops to 60mm in the MidEdge and MidCorner position and is no longer possible in the Edge and Corner position.

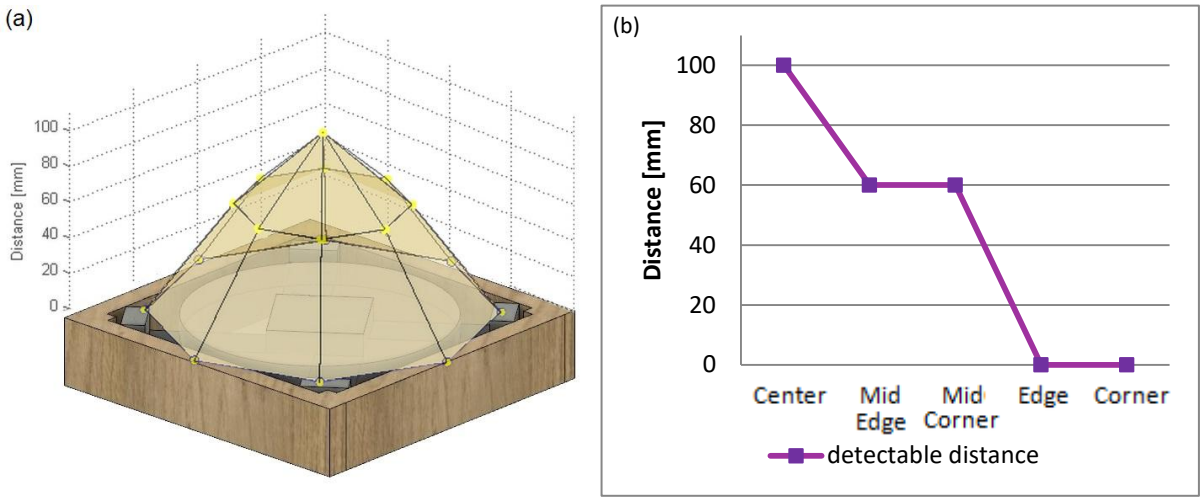

Figure 40: CoCr29Mo: Maximum detectable distances plotted over the five positions represent in an (a) 3-dimensional diagram and a (b) 2-dimensional line graph

Figure 41 presents the maximum detectable distance of Ti over the positions. Like CoCr29Mo a safe detection can be only ensured in the Center position in a range of 100mm. The maximum detectable distance drops to 60mm in the MidEdge and 40mm in the MidCorner position. In the Edge and Corner position the safety detection is no longer possible.

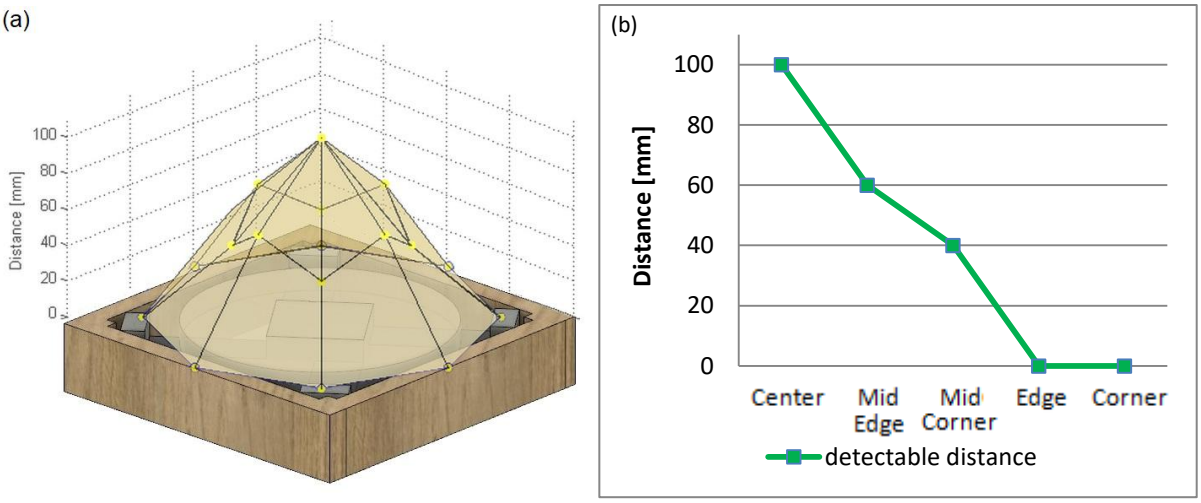

Figure 41: Ti: Maximum detectable distances plotted over the five positions represent in an (a) 3-dimensional diagram and a (b) 2-dimensional line graph

Figure 42 shows safety detection up to a distance of 100mm in the Center and MidEdge for Ti6Al4V between the seat surface and the maximum detectable distance. In MidCorner the this distance falls to 40mm and in the Edge and Corner position, the detection is no longer possible.

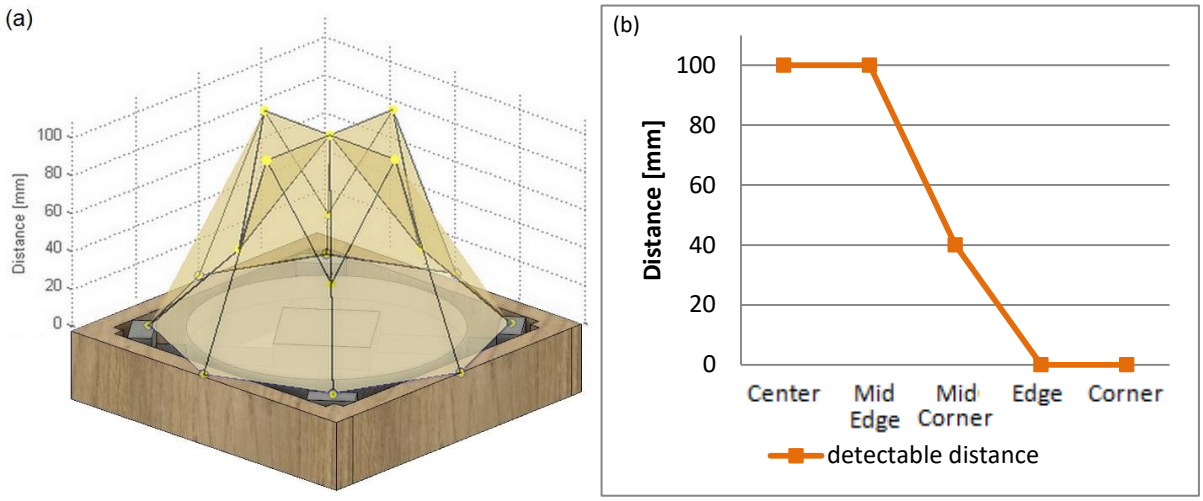

Figure 42: Ti6Al4V: Maximum detectable distances plotted over the five positions represent in an (a) 3-dimensional diagram and a (b) 2-dimensional line graph

4.4 Discussion

The maximum detectable distances of all samples are shown in Figure 43. The x-axis shows the positions and the y-axis shows the measured distance. Several measurements of the same sample, distance and position were performed, but in all test conditions, the same maximum detectable distance were reliable detected.

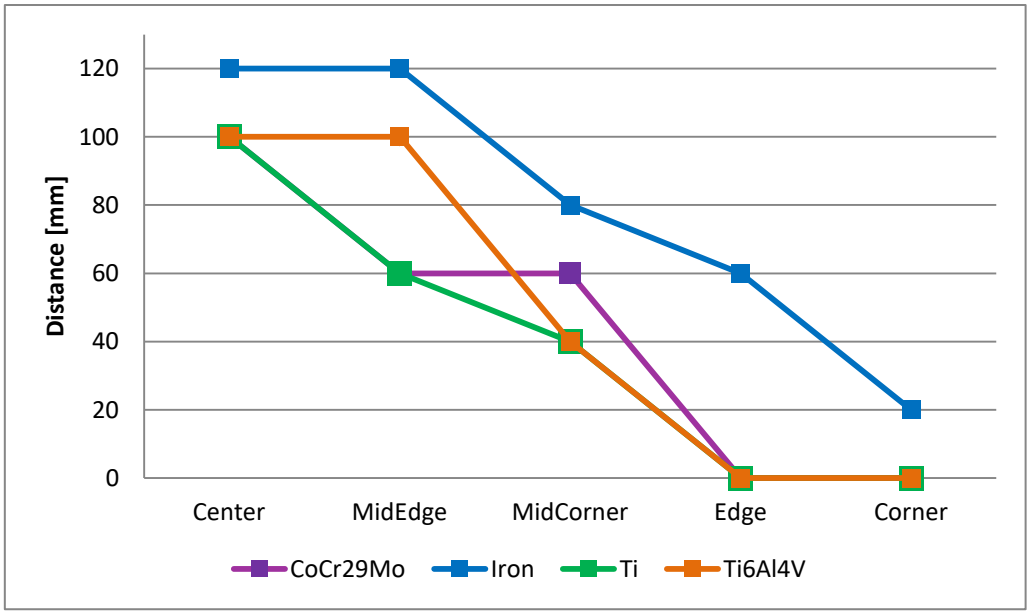

Figure 43: 2-dimensional line graph of the maximum detectable distances plotted over the five positions for all materials

Figure 43 shows the maximum detectable distances plotted over the positions for all samples. The iron sample, due to its properties and geometry, has the largest detection range, as can be seen in section 3.1.3. It can be seen, that the iron sample influences the detection threshold the most. Even at a distance of 120mm and the Center and MidEdge position a safe detection is ensured.

As already mentioned in section 3.1.2, it has to be expected that the highest detection is in the Center, affected due to the shape of the coil. The largest eddy currents make sure that also the strongest secondary magnetic fields arise in the Center and the possible detection range increase. Comparing MidEdge and MidCorner, it can be assumed that MidEdge can reliably detect a higher range between seat surface and sample. Because of the shape of the coil, the core corner forces the field closer to the coils surface and reduced the sensibility in MidCorner. The same applies to Edge and Corner position. The measurements have been carried out to a distance up to 100mm for the CoCr29Mo, Ti6Al4V and Ti sample. For iron the measurements have been carried out to a distance of 120mm.

Comparing the other samples and positions with iron, the maximum detectable distance in the Edge and Corner position drops to a distance of 60mm in the Edge and 20mm in the Corner, but is still the most detectable distance of all samples. In the Center and MidEdge the detectable distance can be ensured in a range of 120mm and drops to 80mm in MidCorner. Depending on the comparative sample and position, a higher distance between 20mm, comparing with CoCr29Mo in the MidCorner position, and 60mm, comparing with Ti or CorCr29Mo in the MidEdge position, can be detected with iron. The difference in the detectable range in the Center

also differs only 20mm between iron and all other samples. As already mentioned, it can be seen again that the maximum detectable distance is the highest in this position, regardless of the used sample.

Compared to iron pure Ti is difficult to detect. Based on the properties and shape of the sample, a safety detection can be only ensured up to a distance of 100mm in the Center. In MidEdge the maximum detectable range drops to 60mm and in MidCorner it falls quickly to 40mm. As already mentioned above, a sample detection in the Edge and Corner position cannot be ensured. Reasons for this are on the one hand the small changes due to the material and on the other hand the shape of the coil. Comparing Ti and Ti6Al4V, it can be seen that these samples differ only in MidEdge position. For Ti the detection range drops to 60mm, while Ti6Al4V can be detected up to 100mm. In the Center a safety detection up to 100mm can be ensured. For both materials no sample could be detected in the Edge and Corner positions. These results can be attributed to the material properties, characteristics, and shape of the coil. With the Ti and CoCr29Mo sample, the maximum detectable distance only differs in the MidCorner position. In this position the maximum detectable distance for Ti drops to 40mm. CoCr29Mo has a higher detection range of up to 60mm. Both samples, CoCr29Mo and Ti, can detect the corresponding material in the Center position up to a distance of 100mm. Similar to Ti, the CoCr29Mo sample could not be detected in the Edge and Corner position. These results can be attributed again to the material properties, characteristics, and shape of the coil. Comparing Ti6Al4V and CoCr29Mo, a safety detection can be ensured up to 100mm in the Center for both samples. For Ti6Al4V the detection range is still 100mm in MidEdge and drops to 40mm in MidCorner. CoCr29Mo has a smaller detection range in MidEdge up to 60mm and a higher detection range in the MidCorner up to 60mm. For both materials, no samples can be detected in the Edge and Corner position. These results can be attributed to the material properties, characteristics, and shape of the coil.

CHAPTER

5 DISCUSSION

In the first section of this chapter, the results of the temperature measurements, see chapter 3, and the sensibility measurements, see chapter 4, are compared and evaluated. The second section discusses the material influences, based on the theory, are considered to the results and at the end of this chapter the additional measurements with other materials, like an intrauterine device and a piercing, are explained.

The detection and the heating of the samples depend on the induced eddy currents. The higher these eddy currents are in the samples, the higher is the heat transfer into the material, which results in a higher power density. Simultaneously, the higher eddy currents also induce a stronger secondary magnetic field, which further modifies the self-inductance and, therefore, increases the detection range. Since the heating and the detection are directly proportional to the magnitude of the eddy currents, there is a strong correlation between them. This means that the higher the power density is the higher is the detection range.

Based on the temperature measurements, the corresponding power density was calculated. According to Wolf (Wolf, 2008), the maximum power density in a metal should not exceed $40mW/cm^2$. A power density higher than this value could damage the surrounding tissue by the resulting heating. To prevent this, a reliable detection in dangerous areas must be ensured. This chapter summarizes and compares these two main measurements. The maximum detectable distance and the distance where the power density is below the critical $40mW/cm^2$ mark can be seen in Table 10. In order to have an additional safety margin, there is another 20mm distance between the last distance where the power density is below the critical $40mW/cm^2$ mark and the maximum detectable distance.

As can be observed in Table 10, these additional criteria are fulfilled for all samples. For CoCr29MO, Ti and Ti6Al4V, it can be seen that no secure detection is possible in the position of Edge and Corner. But the power density of these samples does not reach the critical value at any distance, therefore it does not endanger the patient.

Table 10: Comparison of the maximum detectable distances and the distances where the power density is below the critical 40mW/cm² mark for all positions and materials

		Center	Mid Edge	Mid Corner	Edge	Corner
Iron	**Detectable distance**	120mm	120mm	80mm	60mm	20mm
	Distance < 40mW/cm²	100mm	100mm	80mm	0mm	0mm
CoCr29Mo	**Detectable distance**	100mm	60mm	60mm	0mm	0mm
	Distance < 40mW/cm²	80mm	40mm	0mm	0mm	0mm
Ti	**Detectable distance**	100mm	60mm	40mm	0mm	0mm
	Distance < 40mW/cm²	60mm	40mm	0mm	0mm	0mm
Ti6Al4V	**Detectable distance**	100mm	100mm	40mm	0mm	0mm
	Distance < 40mW/cm²	60mm	40mm	0mm	0mm	0mm

Figure 44 to Figure 47 show the maximum detectable distance (dashed line) and the distance where the power density is below the critical 40mW/cm² mark (solid line) plotted over the different positions. Figure a) consists of two different parts. The different measurement positions are indicated on the x-axis and y-axis. The maximum detectable distance and the distance where the power density is below the critical mark are plotted on the z-axis. The second part of the figure is the 3-dimensional picture of the used coil, displayed on the x-axis and y-axis. Figure b) shows a 2-dimensional line graph, where the different positions are plotted on the x-axis and the maximum detectable distances can be seen on the y-axis.

As mentioned in the previous section and shown in Figure 44, the iron sample in the Center and MidEdge will not reach a power density below the critical mark. For this sample, the temperature measurements in a range of 80mm and the sensibility measurements in the range of 120mm were performed. Based on the results of the trend line (Figure 27) it can be assumed

that no dangerous power density occurs at a distance of 100mm and therefore an additional 20mm safety margin is ensured. In MidCorner, the power density drops below the critical mark at a distance of 80mm. A detection of the sample is possible in this position in the range of 80mm. Therefore, the additional 20mm safety margin is missing in this position. Since the power density is already below the critical mark in this area, reliable detection can be ensured. In the Edge and Corner position, this safety margin increases to 60mm and 20mm difference between the power density and the maximum detectable distance, but in these two positions, heating for the surrounding tissue is no longer dangerous.

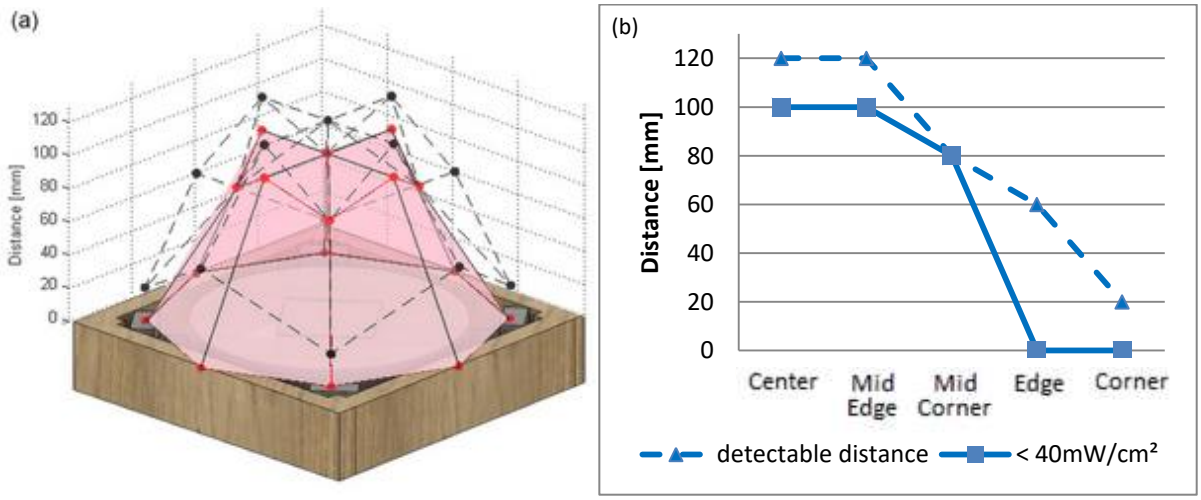

Figure 44: Iron: maximum detectable distances (dashed line) and the distances where the power density is below the critical 40mW/cm² mark (solid line) plotted over the different positions represent in an (a) 3-dimensional diagram and a (b) 2-dimensional line graph

As can be seen in Figure 45, all dangerous power densities of CoCr29Mo were detected safely. Even in the Center, where the critical power density is below the critical mark with a distance of 80mm, reliable detection could be ensured up to 100mm. This corresponds to an additional 20mm safety margin, even if the resulting heating no longer harmed the surrounding tissue. In MidEdge both the dangerous distance of the power density decreases to 40mm and the maximum detectable range to 60mm. This value was also determined in the MidCorner, but no critical power density occurred in this position. In the Edge and Corner position the detection is no longer possible, but there is no dangerous heating anymore.

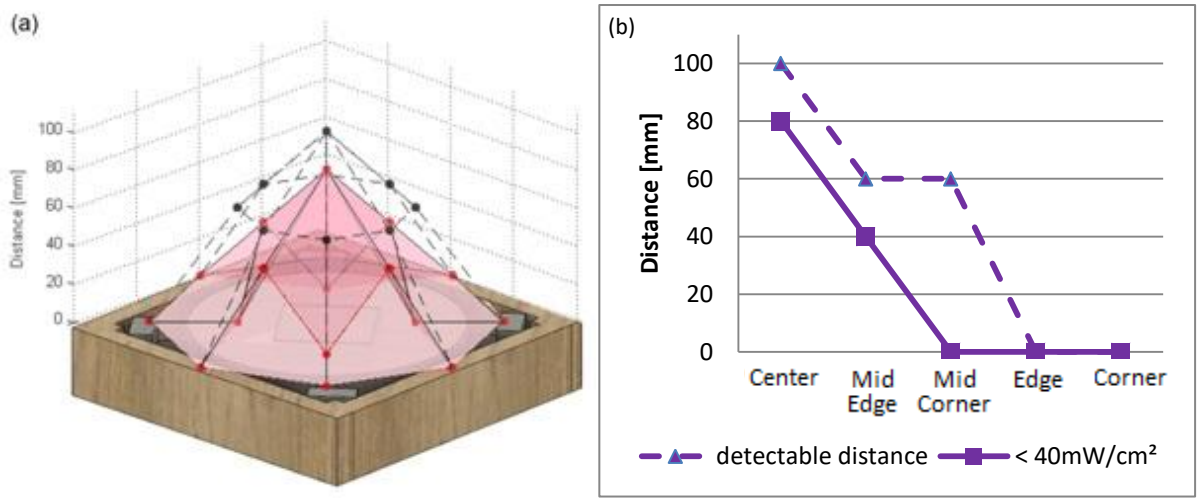

Figure 45: CoCr29Mo: maximum detectable distances (dashed line) and the distances where the power density is below the critical 40mW/cm² mark (solid line) plotted over the different positions represent in an (a) 3-dimensional diagram and a (b) 2-dimensional line graph

According to Figure 46, a clear detection of all positions can be ensured for Ti. In the Center, samples in a range of 100mm can be reliably detected. The critical power density is below the critical mark with a distance of 60mm and this corresponds to an additional 40mm safety margin. In MidEdge, the maximum detectable range drops to 60mm and the distance where the power density is below the critical mark decrease to 40mm. In the MidCorner, a sample is still detected up to a distances of 40mm. No detections are possible in the Edge and Corner position.

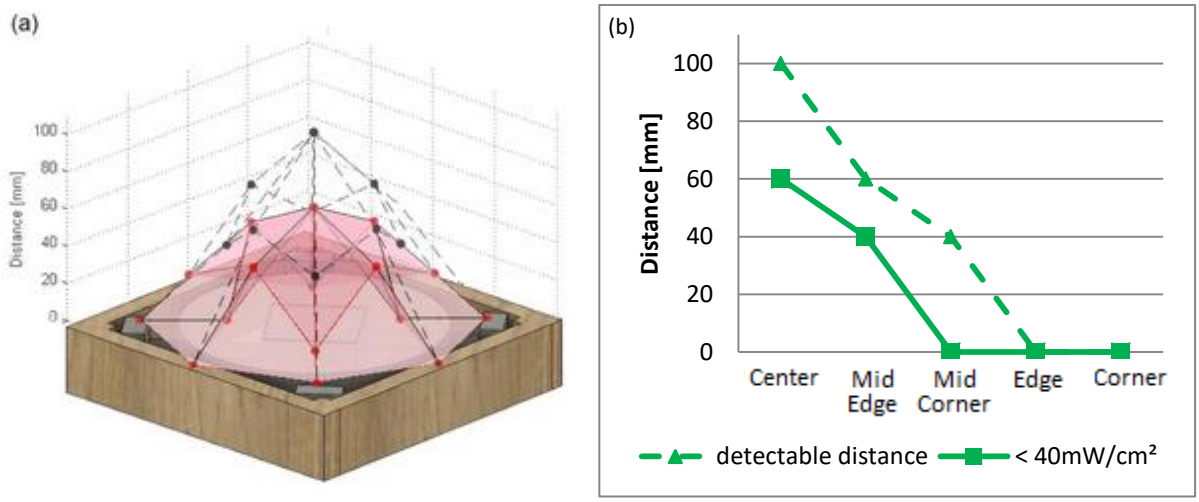

Figure 46: Ti: maximum detectable distances (dashed line) and the distances where the power density is below the critical 40mW/cm² mark (solid line) plotted over the different positions represent in an (a) 3-dimensional diagram and a (b) 2-dimensional line graph

Finally, Figure 47 shows a clear detection of all positions for Ti6Al4V. In the Center and MidEdge position, samples in a range of 100mm can be reliably detected. The corresponding distance for a critical power density below the critical mark is 60mm in the Center and 40mm in the MidEdge and therefore the safety margin is ensured. In the MidCorner, the detection distance drops

quickly to 40mm and also the distance for the critical power density drops, so there is no dangerous heating in this position. Consistent with CoCr29Mo and Ti, no detection is possible in the Edge and Corner position again.

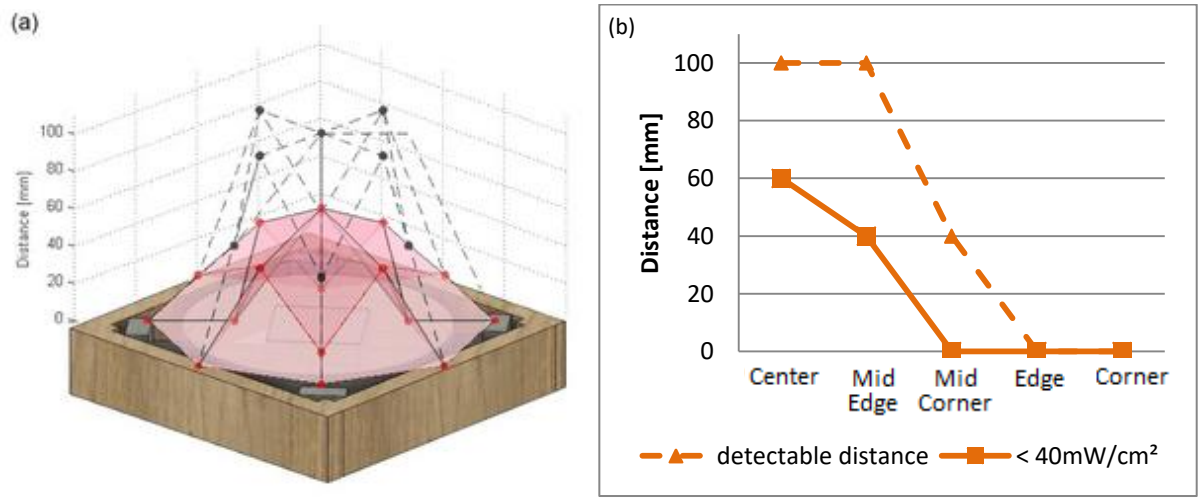

Figure 47: Ti6Al4V: maximum detectable distances (dashed line) and the distances where the power density is below the critical 40mW/cm² mark (solid line) plotted over the different positions represent in an (a) 3-dimensional diagram and a (b) 2-dimensional line graph

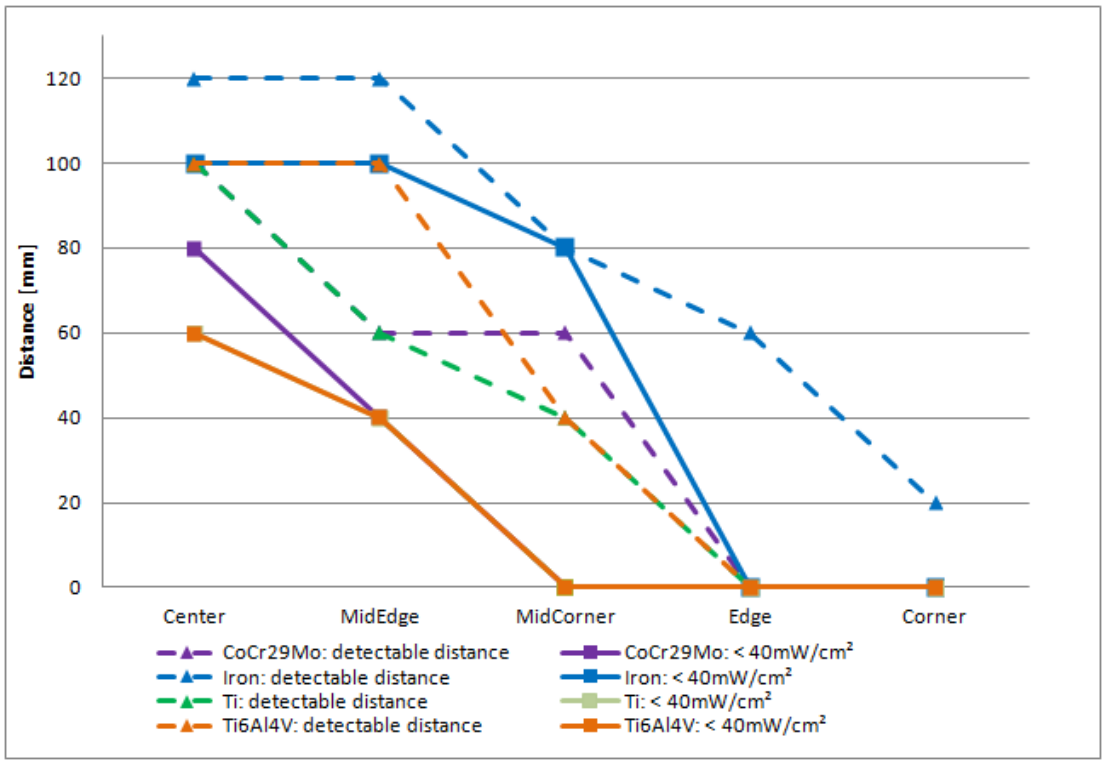

Figure 48: 2-dimensional line graph of the maximum detectable distances (dashed line) and the distances where the power density is below the critical 40mW/cm² mark (solid line) plotted over the different positions for all materials

Figure 48 summarizes all described scenarios in one line graph. The x-axis shows the possible positions and the y-axis the distances. The y-axis shows the maximum detectable distance (solid

line) and the distance where the power density drops below the critical 40mW/cm² mark (dotted line), for the particular sample.

Comparing the distances, it can be seen that the deviations between the maximum detectable distance and the distance where the power density is below the critical power density mark are between 20mm and 60mm for all samples. At the Center Ti6Al4V and Ti have the highest safety margin with a distance of 40mm. For CoCr29Mo and iron this value drops to a safety margin of 20mm. In the MidEdge position, Ti6Al4V has the highest factor of 60mm, while all other samples have a safety margin of 20mm. The highest safety margin in MidCorner has Ti with a distance of 40mm. For Ti6Al4V and CoCr29Mo this value drops to 20mm difference and iron has no safety margin in this position. For the Edge position, iron has a safety margin of 60mm, for all other samples a safety detection is no longer possible. In the Corner the distance drops to 20mm for iron. For the other samples, no detection can be performed in this position.

In summary, a comparison of the different measurements shows that the samples CoCr29Mo, Ti and Ti6Al4V have similar results. The samples Ti and Ti6Al4V have the same distances, where the power density falls below the critical mark, in the respective positions. The CoCr29Mo sample has a difference in the Center position where the distance is 20mm higher. In contrast, due to the higher eddy currents, iron has higher heating and thus higher power density. The shape of the sample favors this even more. It can be seen, that due to these higher eddy currents, the secondary magnetic field also becomes stronger and thus the possible detection is increased.

Slight variations in the measured values may be influenced by factors such as an open window on a windy day or room temperature during the measurement.

5.1 Influence of metals

There are several factors that influence the heating of the metal, and thus the power density. The inductive heating depends on the penetration depth, the eddy currents, and the material parameters but also on the coil itself. Since all the measurements were made with the same coil, all samples were also exposed to the same influences. Therefore it is not considered further for differentiation. As already mentioned, the heat transfer increases with higher eddy currents and leads to a higher power density. In the following section, the different materials are compared and the influence on the heating is explained.

In comparison to the other samples, the measurements of the iron sample are not so important because this sample, in this size and shape, is not used as an implant and therefore does not occur in the human body. These measurements will be included as representative data for other non-biocompatible materials and therefore they were taken as a reference value.

The material properties and characteristics of all use samples are summarized in Table 3. As can be seen, the iron sample is the heaviest with the largest surface area compared to the other samples. This and the other material properties ensure the induction of the highest eddy current in the iron sample and because of that, the sample heats up the most. The iron sample also has the highest magnetic permeability and the electrical resistance in the lower ranges. This leads to a higher electrical conductivity. Since the penetration depth depends on the magnetic permeability and the electrical conductivity, these properties lead to the lowest penetration depth of all samples. This results in a higher impedance near the surface. Due to the higher impedance, the sample heats up faster and have a higher power density. Another factor for this high power density is the mass of the sample, which additionally promotes these high values. The specific heat also affects this result and has the smallest value for iron. Compared to the other variables, the specific heat does not have such a large effect on the power density and this ultimately leads to the highest values being measured in the iron sample.

As can be seen in Table 3, the magnetic permeability of Ti6Al4V and Ti hardly differs from each other with μ=1,00005H/m and μ=1,0000013H/m. Since no exact values for the electrical and magnetically properties were found for CoCr29Mo, the values for a CoCr Alloy were used with a magnetic permeability of μ<1.2. The electrical resistance gives much higher differences with ρ=178μΩcm for Ti6Al4V, ρ=90,8μΩcm for CoCr29Mo and ρ=55,4μΩcm for Ti. Based on the large electrical resistance, Ti6Al4V has the smallest electrical conductivity. The penetration depth depends on the magnetic permeability and the electrical conductivity and thereforeTi6Al4V has the furthest penetration depth. Due to the deeper penetration depth and dimension of the samples, the impedance near the surface is not as high, resulting in less inductive heating and a lower power density. Comparing Ti and CoCr29Mo with Ti6Al4V, each of the two samples have a lower electrical resistance and therefore a higher electrical conductivity. Therefore, the penetration depth is lower than the penetration depth of Ti6Al4V, resulting in a higher impedance near the surface and this leads to a higher power density.

To summarize all results, the material which is most influenced by the magnetic field heated up the most by the eddy current. Reasons for this heating are, on the one hand, the material properties, but also the surface area and shape of the sample on the other hand. The material properties also affect the possible detection range. The higher the resulting eddy currents in the material, the higher is also the detection range. Due to its properties, the iron sample has the highest detectable distance in all measured positions.

5.2 Additional Measurements

As already mentioned, the eddy currents depend on the material, the geometry and the orientation of the object. Therefore, it is not possible to test all the possible scenarios. Additional

measurements, described in Appendix A, were made to prove if the detection range changed with changed dimensions of the sample. This experiment was carried out with a sample of the material CoCr29Mo. The new, smaller test sample differed only in dimension from the original CoCr29Mo sample. The aim of this experiment was to determine if a sample made of the same material but with different dimensions and thus changed power density could also be safely detected.

The first tested sample was a small cobalt-chromium molybdenum sphere shaped hip head, designed by the company BBRAUN Austria with the part number NK544K for the BiCONTACT® Hip Endoprosthesis System. With the small CoCr29Mo sample (Figure 49), six repetitions were performed in the Center and at a distance of 40mm between seat surface and sample. The settings and execution of the measurements were the same as in the main measurements. The power density varies between 70,68mW/cm^2 and 82,91mW/cm^2 with a mean power density of 75,71mW/cm^2 and a standard deviation of 4,35mW/cm^2. In comparison, the large CoCr29Mo sample has a maximum recorded power density of 92,61mW/cm^2. The smaller power density of the small sample can be explained by the size of the sample with the same material. As with the first samples, the maximum detectable range of the small samples was determined. As already mentioned, the resulting power density and the maximum detectable range are related. The higher the power density, the larger the secondary magnetic field and the detection rate increase. In summary, it can be concluded, that the small sample can also be reliably detected. Although these measurements were not extensive, they provide a hint that this tendency might apply to different geometries and positions. In order to make reliable statements, it would be necessary to measure several positions and distances, as for the main materials.

In addition to this experiment, measurements were carried out with an intrauterine device and a piercing. Intrauterine device (Figure 52a) can be influenced by the magnetic field as well. Because of the small size and shape of the intrauterine device, the intrauterine device hardly heats up and therefore there is no danger to the surrounding tissue. A potential problem could be a possible dislocation due to vibration, as these devices are very light and thus can become an unwanted risk for the woman. Therefore, this device was tested for vibration movement. The tests show that the intrauterine device does not move above the seat of the PelviPower Magnetic Field Trainer during treatment. Recently, the effects of the magnetic field on a piercing (Figure 52b) were tested. The results were similar to the intrauterine device. No dangerous heating and no vibration movement could be detected. To confirm these results, another measurement was performed with a larger ring (Figure 52c). But even with this sample, no heating and vibration movements were measured. Further investigations should be validated for these objects in order to confirm the effects to the human body and to verify these results.

Chapter

6 Conclusion

The main measurements of this thesis are divided into two parts. The first part is about the temperature increase of the materials in different positions and distances between the sample and the seat surface during a patient's treatment. The temperature measurements are evaluated with the aim to identify the regions of interest, where the power density is above the critical 40mW/cm^2 mark. The second part deals with the detection of these materials, with a particular focus on the regions of interest, to ensure the safety of the patient.

Due to the induced eddy currents, metal pieces are potentially heated up in the immediate vicinity of a time-varying magnetic field. This heating depends on the material properties, geometry, cross-section and the position and distance between coil and sample. In the first part of this thesis, the temperature heating is measured during a training session. Subsequently, the power density is determined and evaluated from these temperature values. The second part deals with the detection of the metal pieces and the reliable detection of the samples in the regions of interest. Starting from the critical power density, the surrounding tissue could be damaged. Below this mark, the metal piece heats up, but the human body can compensate this heating with natural mechanisms. Identifying this dangerous region is difficult because of the magnetic remanence, which affects the measured voltage if no metal is present. Therefore, the system must be calibrated before starting the treatment.

It is not possible to test all the possible scenarios with different materials and geometries. Therefore additional measurements were made to prove if the detection range changed with changed dimensions of the sample. It can be concluded, that smaller samples can also be reliably detected and therfore they provide a hint that this tendency might apply to different geometries and positions. In addition to implants, other metal objects, such as an intrauterine device or a piercing can lead to unwanted heating. Therefore, further measurements are carried out with these objects. The measurements show that women who use an intrauterine device can use the device without concern about dangerous heating or vibration movement. The measurement with piercings provides results that are comparable to the previous measurements. No dangerous heating or movement can be detected. A more exhaustive study should be validated for both objects in order to confirm the effects to the human body and to verify these results.

In summary, this thesis describes the development and validation of a monitor for detecting metal implants with heating risk within the application field of a magnetic stimulator different heating of the materials and the resulting power density, depending on the position, material and distance between sample and coil. Confirm to the different properties and characteristics of the materials, the power density in some cases is above the critical 40mW/cm^2 mark. Based on Wolfs claim (Wolf, 2008) this power density could damage the surrounding tissue if the material will not be detected. The various tests confirm that all materials are reliably detected in their position and distance if the power density exceeds the critical mark. In addition, a 20mm safety margin between the distance where the power density is below the 40mW/cm^2 mark and the maximum detectable distance is still ensured in all samples, exception iron at one specific position. The detailed conclusions of this thesis can be found in section 3.4 for the power density, in section 4.4 for the maximum detectable distance and in section 5 as a summary of both measurements.

LIST OF ABBREVIATIONS

Characteristics of the magnetic field

B	Magnetic flux density [T]
H	Magnetic field strength [Am]
μ_0	Magnetic field constant [Vs/Am]
ρ	Electrical resistance [Ωm]
ρ_{20}	Electrical resistance related to 20°C
α_{20}	Temperature coefficient related to 20 °C (reference temperature)
ϑ	Temperature [° C]
U_{ind}	Induced electrical voltage [V]
$d\Phi$	Magnetic flux [Wb]
dt	Time [s]
δ	Depth of penetration [m]
σ	Electrical conductivity [S/m]
μ	Magnetic permeability [Vs/Am]
ω	Angular frequency [1/s]
c_p	Specific heat [kJ/kgK]
m	Mass [kg]
ΔT	Change of temperature [°K]
T	Time [s]
P	Heat flux, power density [W/cm^2]
K	Electrical resistance [S/m]
B_r	Remanence induction [T]
J_r	Remanence polarization [mT]
M_r	Remanence magnetization [A/m]

Materials

Ti6Al4V	Titanium-aluminum alloy
Ti	Titanium
CoCr Alloy	Cobalt-chromium-Alloy
CoCr29Mo	Cobalt-chromium-molybdenum- Alloy

Positions

MidEdge	Between Center and Edge
MidCorner	Between Center and Corner
Edge	In the Center of two poles
Center	Center of the coil

Other abbreviations

FES	Functional Magnetic Stimulation
OECD	Organisation for Economic Co-operation and Development
MRI	Magnetic Resonance Imaging
UART	Universal asynchronous receiver/transmitter
ACK	Acknowledgement message
SOH	Start of Heading
EOF	End of Frame
ASCII	American Standard Code for Information Interchange
T_M	Measured temperature value
T_R	Real temperature
ADC	Analog to Digital Converter
OPA	Operational amplifier
RPMS	Repetitive peripheral muscle stimulation

LIST OF FIGURES

LIST OF TABLES

BIBLIOGRAPHY

5832-12, I. (2007). *Implants for surgery -metallic materials- Part 12: Wrought cobalt- chromium-molybdenum alloy.* Geneva.

5832-2, I. (2007). *Implants for surgery - metallic materials - Part 2: Unalloyed titanium.* Geneva.

Aesculap. (2017). *Bicontact® Hüftendoprothesensystem*. Retrieved 10 19, 2017, from https://www.bbraun.de/de/products/b/bicontact-hueftendoprothesensystem.html

Alfred E. Bent, G. W. (2008). *Ostergard's Urogynecology and Pelvic Floor Dysfunction.* Philadelphia: Lippincott Williams & Wikkins.

Bär, C. (2008). *Dauerhafter Körperschmuck - Informationen und Empfehlungen zum Schutz vor Allergien und Infektionen.* Helmholtz Zentrum München.

Bernstein, H. (2012). *Elektrotechnik / Elektronik für Maschinenbauer.* München: Springer Vieweg.

Breuer. (1989). Taschenatlas Physik für Mediziner. In Breuer, *Taschenatlas Physik für Mediziner.* Berlin Heidelberg: Springer Verlag Berlin Heidelberg .

Brooks, D. (2009). *Skin Effect* . UP Media.

Bürscher, B. (2016, März 4). *Gesund.at*. Retrieved Oktober 5, 2017, from http://www.gesund.at/a/spirale

Cadena, R. (2010). Automated Lighting: The Art and Science of Moving Light in Theatre, Live Performance, and Entertainment, Second Edition. In R. Cadena, *Automated Lighting* (p. 79). UK: Taylor & Francis Ltd.

Christopher J. Yeung, R. C. (2002). RF Safety of Wires in Interventional MRI:. *Magnetic Resonance in Medicine 47* , pp. 187-193.

Corey B. Simon, J. L. (2016, 12 1). Age Group Comparisons of TENS Response among Individuals with Chronic Axial Low Back Pain. *HHS Public Access J Pain* , pp. 1268–1279.

Czichos, H. (1991). *HÜTTE Die Grundlagen der Ingenieurwissenschaften 29.* Berlin Heidelberg: Springer Verlag.

D.D. Chandi, P. G. (2003, 11 4). Functional extracorporeal magnetic stimulation as a treatment for female urinary incontinence: 'the chair'. *BJU INTERNATIONAL 93* , pp. 539-542.

Dobsák P, N. M. (2006, January). Low-Frequency Electrical Stimulation Increases Muscle Strength and Improves Blood Supply in Patients With Chronic Heart Failure. *Circulation Journal Vol 70* , pp. 75-82.

E. Hering, R. M. (2005). Taschenbuch derMathematik und Physik. In R. M. E. Hering, *Taschenbuch derMathematik und Physik* (p. 337). Springer-Verlag Berlin Heidelberg.

Ebner, F. (n.d.). *Piercingtrends.* Retrieved Oktober 5, 2017, from http://www.piercingtrends.de/piercing-material.html

EMAG eldec Induction GmbH. (2017). *EMAG eldec Induction GmbH*. Retrieved 10 23, 2017, from http://www.eldec.net/de/anwendungen/induktives-erwaermen.html

Engineering, T. T. (2017). *The Engineering ToolBox*. Retrieved 10 21, 2017, from https://www.engineeringtoolbox.com/permeability-d_1923.html

Eun Jung Park, S. J. (2014, July). Repetitive Transcranial Magnetic Stimulation to Treat Depression and Insomnia with Chronic Low Back Pain. *Korean J Pain 2014 July; Vol. 27, No. 3* , pp. 285-289.

Flora Margarida Barra Bisinottoa, R. A. (2017, September). Burns related to electrosurgery – Report of two cases. *Brazilian Journal of Anesthesiology (English Edition) Volume 67, Issue 5* , pp. 527-534.

Geddes, L. (1994). The first Stimulators - Reviewing the history of electrical stimulation and the devices crucial to its development. *IEEE Engineering in Medicine and Bilology* , 532.

Georg. (1999). Elektromagnetische Felder und Netzwerke. In Georg, *Elektromagnetische Felder und Netzwerke.* Heidelberg: Springer Verlag Berlin Heidelberg.

Gerthsen, C. (1964). Physik ein Lehrbuch zum Gebrauch neben Vorlesungen 8. Auflage. In C. Gerthsen, *Physik ein Lehrbuch zum Gebrauch neben Vorlesungen 8. Auflage* (p. 201). Berlin Heidelberg: Springer Verlag Berlin Heidelberg.

Giancoli, D. C. (2010). Physik Lehr- und Übungsbuch 3. Auflage. In D. C. Giancoli, *Physik Lehr- und Übungsbuch 3. Auflage.* München: Pearson Education Deutschland GmbH.

Girometti, R. (2015, 7 28). 3.0 Tesla magnetic resonance imaging: A new standard in liver imaging? *World Journal of Hepatology* , pp. 1894-1898.

H.D. Bradshaw, A. B. (2003, February 12). The acute effect of magnetic stimulation of the pelvic floor on involuntary detrusor activity during natural filling and overactive bladder symptoms. *Department of Urology, *Medical Physics and Clinical Engineering, and †Obstetrics and Gynaecology, Sheffield Teaching Hospitals, UK* , pp. 810-813.

Hansjörg Graf, G. S. (2007). Heating of Metallic Implants and Instruments Induced by Gradient Switching in a 1.5-Tesla Whole-Body Unit. *Journal of magnetic Resonance Imaging 26* , pp. 1328-1333.

Health, O. W. (n.d.). *World Health Organization*. Retrieved 12 2017, 18, from World Health Organization: http://www.who.int/ageing/en/

Heintze, J. (2016). *Lehrbuch zur Experimentalphysik Band 3.* Heidelberg: Springer Verlag GmbH.

Hiroyuki Muranaka, T. H. (2009). Evaluation of RF Heating on Hip Joint Implant in Phantom during MRI Examinations.

Igor But, M. F. (2005, May). FUNCTIONAL MAGNETIC STIMULATION FOR MIXED URINARY INCONTINENCE. *The Journal of Urology Volume 173, Issue 5* , pp. 1644-164.

(2005). *Infrarot-Thermometer IR-365RF Operating instructions.* Voltcraft®.

Jiles, D. C. (2007). *Introduction to the Principes of Materials Evaluation.* Boca Raton: CRC Press.

Kallenbach, E. Q. (2008). *Elektromagnete Grundlagen. Berechnung, Entwurf.* Wiesbaden: Springer Vieweg.

Karl Küpfmüller, W. M. (2013). *Theoretische Elektrotechnik- Eine Einführung.* Springer Vieweg.

Ke Yang, Y. R. (2010). Nickel-free austenitic stainless steels for medical applications. *Sci Technol Adc Mater* .

Kenneth B. Baker, J. A.-M. (2004). Evaluation of Specific Absorption Rate as a. *OURNAL OF MAGNETIC RESONANCE IMAGING 20* , pp. 315-320.

Kenneth W. Hinchcliff, A. J. (2014). Equine Sports Medicine & Surgery . In A. J. Kenneth W. Hinchcliff, *Equine Sports Medicine & Surgery* . Elsevier .

Kraft, K. (2010). Lehrbuch Naturheilverfahren. In K. Karin, *Lehrbuch Naturheilverfahren.* Stuttgart: Hippokates Verlag.

Kühn, R. (1963). *Funktechnik- Grundlage der Sende-, Empfangs- und Funkortungstechnik.* Braunschweig: Vieweg & Sohn.

Kurt Steinhoff, N. S. (2011). Bericht zur Metallformgebung - Band 2: Untersuchung der plastischen Formgebung unter Einfluss örlich und zeitlich veränderlicher Temperatur- und pannungszustände. Kassel: Kassel University Press GmbH.

Langguth B, L. M. (2014, May). Efficacy of different protocols of transcranial magnetic stimulation for the treatment of tinnitus: Pooled analysis of two randomized controlled studies. *World J Biol Psychiatry. 2014 May* , pp. 276-285.

M. Geetha, A. S. (2009). Ti based biomaterials, the ultimate choice for orthopaedic. *Progess in Materials Science 54* , 397-425.

Mark S. George, R. H. (2007). *Transcranial magnetic Stimulation in clinical Psyhiatry.* Washington DC: American Psychiatric Publishing .

Martellucci, J. (2015). *Electrical Stimulation for Pelvic Floor Disorders.* Switzerland: Springer International Publishing .

Masahito Kobayashi, A. P.-L. (2003). Transcranial magnetic stimulation in neurology. *The Lancet Neurology Vol 2* , p. 145.

MathWorks, I. U. (n.d.). *MathWorks Inc, USA*. Retrieved 1 15, 2018, from https://www.mathworks.com

MatWeb. (2017). *MatWeb Material property data*. Retrieved 10 21, 2017, from MatWeb Material property data: http://www.matweb.com/search/datasheet_print.aspx?matguid=b350a789eda946c6b86a3e4d3c577b39

Maurice Lippmann, W. A. (1974). *Burns of the Skin Caused by a Peripheral-nerve Stimulator.* Anesthesiology 1 1974 Vol.40, 82-84.

Medical Boston Center. (2017). *Pelvic Floor Stimulation for Treatment of Incontinence.* Boston: Boston Medical Center.

Monika Saini, Y. S. (2015). Implant biomaterials: A comprehensive review. *World J Clin Cases* , 52-57.

Mukerji, K. S. (2015). *Electromagnetics for Electrical Machines.* Boca Raton: CRC Press.

Nalbach, M. (2016). *Safety Monitoring for Functional Magnetic Stimulation.* Vienna: Technische Universität Wien .

Obermann, H. S. (2006). Basiswissen der Elektro-, Digital- und Informationstechnik. In H. S. Obermann, *Basiswissen der Elektro-, Digital- und Informationstechnik* (p. 3). Wiesbaden: Vieweg & Sohn Verlag.

P. Weinzierl, M. (1970). *Lehrbuch der Nuklearelektronik.* Wien: Springer Verlag.

Pennes, H. (1948). Analysis of tissue and arterial blood temperatures in the resting human forearm. Journal of Applied Physiology. In H. Pennes, *Analysis of tissue and arterial blood temperatures in the resting human forearm. Journal of Applied Physiology.*

Peter Kurzweil, B. F. (2008). *Physik Formelsammlung: Für Ingenieure und Naturwissenschaftler.* Wiesbaden: Friedr. Vieweg & Sohn Verlag.

Peter Nordbeck, F. F. (2008). Spatial Distribution of RF-Induced E-Fields and Implant. *Magnetic Resonance in Medicine 60* , pp. 312-319.

PonteMed. (2016). *Bedienungsanleitung.* St. Gallen: PonteMed GmbH medical systems.

PonteMed. (2016). *Instruktions-Handout.* St. Gallen: PonteMed GmbH medical systems.

PonteMed, A. (2016). *PonteMed AG*. Retrieved 10 18, 2017, from https://www.pelvipower.com

Processors, I. C. (2012, 11 12). *AZo Materials*. Retrieved 11 2017, 28, from https://www.azom.com/article.aspx?ArticleID=1723

Quick, H. (2011). *Ab wie viel Tesla wird es im MRT gefährlich?* Retrieved 01 06, 2018, from http://www.imp.uni-erlangen.de/mri/pdf/roentgenkongress.pdf

Rau, S. (2004). Die Metalle. In S. Rau, *Die Metalle* (p. 277). München: Neuer Merkur GmbH.

Reth. (1959). *Grundlagen der Elektrotechnik.* Wiesbaden: Springer Dachmedien Wiesbaden GmbH.

Ria Bhola, E. K. (2015, June 3). Single-pulse transcranial magnetic stimulation (sTMS) for the acute treatment of migraine: evaluation of outcome data for the UK post market pilot program. *The Journal of Headache and Pain* .

Robert L. Folmer, S. M. (2015, August). Repetitive Transcranial Magnetic Stimulation Treatment for Chronic TinnitusA Randomized Clinical Trial. *JAMA Otolaryngol Head Neck Surg Volume141, Number8* , pp. 716-722.

Rodney Boyer, G. W. (1994). Materials Properties Handbook: Titanium Alloys. In G. W. Rodney Boyer, *Materials Properties Handbook: Titanium Alloys* (p. 125). ASM International.

Sachin G. Ghalme, A. M. (2016). Biomaterials in Hip Joint Replacement. *International Journal of Materials Science and Engineering* , 113-125.

Schönekeß, H. C. (2009). *Bestimmung statischer und dynamischer Zugspannungen in STahlverseilungen mittels Wirbelstrom-Multisensoren und Ansätzen zu einer Sensordatenfusion.* Kassel: Kassel University Press GmbH.

Standard, V. (2008, 06 13). *Der Standard*. Retrieved 12 2017, 18, from Der Standard: http://derstandard.at/3135198/Aus-der-Huefte

Statista, G. (n.d.). *Statista- Das Statistik-Portal*. Retrieved 12 18, 2017, from Statista- Das Statistik-Portal: https://de.statista.com/statistik/daten/studie/182669/umfrage/hueftgelenksoperationen-in-ausgewaehlten-oecd-laendern/

Steffen Paul, R. P. (2014). Grundlagen der Elektrotechnik und Elektronik 1 5. Auflage. In R. P. Steffen Paul, *Grundlagen der Elektrotechnik und Elektronik 1 5. Auflage* (p. 74). Berlin Heidelberg: Springer Vieweg.

Tadeja Štrumbelj, P. P. (n.d.). Treatment of Urinary Incontinence with Functional Magnetic Stimulation (FMS).

TENS-EMS-Reizstrom. (n.d.). *TENS-EMS-Reizstrom*. Retrieved 12 11, 2017, from http://www.tens-ems-reizstrom.de/ems/anwendung-von-ems/

Timothy Wade Stippick, M. R. (2016). Combined magnetic fields provide robust coverage for interbody and posterolateral lumbar spinal fusion sites. *Med Biol Eng Comput 54* , pp. 113-122.

Tomonori Yamanishi, Y. H.-X. (2014). Multicenter, randomized, sham-controlled study on the efficacy of magnetic stimulation for women with urgency urinary incontinence. *International Journal of Urology (2014) 21* , pp. 395-400.

Vargas Luna, D. J. (2016). *Development of a monitor to detect metallic implants in the surroundings of the PelviPower MTF coil.* Vienna: Medical University of Vienna.

Vasilios K. Kimiskidis, D. K. (2013, February 1). Transcranial magnetic stimulation (TMS) modulates epileptiform discharges in patients with frontal lobe epilepsy: a preliminary EEG-TMS study. *International Journal of Neural Systems Volume 23* .

VOLTCRAFT Conrad Electronic AG, S. (n.d.). *VOLTCRAFT, Conrad Electronic AG*. Retrieved 1 15, 2018, from http://www.voltcraft.ch

Wakolbinger, B. (2013, 04 25). *Österreichische Ärztezeitung Nr. 8* . Retrieved 12 2017, 18, from Österreichische Ärztezeitung Nr. 8 : http://www.aerztezeitung.at/archiv/oeaez-2013/oeaez-8-25042013/hueftendoprothesenregister.html

Webcraft, G. (n.d.). *Webcraft GmbH- M-08 Flux- Detektor.* Retrieved 15 1, 2018, from https://www.supermagnete.at/physik-magnete/flux-detektor-gross-folie-zum-anzeigen-von-magnetfeldern-ca.-150-x-150mm_M-08

Weißgerber, W. (2013). *Elektrotechnik für Ingenieure - Formelsammlung.* Wiesbaden: Springer Vieweg.

Welsch, S. L. (2013). Materie Erde, Wasser Luft und Feuer. In S. L. Welsch, *Materie Erde, Wasser Luft und Feuer* (p. 202). Berlin Heidelberg: Springer Verlag Berlin Heidelberg.

Wilfried Plaßmann, D. S. (2009). Handbuch Elektrotechnik- Grundlagen und Anwendungen für Elektrotechniker 5. Auflage. In D. S. Wilfried Plaßmann, *Handbuch Elektrotechnik- Grundlagen und Anwendungen für Elektrotechniker 5. Auflage* (p. 255). Wiesbaden: Vieweg+Teubner.

Wolf, P. (2008). Thermal considerations for the design of an implanted cortical brain– machine interface (bmi). In Indwelling Neural Implants: Strategies for Contending with the In Vivo Environment. In P. Wolf, *Thermal considerations for the design of an implanted cortical brain–machine interface (bmi). In Indwelling Neural Implants: Strategies for Contending with the In Vivo Environment* (p. Chapter 3). CRC Press/Taylor & Francis.

Wood R, B. K. (2012, June). 1.5 Tesla Magnetic Resonance Imaging Scanners Compared with 3.0 Tesla Magnetic Resonance Imaging Scanners: Systematic Review of Clinical Effectiveness. *CADTH Technology Overviews Volume 2, Issue 2* .

Yamazaki M, e. a. (2016). Evaluation of Artificial Hip Joint with Radiofrequency Heating Issues during MRI Examination: A Comparison between 1.5 T and 3 T.

Yesim Bakar, Ö. C. (2011, November). The use of extracorporeal magnetic innervation for the treatment of stress urinary incontinence in older women: a pilot study. *Archives of Gynecology and Obstetrics Volume 284, Issue 5* , pp. 1163-1168.

Yigitcan Eryaman, B. A. (2011). Reduction of Implant RF Heating Through Modification. *Magnetic Resonance in Medicine 65* , pp. 1305-1313.

APPENDIX

A: ADDITIONAL MEASUREMENTS

To study the effect of the material on the detection range, the following experiment was performed, with a small cobalt-chromium-molybdenum sphere shaped hip head (Figure 49), designed from the company BBRAUN Austria with the part number NK544K for the BiCONTACT® Hip Endoprosthesis System. It consists of 90,7% chromium, 5,8% molybdenum and 3,5% cobalt. This sample is a unipolar hip head with a diameter of 28mm, a volume of 8,157cm^3 and a surface area of 31,48cm^2. Because there is no accurate recording of the magnetic permeability and electrical resistance of CoCr29Mo, similar values were assumed as from the material CoCr Alloy.

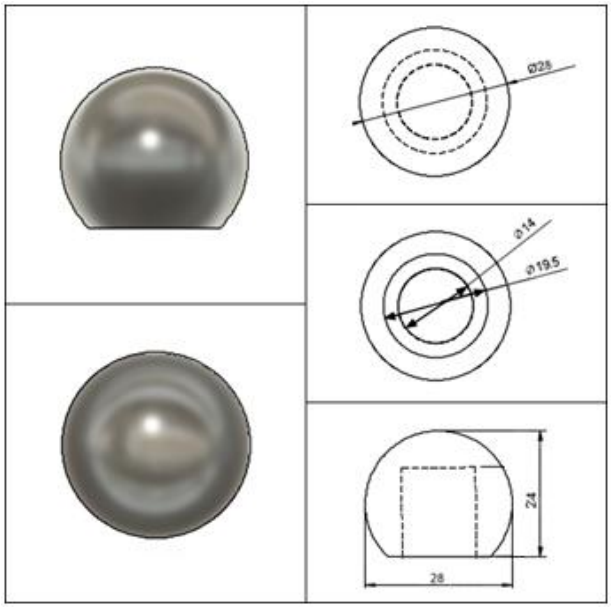

Figure 49: Overview and dimensions of the small CoCr29Mo sample

With this sample, six repetitions were performed in the Center position and with a distance of 40mm. The settings and execution of the measurements were the same as for the other samples.

As can be seen in Figure 50, the power density varies between 70,68mW/cm^2 and 82,91mW/cm^2. This corresponds to a mean of 75,71mW/cm^2.

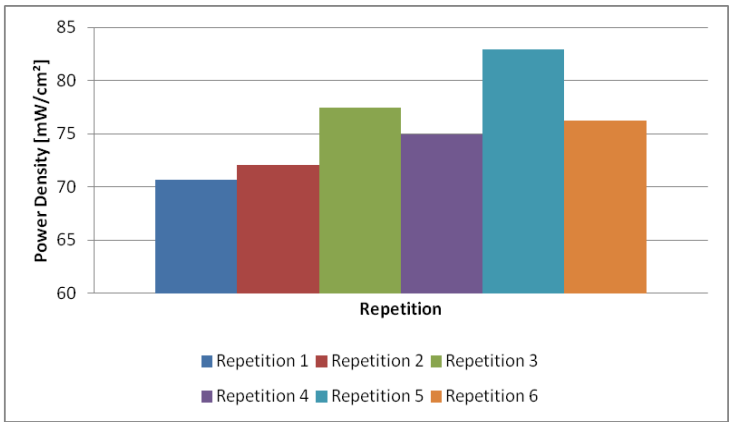

Figure 50: 2-dimensional histogram of the power density plotted over the different repetitions for the small CoCr29Mo sample (Vargas Luna, 2016)

Figure 51 shows a typical heating up curve for this sample in the Center at a distance of 40mm between seat surface and sample. The temperature is plotted on the x-axis and the time on the y-axis. Figure 51a) shows the original temperature curve of the iron sample. Figure 51b) shows the heating curve after the low-pass Butterworth filter, order 2. The red line represents the temperature profile after the low-pass Butterworth filter and the green line represents the maximum slope. The maximum slope sustained over 40 seconds was determined to calculate the power and power density.

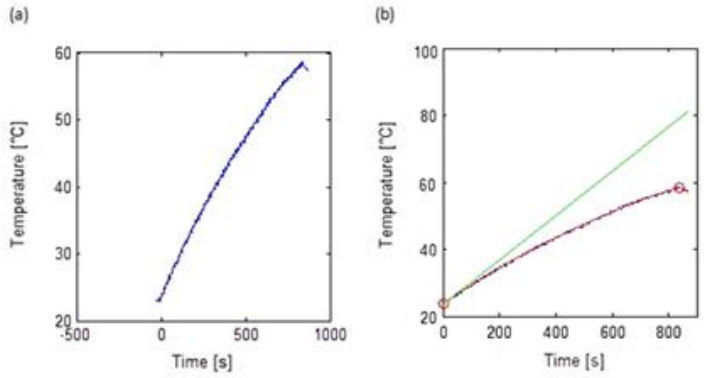

Figure 51: Plot example of the small CoCr29Mo sample: (a) original data of the temperature measurement, starting at time zero. After the end of the measurement, the temperature drop can be seen (b) slightly magnified section of the maximum slope (green line) and the filtered temperature sequence (red line) with the starting point

A comparison of the power densities of both samples, resulting in similar values, can be seen in Table 11. The large sample has a maximum recorded power density of 92,61mW/cm^2 and a mean value of 81,31mW/cm^2. Due to the size of the small sample and the same material, the slightly higher power densities can be explained. As already mentioned, the resulting power density and the maximum detectable range are related. The higher the power density, the larger the secondary magnetic field and the detection rate increases. From these results, it can be seen, that the small sample can also be reliably detected.

Table 11: Comparing the small and the large CoCr29Mo sample

Small CoCr20Mo	Power density [mW/cm²]	Large CoCr20Mo	Power density [mW/cm²]
Repetition 1	70,68	**Repetition 1**	92,61
Repetition 2	72,04	**Repetition 2**	70,02
Repetition 3	77,42		
Repetition 4	74,92		
Repetition 5	82,91		
Repetition 6	76,24		

In addition to implants, other metal objects, such as a copper spiral for women or a piercing, during treatment were tested.

Woman intrauterine device can be influenced by the magnetic field as well (see Figure 52a). Because of the size and shape of the spirals, the spiral hardly heats up and is therefore no danger for the surrounding tissue. Due to the lightweight, these samples were examined for vibration movements. The aim of these measurements was to determine the possible vibration movement of the intrauterine device, due to the magnetic field, and therefore an unwanted risk for woman. The tests show that the device does not move above the seat of the PelviPower Magnetic Field Trainer during treatment. More detailed investigations should still be made to guarantee this with high accuracy.

In addition to the intrauterine device also a piercing was tested (see Figure 52b). The test shows similar results as with the copper spiral. No significant heating of the material and no vibration movements were detected. Finally, a ring was tested to examine "bigger" pieces of jewelry (see Figure 52c). But even with this sample, no heating and vibration movements were measured.

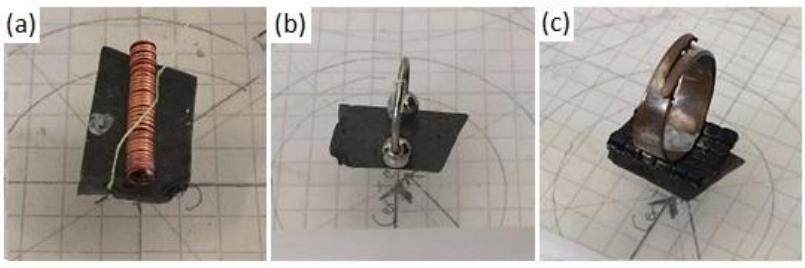

Figure 52: Additional tested materials: (a) intrauterine device (b) piercing (c) ring

B: AVAILABLE COMMANDS FOR THE DEVICE

Table 12 contains the available commands that the device is programmed to understand and answer:

Table 12: Table of command and response codes available for the device (Vargas Luna, 2016)

Command	Hex Code	Description
metalDetection	0x00	Request perform a metal detection
noMetalDetected	0x00	Indicated that no metal was detected
metalDetected	0x01	Indicate that a metal is detected
calMissing	0x02	ERROR: Indicate that the calibration is missing
overHeat	0x03	Indicate that the system is above the maximum operating temperature or that the ventilation system was unable to restrain the warming of the heatsink.
satError	0x04	Indicate that the voltages measured are near the saturation value. This express two scenarios: the coil is disconnected or the values are so high that the measurement are unreliable.
selfTest	0x01	Request a self-test
selfTestPassed	0x00	Indicate that the self-test was passed successfully
selfTestFailed	0x01	Indicate that the self-test was unsuccessful
calibration	0x02	Request the device to measure a calibration value
calCompleted	0x00	Indicates that the calibration was successful
calError	0x01	Indicates that the calibration was unsuccessful
calWritingError	0x02	ERROR: Reference values weren't save correctly in the memory
overHeat	0x03	Same that in metalDetection
satError	0x04	Same that in metalDetection
service	0x03	Requests the device a specific value
ser_softwareV	0x00	Requests the current software version of the monitor
softwareVersion	0x00001	Pre-release version

ser_res_freq	0x01	Requests the resonance frequency being used by the system
ser_raw_voltage	0x02	Request the last raw voltage level measured
ser_raw_th	0x04	Request the threshold of the 1st raw voltage level at position 0%
ser_app_state	0x06	Request the status of the state machine
watchdog	0x04	Request an ack to verify the status of the UART port
initDone	0x05	Indicates that the system was initialized
initSuccessful	0x01	Indicates that the system initialization was successful
initFail	0x02	Indicates that the system initialization was unsuccessful
emergencyStop	0x06	Request the system to restart regardless the current state
State Request	0x08	Request the current state of the state machine

In order to facilitate the correct communication, short acknowlEdge messages are also implemented, as can be seen in Table 13:

Table 13: Table of acknowledgment codes available for the device (Vargas Luna, 2016)

Command	**Hex Code**	**Description**
ack	0x30	Message received correctly
checkError	0x01	The check sum does not correspond to the received bytes
frameLost	0x02	The Frame number does not match with internal count
notAvailable	0x03	The system is busy and cannot receive/process further requests
frameIncomplete	0x04	The number of bytes is different to the pre-established lengths.
UnexpectedFrame	0x06	Indicate that an ack/nack was received when it was not expected
invalidCommand	0x07	Invalid command received
bufferOverRun	0x08	The UART buffer was over run and some data might be lost

C: Circuit's Schematics